7-27-2024

Modeling Fire Behavior: Increasing Fidelity in High-Complexity Fire Models

Jenna Sjunneson McDanold
jsm7044@rit.edu

Recommended Citation

McDanold, Jenna Sjunneson, "Modeling Fire Behavior: Increasing Fidelity in High-Complexity Fire Models" (2024). Thesis. Rochester Institute of Technology. Accessed from

RIT

Modeling Fire Behavior:

Increasing Fidelity in High-Complexity Fire Models

by

Jenna Sjunneson McDanold

A Dissertation submitted in Partial Fulfillment of the Requirements
for the Degree of Doctor of Philosophy in Mathematical Modeling

School of Mathematics and Statistics
College of Science

Rochester Institute of Technology
Rochester, NY
July 27, 2024

Committee Approval:

Dr. Anthony Vodacek Date
Chair, Dissertation Committee
Professor, Chester F. Carlson Center for Imaging Science, College of Science
Rochester Institute of Technology, Rochester, NY

Dr. Nishant Malik Date
Advisor
Assistant Professor, School of Mathematics and Statistics, College of Science
Rochester Institute of Technology, Rochester, NY

Dr. Niels Otani Date
Committee Member
Associate Professor, School of Mathematics and Statistics, College of Science
Rochester Institute of Technology, Rochester, NY

Dr. Tony Wong Date
Committee Member
Assistant Professor, School of Mathematics and Statistics, College of Science
Rochester Institute of Technology, Rochester, NY

Dr. Alex Jonko Date
Committee Member
Staff Scientist, Los Alamos National Laboratory
Earth and Environmental Sciences Division
Climate, Ecology, and Environment Group

Dr. Rod Linn Date
Committee Member
Senior Staff Scientist, Los Alamos National Laboratory
Earth and Environmental Sciences Division
Energy and Natural Resources Security Group

Dr. Nathan Cahill Date
Director, Mathematical Modeling Program
Professor, School of Mathematics and Statistics, College of Science
Rochester Institute of Technology, Rochester, NY

TABLE OF CONTENTS

LIST OF FIGURES

LIST OF TABLES

Acknowledgements

Thank you to my RIT advisor, Nishant Malik, for his support and instruction throughout these past six years. I am also grateful to Rod Linn and Alex Jonko, my mentors at the Los Alamos National Laboratory (LANL) who have helped me expand my knowledge of fire behavior, atmospheric sciences, and generally how to be a scientist. My gratitude extends to Kara Yedinak who helped me with many long discussions of fire behavior and atmospheric interactions and also helped me understand another perspective on scientific work outside of the lab. I would like to thank Bob Kremens who helped me get started on this journey by teaching me the basics of thermodynamics and helping me connect to LANL. And finally, to the extensive list of co-authors on my papers for helping me be an ecologist, a fire behavior expert, and a fluid physicist as well as a mathematician.

I could not have accomplished this without the unending support from my parents and their respective partners who due to the time difference between here and Australia helped me mentally handle the stress of being a student with many a late night phone call.

Finally, I’m grateful to the bunnies that I have had during this degree; Bonnie and Clyde who have passed, and now Ginny and Major Adams, who all put up with my emotions and frustrations and continued to provide love and a constant source of amusement.

The research presented in this thesis was made possible by funding from the School of Mathematics and Statistics, Rochester Institute of Technology, and various divisions and centers of the Los Alamos National Laboratory (LANL), including the Earth and Environmental Sciences Division (EES), the Center for Space and Earth Sciences (CSES), and the Center for Non-Linear Sciences (CNLS).

Abstract

Recent technological advances have yielded several high-complexity models for fire behavior. Low-intensity burns present difficulties in modeling due to a strong sensitivity to wind and fuels. This dissertation explores support research to improve representation of low-intensity fire in these high-complexity fire simulations. We focus on three areas: (i) data-driven modeling with a Spatially Extended Radiant heat Fire model (SERF), (ii) fuel heterogeneity with our model Distribution of Understory using Elliptical Transport (DUET), and (iii) research on whole system dynamics using chaos theory. To increase simulated resolution of low-intensity fire behavior, we employ an observational data set to develop SERF with spatial resolution on the order of ≈ 0.05 m^2, in contrast to the 1–2 m^2 typical of the process-based models. SERF uses probability distributions to calculate radiant heat levels through a coupled map lattice which then inform a cellular automata model. In response to the need for more detailed surface vegetation maps, we develop a mechanistic model for estimating variation in surface vegetation called the Distribution of Understory using Elliptical Transport (DUET). DUET connects the canopy structure to the litter dispersal using ellipses based on tree species characteristics, wind data, and location-specific features, and then calculates grass growth and decomposition in the years since the last burn of the area. Finally, we investigate the sensitivity of a high complexity wildfire model, FIRETEC, using chaos theory. We develop 3900 one-dimensional time series from a FIRETEC simulation designed to represent low-intensity burning conditions. We test them using the Chaos 0-1 Test and an artificial neural network designed to distinguish between stochastic and deterministic series. By focusing on data-driven modeling, vegetation mapping, and broad-scale dynamics, our work adds essential support models and research to process-based fire models when representing low-intensity burns.

CHAPTER 1. Introduction

1.1 Background

Oxygen, heat, and fuel are the three components that influence fire dynamics (Quintiere 1998). However, the simplicity of this “fire triangle” can be misleading, as different configurations of these ingredients lead to a diverse set of dynamics. The topography of the fuel bed influences the convection and radiative heat transfer (Iniguez, Swetnam, and Yool 2008; Clements and Seto 2015; Airey-Lauvaux et al. 2022). Differences in litter accumulation or treatments in a given area can change the surface and ladder fuels and lead a lower-intensity fire to develop into a high-intensity crown fire (Kilgore and Sando 1975; Menning and Stephens 2007; Alvarez, Gracia, and Retana 2012). Flow fields in the atmosphere interact with the heat released from a fire to create new atmospheric flows and can lead to unique phenomena like fire whirls and counter-rotating vortices in and around the flames (Potter 2012a, 2012b; Lareau et al. 2022). These are just a few examples of the possible complex behaviors that can develop from these three simple components.

Fire is an essential element to healthy ecosystems across the world. Many environments are considered to be “fire-dependent” ecosystems, in that the flora and fauna present in the area require heat for survival (Sauer 1950; Bond, Woodward, and Midgley 2005; McGranahan and Wonkka 2020; McLauchlan et al. 2020; Robbins et al. 2022). Many plants use heat to motivate their reproductive processes, or the area may require clearing of debris or dead surface layers, leaving a carbon rich soil for new growth. Crown fires may clear some of the canopy to leave room for sunlight to reach the surface and provide warmth to seedlings or smaller plants that require sun to grow. Ecosystems rely on the balance of nutrients and natural resources and fire is one of many contributing factors for healthy systems.

Some human suppression tactics have had devastating effects on these fire-dependent ecosystems (Van Lear et al. 2005; Keane et al. 2008; La Puma, Lathrop, and Keuler 2013; Hanberry 2021). To restore these ecosystems to their natural state, we often intentionally light fires in specified areas with particular ecological goals in mind. This practice is called "prescribed burning." These burns are designed for the given ecosystem considering several factors including wind and environmental conditions as well as ecological needs (Wade and Lunsford 1989; Keane et al. 2008; Linn et al. 2021). In the performance of prescribed burns, control is of utmost importance to avoid unintentionally damaging the environment or the surrounding structures (Wade and Lunsford 1989). Typically, prescribed burns are designed to be lower intensity than major wildland fires to avoid escape and unintentional ecological damage (Wade and Lunsford 1989; Van Lear et al. 2005; Linn et al. 2021). These lower intensity fires, defined here as slow-moving surface-level fires, tend to be more sensitive to environmental conditions including slight wind variations and surface fuel spatial heterogeneity (Clements et al. 2015; Jonko et al. 2021; Linn et al. 2021). Due to their low flame lengths and slower speeds, they can also be easier to control. Fire practitioners and land managers are always seeking a better understanding of fire behavior to avoid damaging the ecosystems further and design our prescriptions to minimize the risk of escape.

To further our understanding of fire dynamics, we require a substantial variety of data sets to allow for the examination of the whole system and its components. Collecting data in the field is challenging given the large amount of energy emitted from even the smallest fires, the consumption of vegetation (fuel), and the complex interactions in the fire environment. However, it is possible to design new experiments for specific measurement goals through computer modeling and simulation. In particular, numerical models offer us the ability to generate data at the spatial resolution characteristic of low-intensity fire propagation without the risks and challenges associated with data collection in the field. Even though models may lack some of the physical processes, the intricacy and fidelity of these models in comparison to experimental data make them an essential tool for studying fire dynamics.

Hawley (1926) and Gisborne (1927) began the conversation regarding the value of forest fire modeling and objectives for the research in the 1920s. Their initial models relating fire spread to weather patterns and moisture contents laid the groundwork for more complex models in the 30s and 40s. Curry and Fons (1938) employed observational data from the field connecting wind, moisture, time, and slope to approximate rate of perimeter increase for Ponderosa Pine forests in California, but found that the results were unique to the circumstances of the data and could not be universally applied. Fons (1946) then expanded the model to include results from laboratory experiments with homogeneous fuel beds in an attempt to develop knowledge of the fundamental processes contributing to fire spread.

Following World War II, fire modeling expanded significantly after the government reports by Chandler, Storey, and Tangren (1963) and Rogers and Miller (1963) regarding the resulting mass fires from nuclear explosions (Sullivan 2009). These reports led to an increased desire for understanding fire behavior and developing "fire-danger" metrics. Weber (1991) provided a comprehensive review of the various models developed from this era, dividing them into three categories: statistical, empirical, and physical. The statistical models rely on data collected in the field and generally work well for fires that are similar to the data upon which they are based, but have minimal success for fires outside of those specific parameters (Weber 1991; Linn 1997; Sullivan 2009). McArthur (1966) developed a statistical model using grassland fire data which was used to develop a fire-danger metric, classifying likelihood of fire danger from “low-moderate” to “catastophic.” This model was translated into equations by Noble, Gill, and Bary (1980) and is still being used extensively, particularly in Australia (Griffiths 1999; Khastagir, Jayasuriya, and Bhuyian 2018; Shah et al. 2022).

Arguably, one of the most well-known models in the fire science community from this era is the Rothermel (1972) model. Based on a model built by Frandsen (1971) in conjunction with McArthur (1966) data plus wind tunnel experimental data developed by Rothermel and Anderson (1966) and modified by Albini (1976), the Rothermel model uses these data and applies equations that represent the heat flux and energy transfer within a fire in one-dimension (Weber 1991; Andrews 2018). It is classified as a quasi-empirical model by Sullivan (2009), as it uses data as well as equations, but does not represent the specific type of heat transfer. Often this model has been implemented as a base for more complex models as in BEHAVE (Burgan 1984), FARSITE (Finney 1998), and *FireStation* (Lopes, Cruz, and Viegas 2002). Cellular automata models that track fire through a landscape also use Rothermel’s model as in Yongzhong et al. (2004), Trunfio et al. (2011), and Zhang et al. (2022).

The physical models from Weber (1991) are those that attempt to represent the physical and/or chemical processes from combustion, and are the types of models we refer to as “high-complexity.” The Fons (1946) model would be the first of this type of model, but recently, major technological advances have increased computational power to allow for more complex coupled atmosphere-fire models. These models often use computational fluid dynamics (CFD) to resolve the wind behavior interacting with the heat from the fire. For instance, the National Center for Atmospheric Research developed WRF-SFIRE that uses the Weather Research and Forecasting model (WRF) in conjunction with the fire spread model SFIRE (Mandel et al. 2014). SFIRE was developed from the Coupled Atmosphere-Wildland Fire Environment (CAWFE) which uses the Rothermel fire-spread model applied to three dimensions (Clark et al. 1996). The Wildland-urban-interface (WUI) Fire Dynamics Simulator (WFDS) was developed by the National Institute for Standards and Technology and is an extension of the urban fire simulator FDS (Fire Dynamics Simulator) (Mell et al. 2007). This model was specifically designed to investigate the effect of fires on the WUI, the intersection between wildland and urban environments. Finally, HIGRAD-FIRETEC, developed at the Los Alamos National Laboratory and used in the third part of this dissertation, uses the atmospheric model HIGRAD in conjunction with the fire behavior simulator FIRETEC (Linn et al. 2002). HIGRAD is specifically designed for atmospheric behavior under high gradients of temperature and pressure, such as those encountered during an active fire. HIGRAD is coupled with FIRETEC, a CFD fire behavior model designed to be a research tool for the fundamental physical processes occurring during wildfires.

Due to the acute sensitivity for low-intensity fires, representing wind variation and surface fuel heterogeneity becomes vital to the success of these high-complexity models in simulating this type of fire (Linn et al. 2021). Additionally, comparison to data and evaluating uncertainty in these input parameters may lead to more precise estimates of low-intensity burning behavior. Our research involves modeling efforts in support of these process-based fire behavior models to increase fidelity for low-intensity fires. For this dissertation, we split this research into three sections: (i) a spatially extended model from data collected in the field to study low-intensity behavior dynamics at small-scales, (ii) a mechanistic surface fuel model based on canopy structure to represent greater surface fuel heterogeneity for input parameters, and (iii) an investigation into the chaotic qualities of low-intensity fires using nonlinear time series analysis. These three components are described in detail below and throughout this thesis.

1.2 SERF

Our first goal involves studying a dataset collected in the field of small-scale, low-intensity fires lit in the New Jersey Pine Barrens over the course of several years. We develop a Cellular Automata (CA) model to mimic these data fires, as CA models miminize the computational expense of modeling by discretizing time and space, reducing the model to a collection of basic equations applied to each cell during a single timestep. Physicists often utilize the CA framework for representing geophysical processes that adhere to some basic physical laws in which the new value for a particular spatial location at time *t* depends on the spatial neighborhood at previous timesteps (Wolfram 1983; Toffoli 1984; Vichniac 1984). From snow avalanche models to lava flows to porous media, CA models are popular among fluid flow modelers (Rothman 1988; Kronholm and Birkeland 2005; Herault et al. 2009).

The discretization process resembles using Reimann sums to calculate integral approximations. While some information may be lost in the estimation, the results can be close enough to be valuable depending on how and for what purpose you use the integral or model. CA models also often allow for the possibility of "self-reproduction" in that a neighboring state will directly reproduce itself in adjacent cells (Wolfram 1983), a common attribute of chaotic systems and fractals. Mathematical models are inherently approximations of the processes they represent, in which error estimates are used for validation purposes (Braga-Neto 2005; Rebba, Mahadevan, and Huang 2006).

Most wildland fire behavior CA-based models produce results that track the fireline and create images with limited information. These models use inputs regarding the surrounding topography and wind data, seeking to predict the area burnt over time. The typical resulting graphs focus on either contours of the fireline in time increments as in (Berjak and Hearne 2002; Alexandridis et al. 2008; Almeida and Macau 2011; Ghisu et al. 2015; Gennaro et al. 2017; Zheng et al. 2017), or they represent the shape of the resulting burnt area as in (Hernández Encinas et al. 2007; Yassemi, Dragićević, and Schmidt 2008; Trunfio et al. 2011; Mahmoud and Chulahwat 2017; Freire and DaCamara 2019), or both (Liu et al. 2018). These models take advantage of the finite set of discrete outputs in the CA framework, but this limits the information that can be obtained from the model.

Adding an underlying Coupled Map Lattice (CML) model to the CA framework allows for more information to be collected than with typical CA models that only produce a finite amount of discrete output values. In this project, we present a Spatially-Extended Radiant heat Fire model (SERF), a CA model using arrays with infrared radiant heat values recorded during a selection of small-scale prescribed fires. Using these infrared data, we determine the main characteristics of the radiant heat emanating from these fires and create a CML for simulating the fire behavior. We then use this CML to define five states of fire behavior for a CA model, creating a spatially extended discrete dynamical systems-based model whose parameters we determine from empirical data. The SERF model will be explained in detail in chapter 2.

1.3 DUET

The spread and intensity of wildland fire is determined by an interplay between elements of the fire environment, including fuels, weather, and topography (Rothermel 1972; Agee 1996). Fire behavior sensitivity to fuel heterogeneity depends on burn intensity and features of the fire environment. In low wind and low intensity fire scenarios, fire behavior can be particularly sensitive to the distribution of understory or surface fuels, consisting of live herbaceous vegetation, shrubs, and dead leaf litter, as the surface is the fire's primary fuel source (Stephens, Finney, and Schantz

2004; Hiers et al. 2009; Dell et al. 2017; Loudermilk, Hiers, and O'Brien 2017; Prior, Murphy, and Bowman 2018). Accounting for the spatial distribution and heterogeneity of surface fuels is thus important for predicting prescribed fire behavior, fire spread, as well as flanking and backing portions of wildfires (Campbell-Lochrie et al. 2021; Linn et al. 2021; Atchley et al. 2021). Recent work has highlighted fire behavior sensitivity to surface fuel distribution for a variety of ecosystems through observation and modeling which implies that the heterogeneity of these fuels is of particular interest (E. L. Loudermilk et al. 2011; E. Louise Loudermilk et al. 2014; O'Brien et al. 2016; Parsons et al. 2017; Hoffman et al. 2018; Skowronski, Gallagher, and Warner 2020; Coen et al. 2020; Linn et al. 2021).

In addition to wildland fire behavior, tree litter deposition patterns affect ecosystem dynamics by supplying soil nutrients through leaf, bark, and catkin litter decomposition (Midgley, Brzostek, and Phillips 2015). Several studies have examined how different tree species' litter affects soil nitrogen and carbon (Prescott and Grayston 2013; Lin et al. 2017; Trap et al. 2017). More precise representation of spatial litter distributions may lead to a better understanding of ecosystem changes due to litter accumulation from various tree species within forests or wetlands, and potentially how patterns of decomposition influence fire effects (Stephens, Finney, and Schantz 2004; Stoler and Relyea 2011; Arthur et al. 2012; Carpenter et al. 2021).

Heterogeneous tree litter and grass patterns are influenced by various factors, including overstory structure and prevailing winds, which affect when the foliage falls from trees or shrubs, where it lands, and how it influences grass distribution and density through indirect effects on resources (Riegel, Miller, and Krueger 1992; Staelens et al. 2003; Jonard, Andre, and Ponette 2006; Pecot et al. 2007). Once on the ground, other processes redistribute and decompose the litter material (Forrester and Bauhus 2016; García-Palacios et al. 2016). A number of factors can alter the trajectory of leaves when they fall from the tree, including the shape of the needles or leaves, the height from which they fall, and local winds (Nickmans et al. 2019). Decay variability, which depends on climatic conditions, species litter characteristics and chemistry, moisture retention, packing density etc., can change the depth and loading of the localized litter accumulation, the nutrient composition of the soils, and the moisture levels present at any given time (R. Mitchell et al. 1999; Adair et al. 2008; Keane 2008; Arthur et al. 2012; Cornelissen et al. 2017; Babl-Plauche et al. 2022; Berg and Lönn 2022).

Traditional sampling methods for obtaining accurate and spatially-explicit estimates of the dynamic heterogeneity of surface biomass require considerable investment in personnel, time, and money (Keane and Reeves 2012; Tinkham et al. 2012). At stand scales, scientists and managers commonly combine surface biomass sampling approaches with other forest and rangeland inventory methods to estimate the fuel load at landscape or prescribed fire burn block scales for various fuel strata (i.e., surface and canopy fuel layers). Terrestrial lidar has been used to characterize more localized (radius of tens of meters) fuel load in strata (E. Louise Loudermilk et al. 2009; Bright et al. 2017; Jarron et al. 2020). Lidar techniques and photogrammetric methods show success when representing surface fuels (Keane and Reeves 2012; Rowell et al. 2020). However, they are associated with great financial and labor costs when employed at landscape scales (Silva et al. 2016). Aerial lidar can be used at much larger spatial scales, and while it can be used to some degree to map coarse woody debris or shrubs, it is limited in its ability to detect lower strata surface fuels such as litter or grass, due to both signal noise and occlusion (Seielstad and Queen 2003; Gajardo, García, and Riaño 2014). Consequently, most studies using aerial lidar have focused on characterizing the canopy fuel layer and individual tree properties such as tree crown diameter, stem spatial-density, basal area, and biomass in several locations (Goodwin, Coops, and Culvenor 2006;

Hyde et al. 2006; Hudak et al. 2008; Ruiz et al. 2014; Silva et al. 2016). Litter and grass continue to be difficult to map with remote sensing, so spatially explicit data capturing their patterns at large extents is difficult to find.

Most previous work modeling litter dispersal employs probabilistic approaches. Ferrari and Sugita (1996) created an exponential model based on stem location, which Staelens et al. (2003) expanded to include wind influence. Jonard, Andre, and Ponette (2006) used a ballistic and a Weibull distribution approach that incorporated height of maximum crown radius, which was also used by Nickmans et al. (2019) to determine soil nutrient characteristics. Linn et al. (2005) used the vertically integrated canopy foliar mass above a location to infer litter and grass patterns, but this approach led to litter being only located directly under trees. The Jonard, Andre, and Ponette (2006) model assumed all leaves were released from the center of the tree at the height of maximum crown radius and it modeled leaf dispersal patterns using a seed dispersal model designed by Greene and Johnson (1989). Although there is value in each of these approaches, they miss some of the processes that impact litter dispersal, such as variation in heights and locations of trees from which leaves and needles fall, species-specific leaf and needle characteristics, and dominant seasonal wind events, which can create direction bias in litterfall heterogeneity.

We present here a mechanistic model we call Distribution of Understory using Elliptical Transport (DUET) that connects the litterfall from the trees to a specific canopy arrangement. It also uses dynamic decay rates that change with time and spatial configuration. The model develops a full picture of the surface fuels of a given area for use within FIRETEC, or with other fire modeling systems. The DUET model is described in detail in chapter 3.

1.4 Detecting Chaos in Fire

The concept of chaos was first introduced in the late 1800's by the mathematician Jules Henri Poincaré, and further defined in 1963 by meteorologist Edward Lorenz, who introduced the concept of the strange attractor (Lorenz 1963). There is some debate on the official definition of chaos, but it is generally accepted to include at least three features: sensitive dependence on initial conditions, and deterministic and aperiodic long-term behavior (Lorenz 1963; Banks et al. 1992; Brown and Chua 1996; Hunt and Ott 2015; Strogatz 2019). Sensitive dependence on initial conditions implies that a very slight change in an initial condition can result in vastly different outcomes. Deterministic behavior implies that any noisiness within the outputs are a result of the nonlinearity of the system, not any stochastic components. Specifically, a unique input to a deterministic system will always result in a corresponding unique output, whereas a stochastic system may produce a variety of outputs for any given input. Aperiodic long-term behavior is characterized by trajectories that do not "settle" into any kind of periodic behavior (i.e. limit cycles, stable fixed points, or quasiperiodic orbits). This is a secondary result of the combination of determinism and sensitive dependence on initial conditions; since no trajectory ends up exactly where any previous trajectory has been (unique inputs lead to unique outputs), no matter how close those trajectories are, there will be long-term divergence between them (sensitivity to initial conditions).

Gaining information on whole system dynamics using chaos theory could reveal new relationships between parameters and potentially improve our understanding of the interplay between all the characteristics of the fire. Clements et al. (2015) demonstrates that low intensity fires are sensitive to shifts in near-surface wind dynamics through field collected data during nine burns on different plots. Linn et al. (2021) uses one of those experimental burns to inform a FIRETEC simulation to further illustrate that small changes in the windfield can have a broad effect on fire behavior. Jonko et al. (2021) uses an ensemble approach in which they compare 45 FIRETEC simulations with identical conditions except for small perturbations in the ambient wind field. All of these studies clearly indicate that macroscopic fire behavior is sensitive to small perturbations in wind conditions. This sensitivity to small perturbations in initial conditions is a hallmark feature of chaos and nonlinear dynamics.

The attempt at prediction of chaotic systems beyond a particular time factor will result in significant uncertainty which creates challenges in effectively predicting geophysical systems, such as the weather, river flow, or sediment transport (Sivakumar 2004). By mathematically defining fire behavior as chaotic, we seek to discover relationships between its system components and some underlying patterns that contribute to the apparent irregularity of the system. Finding patterns in fire behavior will be a critical step in finding ways to evaluate uncertainty in these fire behavior models and improve prescribed fire designs for more control, thereby improving their effectiveness for reducing destructive wildfire events and restoring balance within fire-dependent ecosystems. We describe the study and the results in detail in chapter 4.

CHAPTER 2. SERF: Spatially Extended Radiant heat Fire model

The material presented below is part of the article published in *Physical Review E* (McDanold and Malik 2023).

2.1 Description of SERF

SERF defines $T_n(i,j)$, the radiant heat temperature at time step n for cell location (i,j), in five discrete stages. Using the CML framework, an equation defines the behavior of the radiant temperature for each stage, with parameter thresholds marking the transition from one stage to the next. These five stages represent the life cycle of radiant temperature for an area that burns. Figure 2.1 shows a schematic of the five stages and each are explained in detail within the following sections.

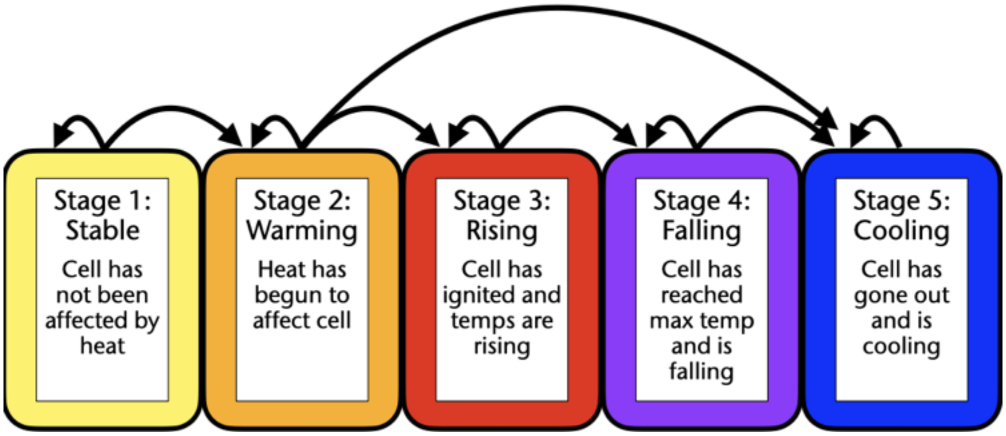

Figure 2.1: *A schematic of the five stages that make up the life cycle of a burning cell.*

2.1.1 The Model

All cells begin in stage one, *stable*, in which the heat from the oncoming fire has not yet reached this cell. Once that heat affects the cell, it transitions into the *warming* stage, and when the heat rises sufficiently for ignition, it transitions into stage three, *rising*. The heat then rises as the fuel is consumed until it reaches its maximum temperature,$T_M(i,j)$, after which it transitions into stage four, *falling*, when the radiant heat reduces as the fuel consumption completes. Once the fuel is gone, the flame ceases, and the cell transitions into stage five, *cooling*, in which the ground beneath the fire cools back to equilibrium with the ambient temperature of the area.

The parameters in SERF unique to each simulation are the domain size in two dimensions and the overall moisture content for the area, m_c. The parameters unique to each cell per simulation are the maximum radiant temperature $T_M(i,j)$, the heat transfer coefficient for the fuel $k(i,j)$, and the time required to rise to and fall from $T_M(i,j)$, $R(i,j)$ and $F(i,j)$ respectively. Each of these parameters are generated from a probability distribution built from the data set described in section 2.2.1.

Algorithm Structure and Boundary Conditions

The algorithm loops through each coordinate in the lattice, (i,j), defined by a domain size of $I \times J$ to calculate the radiant temperature and assign the discrete stage number to the cell. The first two stages calculate the radiant temperature of a particular cell using the temperatures of the surrounding neighbors. For this process, we use the Moore neighborhood defined as

$$\{(i+a, j+b) \,|\, -1 \leq a,b \leq 1; a,b \in \mathbb{Z}\}. \tag{2.1}$$

In the event that a particular coordinate (i,j) lies on the boundary of the domain, we only consider those coordinates defined within the domain as part of the equations. Meaning, if we are calculating the ambient temperature of the corner coordinate $(1,1)$, we would only consider the three existing neighbors, $(2,1),(2,2)$, and $(1,2)$ in the calculation. For more information regarding the ambient temperature function, please see section 2.1.1 and equation 2.3.

Stages one and two: Stability and Warming

To begin, we initialize the entire domain as the base temperature for the day on which the burn is to take place, T_B, which we define as stage one, *stable*. To start the fire, we synthetically raise the temperature to ignition for a chosen group of cells and set them to stage three, *rising*.As the heat from these initialized cells approaches the neighbors, radiant and convective heat transfer causes the temperature to rise and results in the transition into stage two. Within stages one and two, we use a modified Newton's law of cooling equation to represent how the radiant temperature at timestep $n+1$ is affected by the ambient temperature of the neighboring area at timestep n.

$$T_{n+1}(i,j) = T_n(i,j) + k(i,j)\left[A_n(i,j) - T_n(i,j)\right]. \tag{2.2}$$

Here, $A_n(i,j)$ is the ambient temperature calculated from the neighboring cells with a weighting function $W(i,j)$ at the previous timestep as follows:

$$A_n(i,j) = \sum_{a=-1}^{1}\sum_{b=-1}^{1} W(i+a,j+b)T_n(i+a,j+b). \tag{2.3}$$

In stage one, $W(i,j) = 1/N \; \forall \; i,j$, where N is the total number of neighbors in the calculation. This along with (2.3), leads to $A_n(i,j) = T_n(i,j)$. From (2.2), we therefore have $T_{n+1}(i,j) = T_n(i,j)$ and the temperature does not change. In stage two, since heat is present, we apply a multiplicative factor of 1.2 to $W(i,j)$, which represents the addition of convective heat transfer as the flames encroach on the area while the radiant temperature increases. Once the temperature rises to inside the bounds of the ignition interval such that $T_n(i,j) \in [I_{min}, I_{max}]$, a cell can undergo one of three options: (i) remain in stage two, *warming*, (ii) transition into stage three, *rising*, or (iii) transition into stage five, *cooling*. If $T_n(i,j) \in (I_{min}, I_{max})$, using the moisture content, m_c, the cell attempts to ignite between D_{min} and D_{max} times, based on a uniformly distributed parameter delay matrix, D, which will be explained in detail in section 2.2.3. If the attempt fails, the cell remains in stage two. If the attempt succeeds, the cell transitions into stage three. If we have $T_n(i,j) > I_{max}$, the cell automatically transitions into stage three, *rising*. If all attempts fail, the cell transitions into stage five. A transition from stage two to stage five represents a cell that will not ignite due to the chemical structure of the fuel in that cell. For instance, this could represent a rock that will heat up but never ignite. Figure 2.2 shows how a particular cell might move through stages two to five, each of which is described in the subsequent subsections.

Stages three and four: Rising and Falling

If the cell ignites, the chemical and physical characteristics of the fuel become the driving forces in how the radiant heat rises and falls. Since the fuel is now being consumed, the area begins to generate its own heat. Thus, for stages three and four, we move away from Newton's law of cooling and define two linear functions for how the heat changes from one timestep to the next. For stage three, rising, we have:

$$T_{n+1}(i,j) = T_S(i,j) + \frac{T_M(i,j) - T_S(i,j)}{R(i,j)}(n - S(i,j)), \tag{2.4}$$

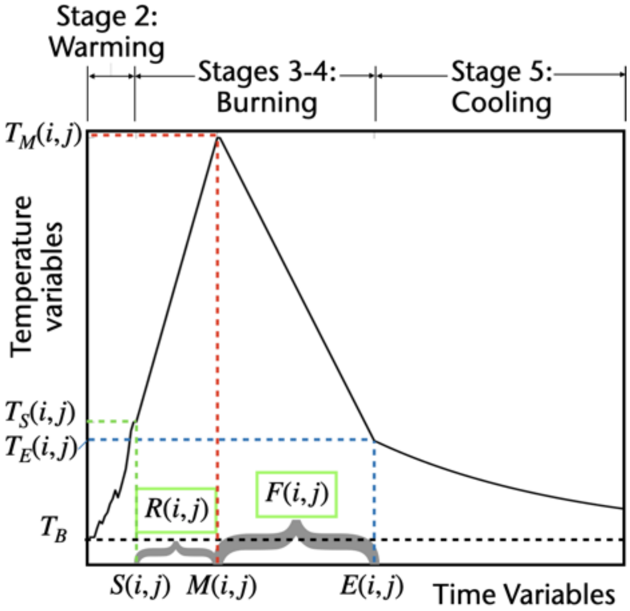

Figure 2.2: *Representation of how the radiant temperature changes in a specific cell over time beginning in stage two, warming, where Newton's law of cooling is applied, moving through the linear equations developed for stages three (rising) and four (falling) and ending in stage five, cooling.*

and for stage four, falling, we have:

$$T_{n+1}(i,j) = T_M(i,j) - \frac{T_M(i,j) - T_S(i,j)}{F(i,j)}(n - M(i,j)). \tag{2.5}$$

For simplicity, stages three and four are defined as linear functions in which the cell rises to its maximum temperature, $T_M(i,j)$ over $R(i,j)$ timesteps, and falls from $T_M(i,j)$ over $F(i,j)$ timesteps. Since the temperature at which the transition into stage three occurs is not set but determined through the use of the delay matrix, $D(i,j)$ interacting with the ignition interval (I_{min}, I_{max}), we define $T_S(i,j)$ to be the ignition temperature for location (i,j) and $S(i,j)$ to be the timestep at which the transition occurs. Then $M(i,j)$ is the timestep at which the maximum temperature is achieved. During stage four, once the cell reduces in heat back down to the ignition interval, $[I_{min}, I_{max}]$, the cell is again tested to see if it has extinguished. The temperature at which the cell extinguishes is defined as $T_E(i,j)$ at timestep $E(i,j)$, and we transition into stage five.

Stage five: Cooling

This stage represents the time when the fuel has been consumed, and the ground beneath the fuel is cooling off back down to equilibrium with the area's temperature, T_B. We use an exponential function to show how the heat dissipates after the fire has moved through the area:

$$T_{n+1}(i,j) = (T_E(i,j) - T_B)\exp\left(\frac{E(i,j)-n}{T_E(i,j)-T_B}\right) + T_B. \tag{2.6}$$

This is the last stage of the process. Once the cell reduces back down to T_B, it is considered to be burnt and is no longer subject to any temperature changes.

2.2 Parameters and the data set

SERF was built from a large data set developed in the New Jersey Pine Barrens from 2017 through 2021 during several controlled burns, under a grant from SERDP (Strategic Environmental Research and Development Program) within the Department of Defense. The data was collected by the Northern Research Station of the United States Department of Agriculture (USDA) Forest Service (Kremens 2019). In this section, we describe the extent of the data set and how we incorporated this data into the model.

2.2.1 The Data Set

There were two types of fires that were burned under this grant: square fires with 12-meter length sides, and 30-acre fires. Both were prescribed and kept under tight surveillance. The 12-

meter fires were outfitted with a truss at six feet over the burning zone containing 16 equally spaced data collection devices in a four-by-four grid (see Fig. 2.3). Each device housed a FLIR Lepton® 1.5 that recorded infrared information, and a digital camera along with various other data collection devices. The fuel below the cameras for the 12-meter burns was collected, weighed, and evenly distributed throughout the burn zone. For the 30-acre fires, the devices were distributed randomly throughout the burn zone.

All of the cameras were initiated simultaneously and began taking snapshots of the area at one-second intervals. The FLIR Lepton® 1.5 recorded the infrared radiant output (from $8-14$ microns) emanating from each cell in the viewing range and outputted a numerical array with values ranging from approximately 8000 to 16000. The prescribed fires were ignited below the cameras and allowed to burn through the area underneath (Kremens 2019). For the 12-meter burns, the viewing area for each camera was approximately 3 meters square, but the resulting numerical array was presented as 60×80 cells. Figure 2.3 shows the setup for the data set collection. Please note that due to the Covid-19 crisis, we could not perform the necessary experiments to determine the exact spatial region captured by each camera by calibrating the digital and infrared cameras together; this should be done in the future.

Since each segment of ground was individually recorded, we first found all of the arrays related to a particular fire in a given section and stacked the arrays on top of one another in a three-dimensional time-sequential tensor (dimensions being x and y spatial dimensions with time as the third). Out of 3.1 million files, we could find 74 successful fire visualizations that did not have any deformities. We denote these 74 fire visualizations using the symbol f_m, where m is the fire index that goes from 1 to 74, that is the set $\{f_m\}_{m=1}^{74}$ represents these 74 successful fire visualizations.

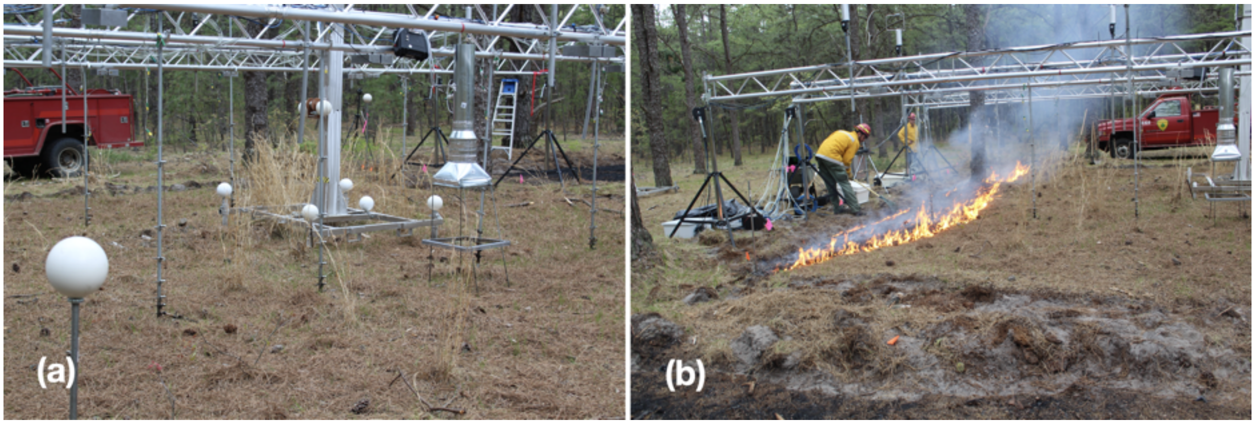

Figure 2.3: *Truss setup in the New Jersey Pine Barrens for the creation of the data set; (a) Before the burn; (b) After burn was initialized; Photos courtesy of Dr. Robert Kremens, Chester F. Carlson Center for Imaging Science, Rochester Institute of Technology (RIT); credit: USDA Forest Service Northern Research Station.*

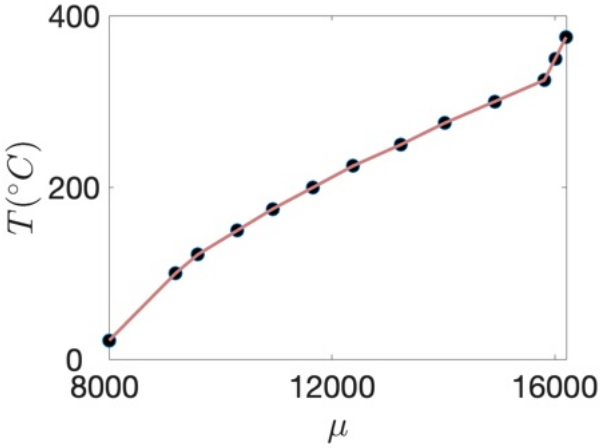

Figure 2.4: *Calibration graph for relating infrared output data to radiant temperature values from observations using a black box unit with the FLIR Lepton*® *1.5 camera.*

From laboratory experiments performed with the Lepton® camera, the infrared values were found to correspond to a radiant temperature flux range of approximately 22°C to 400°C (FLIR 2018). For the interpolation scheme, we first attempted a cubic spline interpolation but the results were similar to the linear interpolation, and thus the linear was chosen for simplicity. Note the sudden increase towards the top right of the graph in Fig. 2.4 that indicates the temperature data may not be entirely accurate towards the upper bound for the range of temperatures recorded. This is reflected in the maximum temperatures for the power flux being capped at $T_M = 400°\text{C}$. This anomaly was adjusted in the model so that some of the maximum temperatures can be above this value, but without accurate data for that range, it is possible that the resulting maximum radiant temperature estimations may be lower than the true values.

2.2.2 Data-Driven Parameters

From the data set, we obtained several parameters for SERF including two global parameters: the ignition interval, $[I_{min}, I_{max}]$, and the unburnt proportion of land $U(f_m)$ for a fire instance f_m; and four cell-dependent input parameter matrices: the maximum temperatures, T_M, the rise and fall times, R and F, and the heat coefficients, k. Each of the input parameter matrices used in the model is defined using a probability distribution taken from all of the cells in the data set fires. We experimented with fitting several different probability distributions to the data. Since we cannot assume that our data parameters adhere to any specific distribution, we chose the kernel distribution since it led to the most accurate model outputs compared to the observational data.

For R, F, T_M, and k, SERF builds the input matrices by assigning values to a subset of cells through sampling the corresponding distribution defined by the data set, and then “smoothing” these numbers to increase realistic stability in the model. For R and F, a random number between 50% and 70% of the cells are assigned a value with the rest equal to 1. For k and T_M, all cells are assigned a value from their respective probability distributions.

The smoothing process for each of the four parameter matrices is performed by finding the sum of each cell and its immediate neighbors, and then multiplying that by a random number chosen from a normal distribution:

$$P'(i,j) = p \sum_{a=-1}^{1} \sum_{b=-1}^{1} P(i+a, j+b) \tag{2.7}$$

where $P \in \{R, F, k, T_M\}$, and $p \sim \mathcal{N}(\mu = 1, \sigma = 0.04)$. This process is repeated twice for R, F, and k, and ten times for T_M. Then the values are normalized back to the original interval by finding the maximum value of the original matrix, $max(P)$ and dividing that by the maximum value of the new matrix $max(P')$:

$$P(i,j) = P'(i,j) \frac{max(P)}{max(P')}. \tag{2.8}$$

Figure 2.5 shows a sample T_M matrix, where Fig. 2.5(a) shows the initial sample matrix and Fig. 2.5(b) shows the matrix after smoothing.

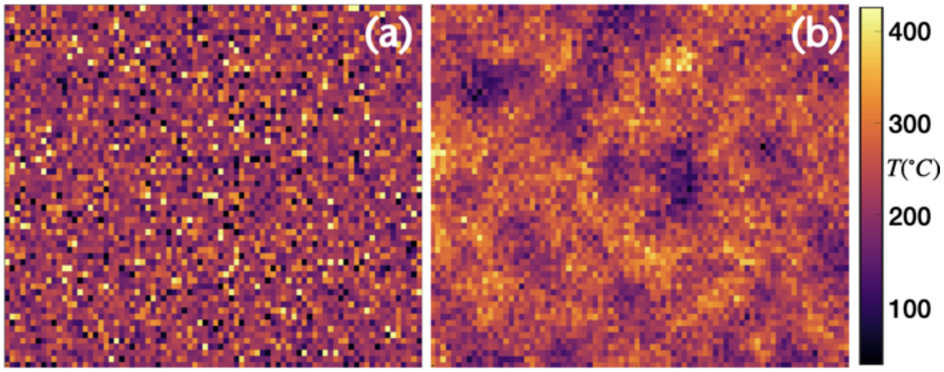

Figure 2.5: *A representative sample of T_M matrix and a smoothed version used in SERF: (a) Initial T_M matrix with values sampled from the distribution for maximum temperatures; (b) T_M matrix after smoothing.*

The Ignition Interval: $[I_{min}, I_{max}]$

The fuel for the $12m^2$ prescribed burns was a mixture of live and dead needles, leaves, and brush, and was gathered from the area designated for the fire, weighed, then dispersed as evenly as possible throughout all 16 sections of each burn zone (Kremens 2019). The 30-acre fires held a mixture of the same but more heterogeneously distributed. As ignition temperatures vary widely for these different fuels, we needed to find a reasonable interval, $[I_{min}, I_{max}]$, for ignition temperatures represented in these fires, $\{f_m\}_{m=1}^{74}$.

Since we had chosen the set of fires to be those known to ignite, we could estimate the second of ignition to be the timestep at which the fire entered the field of view. Using visualizations of the infrared value tensors, we came up with an equation for the average temperature of the cells based on the maximum and minimum radiant temperature of each fire, f_m:

$$I_m(f_m) = |0.2(I_{max}(f_m) - I_{min}(f_m))| + I_{min}(f_m). \tag{2.9}$$

The equation was developed by finding the range of temperatures recorded in each fire f_m, $[I_{min}(f_m), I_{max}(f_m)]$, and determining the ignition point for that fire to be approximately 20% of that range above $I_{min}(f_m)$. Then we found the greatest and least value for all ignition temperatures and that defined the ignition interval for SERF. Figure 2.6 shows the various temperatures for each fire in the data set.

From Fig. 2.6 we found that the minimum and maximum values for threshold for each of these fires to be: $I_{min} \approx 90°C$ and $I_{max} \approx 150°C$. Note that Fig. 2.6 also shows the upper bound on the recording device at $400°C$ as described previously in section 2.2.1.

Maximum temperatures

A kernel distribution was fitted to a histogram of the maximum radiant temperatures achieved for each cell in all of the fire tensors, for a total of $355,200$ cells. Figure 2.7 shows the maximum

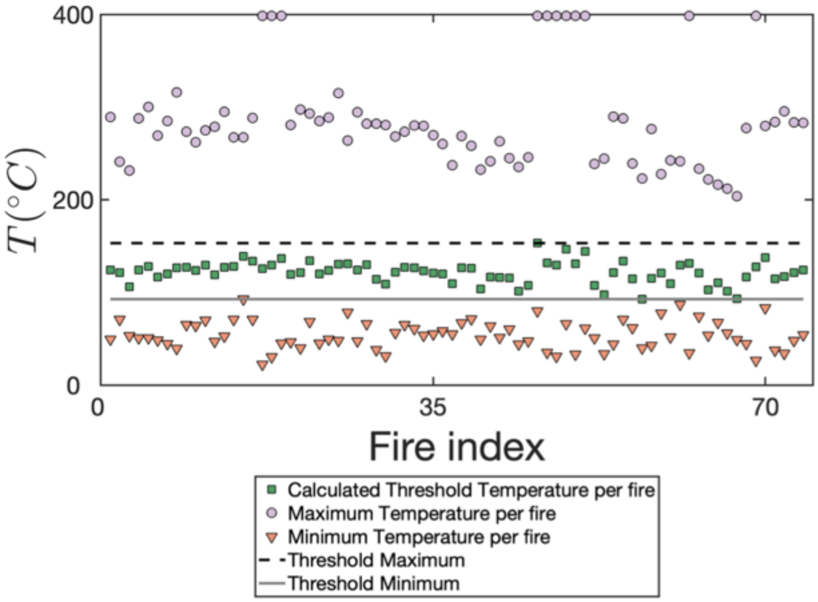

Figure 2.6: *Maximum, Minimum, and Threshold Temperatures for each fire in degrees Celsius and the top and bottom of the threshold interval.*

temperatures for each cell across all fires and the estimated distribution for these quantities. The majority of the fires had a large variance in temperatures across cells, resulting in various local maxima in the distribution. Moreover, there were some fires in which the entire area was engulfed in flames that all burned at the upper bound of the Lepton device. The tall bar at the right end of this graph in Fig. 2.7 represents these high-intensity fires. A large number of cells reached around 200 degrees indicating that most of the cells caught fire but did not release significant heat energy. The smaller local maxima around 300 degrees indicates that certain fires maintained a higher temperature than average but did not reach the upper bound. In short, the variety of different fires begot various maximum temperatures.

This kernel distribution was then sampled to initialize all cells in the T_M parameter matrix. The "smoothing" process was then applied as described in section 2.2.2. Each cell was "smoothed" to allow for more even heating temperatures in neighboring cells.

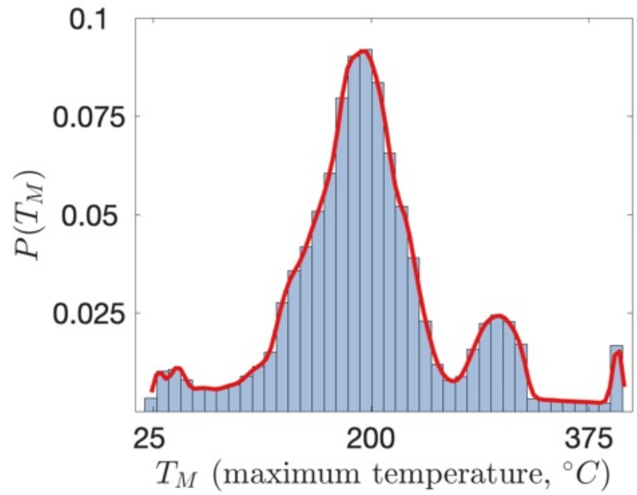

Figure 2.7: *Recorded maximum temperatures for* 355,200 *cells from all fires in the data set; histogram and fitted kernel distribution (red line).*

Rise(R) and Fall (F) Times Distributions

Using the ignition temperature defined for each fire (see section 2.2.2), we measured the number of timesteps, $R(i, j)$, required for the temperature in each cell to go from the starting ignition temperature, $T_S(i, j)$, up to maximum temperature $T_M(i, j)$ and the number of time steps $F(i, j)$ to fall from $T_M(i, j)$ back to the ignition temperature. Figure 2.8 shows the distribution of R and F derived from the data. The red lines in this figure are the corresponding kernel density estimate. We experimented with various probability distributions including joint distributions for these parameters and found that the kernel distribution with each R and F value sampled separately produced results that most closely matched the data set fires. The average rise time , $\langle R \rangle = 26$ seconds, and the average fall time $\langle F \rangle = 58$ seconds. These histograms indicate a strong likelihood that the rise and fall times would be relatively low, although it is possible to have a long tail during the cooling stage.

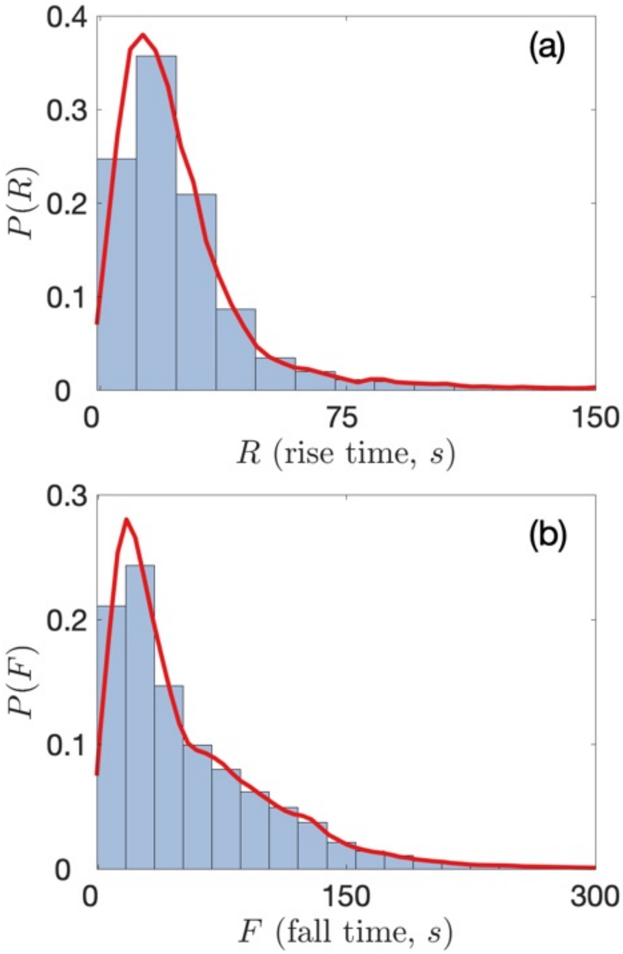

Figure 2.8: *Rise (a) and fall (b) time value histograms and kernel distributions from the data set.*

Heat Coefficient Array (k-matrix)

The heat coefficient for a given material is typically determined as the likelihood of a given substance to transfer heat to a neighboring material. Sometimes referred to as “conductance,” it is the primary parameter in Newton’s law of cooling which was used for the rising of the temperature during stages one and two, and the transition into stage three. We determined the probability distribution of these coefficients from the data set by finding the global maximum temperature achieved for all cells in a given fire and then estimating the ratio of the maximum temperature for each cell to that global value. This gave us a number between 0 and 1 that we used to represent the "burnability" of that particular cell. We created a histogram and fitted a kernel distribution to the data. Figure 2.9 shows the results of that distribution. We note that the majority of the calculations of k lie between 0.7 and 0.95, which implies that the radiant temperatures for each cell were relatively close to the global maximum for that fire. This accounts for an approximate mean of 0.0855 for the unburnt proportion of land, U, and also indicates that most of the cells reached temperatures above I_{max}. The values for the k parameter matrix are sampled from this probability distribution for each cell in the domain. The matrix is then "smoothed" according to the method described at the start of section 2.2.2. As with the other cell-specific parameter matrices (R, F, and T_M), we experimented with various probability distributions for these values but found the kernel distribution to represent the heat coefficients most accurately in comparison with the data set.

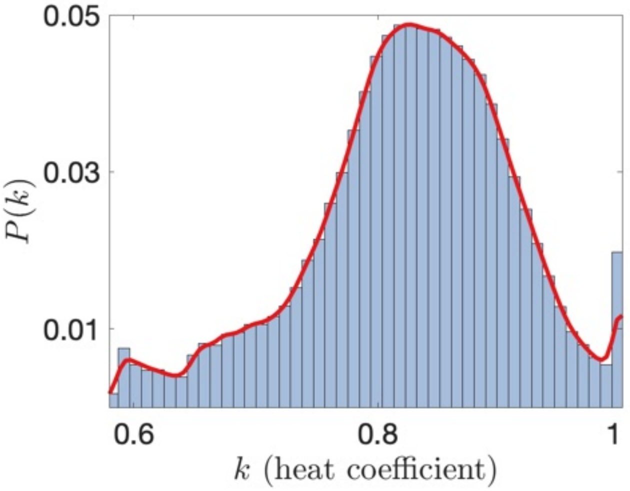

Figure 2.9: *Heat coefficient histogram with kernel distribution; found largest temperature value in the maximum temperature matrix for each fire and the proportion of that maximum reached by each cell.*

Initial Conditions

From the visualizations of the data set fires, we found four initial conditions represented: corner, side, chunk, and double chunk. Figure 2.10 shows examples of these initial conditions from the simulations alongside data set representations of each type (the left images are from SERF simulations and the right from the data set). It should be noted that the orientation of the cameras was not standardized when they were placed along the truss, which means that the fire traveled in several directions on camera. For SERF, the fires all move in the same direction with a standardized trajectory of west to east, or south to north within the view frame.

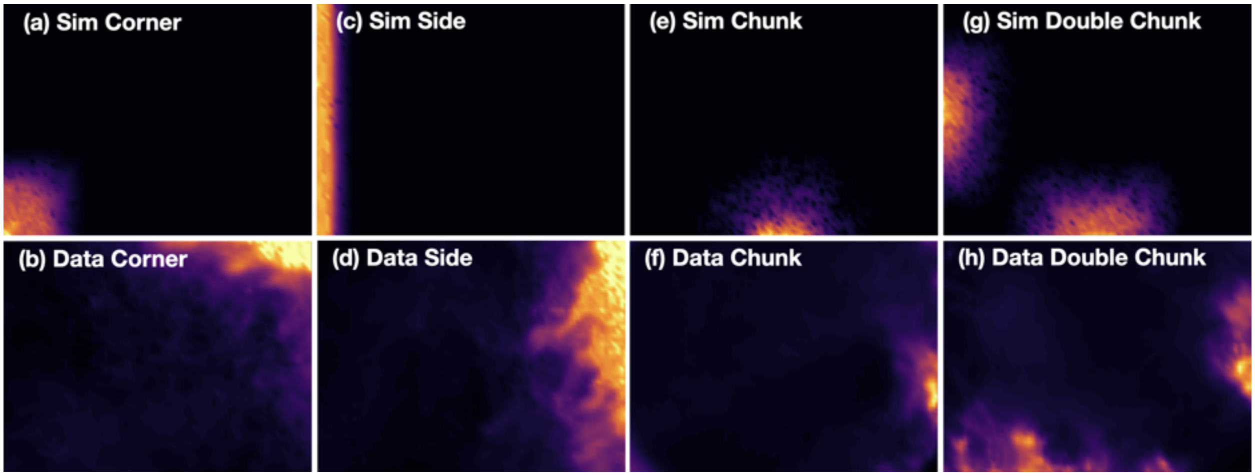

Figure 2.10: *Initial Conditions: a) corner from* $\{S_m\}$*, b) corner from* $\{f_m\}$*, c) side from* $\{S_m\}$*, d) side from* $\{f_m\}$*, e) chunk from* $\{S_m\}$*, f) chunk from* $\{f_m\}$*, g) double chunk from* $\{S_m\}$*, h) double chunk from* $\{f_m\}$*.*

We also incorporated an initial condition that was not represented in the data set. It is widely known that spotting occurrences in wildfires can accelerate the spread of the fire, and understanding this phenomenon is an important part of keeping prescribed fires under control (Koo et al. 2012; Manzello et al. 2020). Therefore, we added more simulations with a fifth initial condition of spotting, where we ignited three spots in the middle of the domain (see Fig. 2.11).

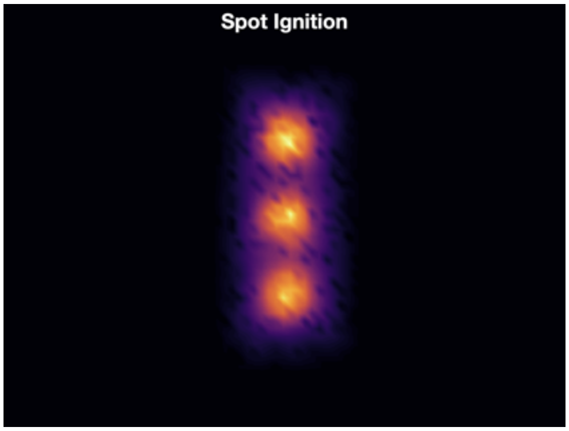

Figure 2.11: *Spotting initial condition, added to the simulations to analyze fires beyond what was represented in the data set.*

As described in section 2.1.1, these initial conditions were used to synthetically raise the temperature of a particular set of cells at the start of the simulation. Each of these cells were raised to I_{max} for the CML model and the stages set to three in the CA model. Section 2.5 has examples of each ignition type from the data set and the simulations, including a set of images from the spotting ignition. Of note in these images are that the timing varied greatly for the length of the fires within the viewing area, but the simulation versus the data set image sets are quite similar in structure.

Distribution for Unburnt Area

For verification purposes, we used the unburnt proportion of land in each fire from the data set, $U(f_m)$, by determining the mean, $\langle U(f_m)\rangle$ of this parameter (the mean is taken over $\{f_m\}_{m=1}^{74}$, the fire instances). To find the proportion of cells that did not ignite and therefore did not burn, we used the ignition values represented in Fig. 2.6 and described in section 2.2.2, and defined each of the cells as burnt if they achieved the ignition temperature for that particular fire, or unburnt if they did not. We counted the number of cells whose final state was burnt, out of the total number of cells in each fire and created a matching exponential distribution. Figure 2.12 shows the histogram with the fitted exponential. When we fit the curve for the proportion of land that did not burn, we found that $\langle U(f_m) \rangle = 0.0855$.

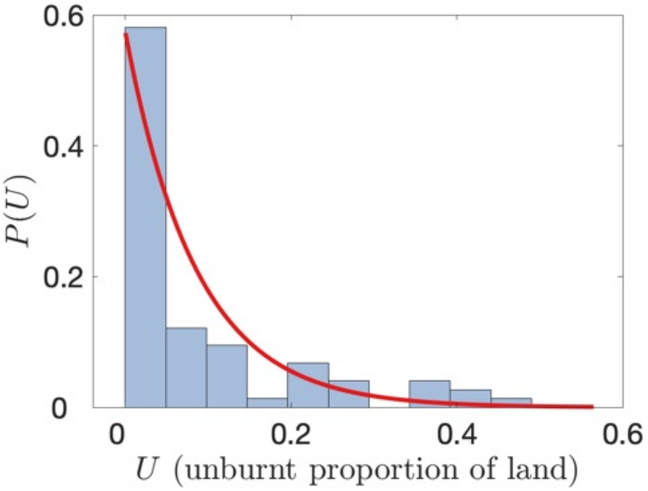

Figure 2.12: *Histogram of the proportion of cells that did not burn in each fire from the data set (U). The exponential curve fitted to the histogram shown here in red has a mean of $\langle U(f_m) \rangle =$ 0.0855.*

2.2.3 Non-Data-Driven Parameter:Moisture Content: m_c

Although moisture information was not available for the data set, fuel moisture levels have a major impact on fire behavior (Blauw et al. 2015; Torres et al. 2018). To appropriately use the moisture content in the simulations, we needed to associate that value, m_c, with whether or not the cell would ignite. To do this, we use this moisture level as a threshold to decide if the temperature will change for that cell for a given timestep. For each cell, we randomly generate a uniformly distributed number between 0 and 1 and if the number is below m_c, then we set $T_{n+1}(i,j) = T_n(i,j)$ and the algorithm skips to the next cell. This allows for a slower rate of spread when the moisture level is higher.

When testing the effect of the moisture content in the simulations, we found that while this random uniform number had an effect, the speed of the fires in the data set were still slower than those achieved with m_c. Thus, to accentuate the effect of m_c, we created a parameter matrix to delay the ignition, $D(i,j)$, in which each cell was assigned an integer between 1 and 10 from a uniform distribution for how many times SERF attempts to ignite that particular cell. The matrix was then smoothed using the method described in section 2.2.2, and returned to integers. This delay value is used to test the transition from stage two to stage three. If the cell does not ignite within $D(i,j)$ attempts at ignition, the cell is considered nonflammable and the algorithm transitions that cell from stage two directly into stage five, cooling. As with the other parameter matrices, this matrix was built by assigning values as described above to all of the cells in each simulation and then "smoothing" the values across the domain.

2.3 Results and Discussion

We performed a total of 100 SERF simulations, $\{S_m\}_{m=1}^{100}$ with 20 of each initial conditions described in section 2.2.2. A simulation begins with a synthetic rising of the temperature to I_{max} and setting the cell stage to three for a collection of cells. A simulation is considered complete when all cells have reached stage five. We collected the fire simulation tensors, parameter matrices, and a variety of other useful information from each simulation so that we could analyze the results. Since the data set was collected at one-second intervals, each $I \times J$ matrix produced from the algorithm is considered to be one second in the life of the fire.

To verify SERF, we compared several metrics from the simulations to the data set, including the likelihood of transition between stages, burning potential for each cell, the proportion of land that remained unburnt, and two timing metrics for spread rates. Each is described in detail in section 2.3.1.

To validate SERF, we compared the output to a typical CA model without the underlying CML model to show the strengths of adding the ability to achieve a continuous set of outputs for determining the states of the system. The results of these tests are described in detail in section 2.3.2.

2.3.1 Verification

The combination of all of the probabilistic parameter inputs with the smoothing function described in section 2.2.2, the uniformly distributed moisture content and delay matrix, and the stochastic values generated in the algorithm makes SERF inherently probabilistic. Thus, we were able to use several input parameter distributions as metrics to calibrate and verify the model. We ran several sets of simulations and compared the outputs to these parameters as metrics derived from the observational data. In particular, we compared unburnt areas $U(f_m)$ for each fire in $\{f_m\}_{m=1}^{74}$, the distribution of maximum temperatures, and the distributions of rising and fall times.

Transition Matrices

To test the overall effectiveness of the CA model, we developed a transition matrix for the data set fires $\{f_m\}_{m=1}^{74}$ and the SERF simulations $\{S_m\}_{m=1}^{100}$ showing the probability of moving from one stage to another, calculated and averaged over all cells in the fires and simulations separately. The transition matrices were then created for the fires and SERF. Figure 2.13 shows the difference between the transition probabilities for the fires and the SERF simulations.

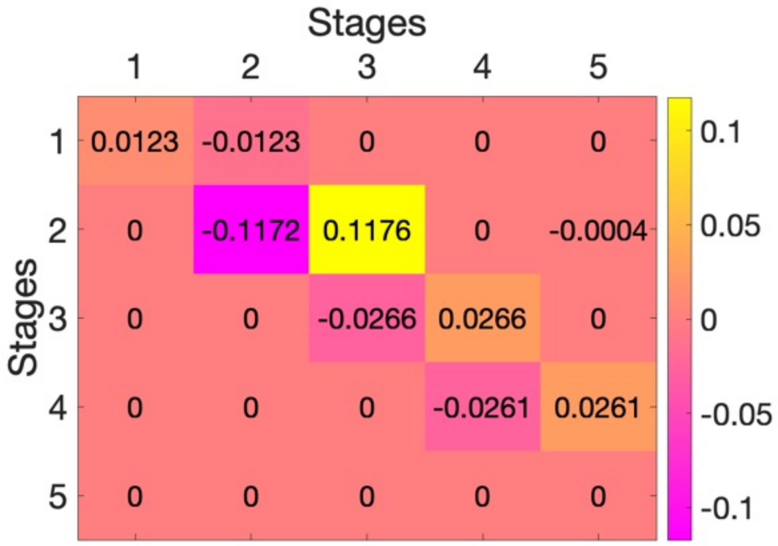

	1	2	3	4	5
1	0.0123	-0.0123	0	0	0
2	0	-0.1172	0.1176	0	-0.0004
3	0	0	-0.0266	0.0266	0
4	0	0	0	-0.0261	0.0261
5	0	0	0	0	0

Figure 2.13: *Percentage differences in stage transition probabilities for the SERF simulations versus the data set. The simulations reproduce the transition probabilities with an error of less than* 3% *for all cases except the stage two to three transition where the error is* 12%*.*

Due to the probabilistic nature of the algorithm, each set of simulation results were unique in their comparison to the data set. Using the parameter values and ranges we chose, the resulting differences ranged from a maximum difference of 11% to 12% in transition from stages 2 to 3. We have chosen to show a matrix representing an 11.76% maximum difference in figure 2.13. The rest of the differences were less than 3% for all sets of simulations indicating that SERF successfully captured the transition probabilities for each stage. Other metrics that were compared with the data set including unburnt proportion of land and the heat coefficient ranges showed no major changes between the various simulation runs.

Heat Coefficients: Vegetation Burning Potential

The heat coefficients assigned to each cell represent the likelihood of the fuel burning. A low heat coefficient indicates a low probability of ignition, as in the case of a cell that is dominated by the presence of a rock or dirt, as opposed to leaves or branches, which would represent a higher heat coefficient. Initialized using the distribution from the data set as defined in section 2.2.2, the final heat coefficients were also affected by the moisture content, m_c, and the delay matrix, D. Figure 2.14 shows the heat coefficients of each cell from every simulation in comparison to those determined from the data sets. The mean of the heat coefficients for SERF is approximately 0.8351 and the mean for the data set is 0.8264, a difference of .0087. In Fig. 2.14, we observe that the variance of the simulations and data set are relatively close, and the median values represented by the red lines are 0.8325 and 0.8347 for the data set and simulations respectively, which indicates a difference of only 0.0022 and a successful representation of the heat coefficients for the data set in the model.

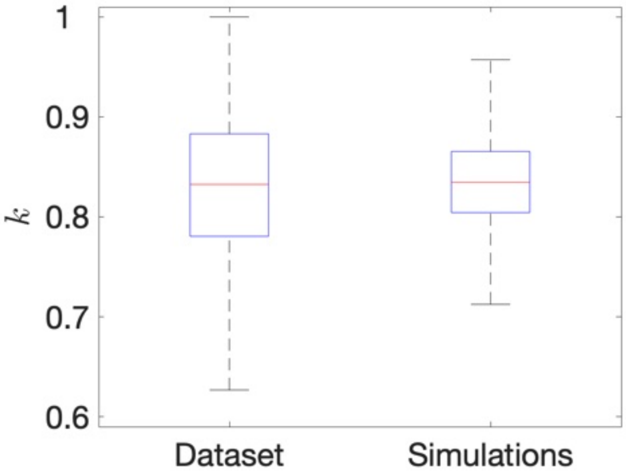

Figure 2.14: *Box plot comparing the heat coefficients in the SERF simulations and the data set; the red line in the middle of the boxes indicates median values. Observe the relative similarity between k in the data set and SERF simulations.*

Unburnt proportion of land

Another metric we used to determine the success of SERF was to see if the unburnt proportion of land (U) was similar between the simulations and the data set. Figure 2.15 shows a box plot that exhibits the success of this metric. For SERF, we estimated U by finding the proportion of cells that transitioned from stage two to stage five, without ignition. T_A, M, D, and k influenced U. The mean of U in the SERF simulations is 0.0865, and in the data set, 0.0867 for a difference of 0.0002. The medians (represented as the red line in the box plot) are 0.0293 and 0.0125 for the data set and simulations respectively which exhibits a difference of only 1.68%. The variance of U differed, with the simulations creating slightly more variance than the data set.

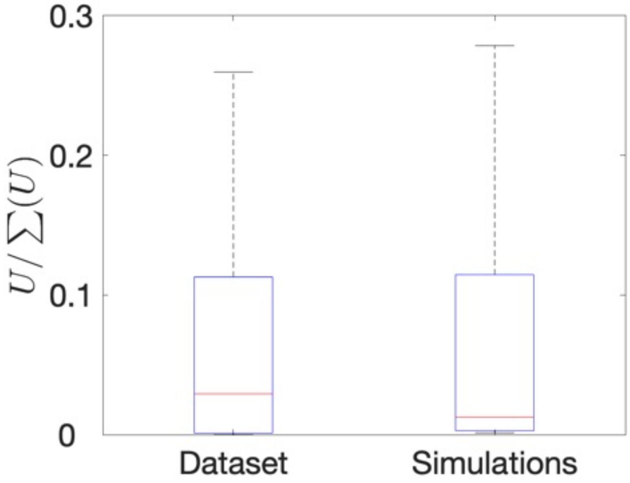

__Figure 2.15:__ Box plot showing the unburnt proportion of land in the SERF simulations compared to the data set. Observe the relative similarity between U in the data set and simulations.

Lingering Embers

Often in a fire, particular spots continue to burn long after the bulk of the fire has dissipated. This phenomenon has to do with the density and moisture level of the fuel on the ground. A more moisture-rich fuel takes longer to burn because the water must be evaporated off before the fuel can be consumed, and a denser area lacks the ability to draw in the oxygen as freely so the combustion process slows. Understanding the length of time embers may linger during a prescribed burn could inhibit the introduction of firebrands into the surrounding foliage long after the area has burnt. In the data set, 29 of the 74 fires showed obvious evidence of lingering embers. However, many of the data set visualizations were cut short from the full length of the fire if the embers burned at a low temperature, so some lingering embers may have been lost. Figure 2.16(a-b) shows some images from the data set fires representing this phenomenon and Fig. 2.16(c-d) shows the same behavior from the simulations. In the SERF simulations, this originates from the probabilistically determined rise and fall times of each cell in conjunction with the varying start time for the ignitions. Some of those values add up to a long burn for a particular group of cells.

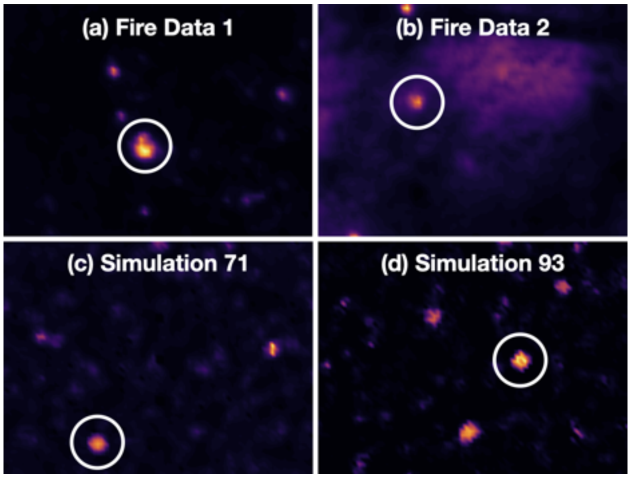

Figure 2.16: *Lingering embers in the simulations and fire data sets; (a)* f_8, *second* 500 *of* 1100*; (b)* f_{50}, *second* 2550 *of* 2894*; (c)* S_{71}, *second* 2000 *of* 2310*; (d)* S_{93}, *second* 900 *of* 1241.

Cell rise and fall relationship with fireline

Many CA models focus on the speed of the fireline as it moves through the area because that gives an indication of how quickly it will take over a given area outside of the burn zone. However, the time the fire spends in any given area can also make a huge difference to fire practitioners because of the likelihood of firebrand transport, lingering embers, and smoke production. SERF accurately represents the variance in how long the fire spends in any given area. Figure 2.17 displays some stills from SERF simulation number 30 that exhibit the length of time the fire spends in the domain.

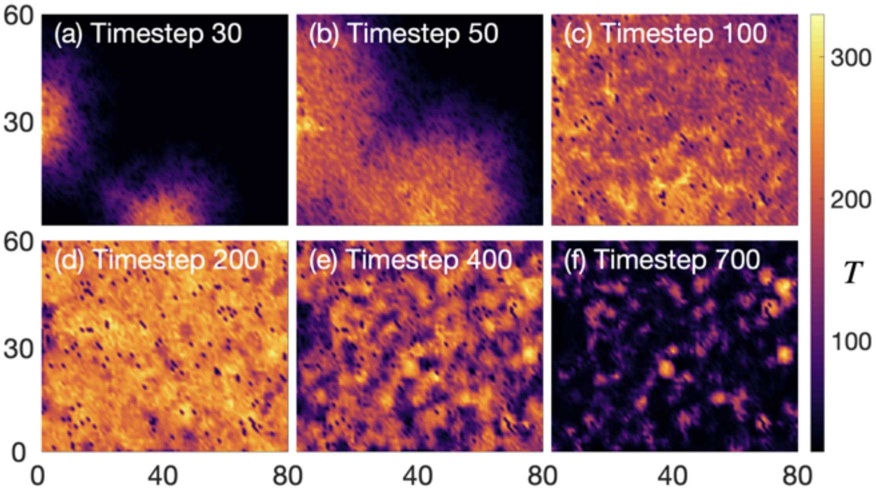

Figure 2.17: *Successful representation of the lingering heat after the fireline moves through the area; images from SERF simulation number* 30*; a) timestep* 30*; b) timestep* 50*; c) timestep* 100*; d) timestep* 200*; e) timestep* 400*; f) timestep* 700.

2.3.2 Validation: Comparison to Basic CA

To validate mathematical models, we compare the model output against known fire behavior and analyze any similarities or differences. For SERF, we made a direct comparison to a much lower complexity CA model. We began this project by constructing our own basic square-cell CA model. For this basic model, each cell is in one of three states: burned, unburnt, or burning, so that $B_n(i,j) \in \{0,1,2\}$ respectively for each cell, (i,j) and time step n. The only parameter represented in this basic CA model is a heat coefficient for each cell uniformly distributed between 0.5 and 1 such that $\forall(i,j), k(i,j) \sim \mathscr{U}(0.5,1)$.

All cells are initialized with a value of unburnt, $\forall(i,j), B_0(i,j) = 1$. We "ignite" a fire by assigning a selection of cells to the burning stage, such that $B_0(i,j) = 2$ for those cells. With each time step in the loop, each cell that is currently burning may cause a neighboring cell to transition into the burning stage by a factor that is based on wind direction and speed. With wind speed $W = 0\ m/s$, the factor governing any of the eight neighboring cells transitioning to burning is 0.5. With a wind speed greater than 0, the factor increases by $0.4 \times W/5$ in the direction of the wind, and $0.3 \times W/5$ for the neighboring cells to the wind direction, and reduces by $0.4 \times W/5$ in the opposite direction from the wind and $0.3 \times W/5$ for the neighboring cells in opposition to the wind direction. The cells perpendicular to the wind direction remain with a transition factor of 0.5. The 5 in the denominator for each of these values minimizes the effect of the wind for slower wind speeds below 5 meters per second. For instance, if we set the wind direction to NW (meaning the wind is coming from the NW) and the wind speed to 5, then we have the following factor matrix for the neighboring cells of a particular cell $B_n(a,b)$ transitioning into the burning state:

$$\text{if } B_n(a,b) = 2$$

$$\mathscr{F}\begin{bmatrix} (a-1,b+1) & (a,b+1) & (a+1,b+1) \\ (a-1,b) & (a,b) & (a+1,b) \\ (a-1,b-1) & (a,b-1) & (a+1,b-1) \end{bmatrix}$$

$$= \begin{bmatrix} 0.1 & 0.2 & 0.5 \\ 0.2 & 0 & 0.8 \\ 0.5 & 0.8 & 0.9 \end{bmatrix} \tag{2.10}$$

The new values of the cells are then calculated as the sum of the originally assigned heat coefficient value described in the first paragraph with these factors above, and then we use the ceiling function to define the current state of cell (i, j) as 1 (unburnt) or 2 (burning):

$$B_n(i, j) = \lceil k(i, j) + \mathscr{F}(i, j) \rceil \tag{2.11}$$

If the cell value is unburnt ($B_n(i, j) = 1$), the cell remains available for this transition in subsequent time steps. If the cell is burning, ($B_n(i, j) = 2$), the cell will transition to 0 in the next time step and remain at 0 from there on. Thus, in each time step, each cell will achieve one of only three distinct states: $0, 1$, or 2. Once a cell has transitioned into burning, or state 2, the next time step transitions the cell into the burnt state, 0. Therefore, no cell remains burning for longer than one time step. The simulation ends when no cell values are equal to 2, or $\forall (i, j), B_n(i, j) \in \{0, 1\}$.

For comparison to SERF, Fig. 2.18(a-d) shows different time steps from that basic model using a 300×300 grid with winds from the North at 5mph, and Fig. 2.18(e-h) showing the same domain with no winds. From these figures, the fireline clearly defines the next movements through the field of view, and the presence of heavy winds adjusts the fireline significantly. With no winds, this basic CA model represents the elliptical shape of the fireline with concentric contours as portrayed in the other papers (Hernández Encinas et al. 2007; Alexandridis et al. 2008; Yassemi, Dragićević, and Schmidt 2008; Progias and Sirakoulis 2013; Ghisu et al. 2015; Gennaro et al. 2017; Mahmoud and Chulahwat 2017; Zheng et al. 2017; Liu et al. 2018; Freire and DaCamara 2019). The main

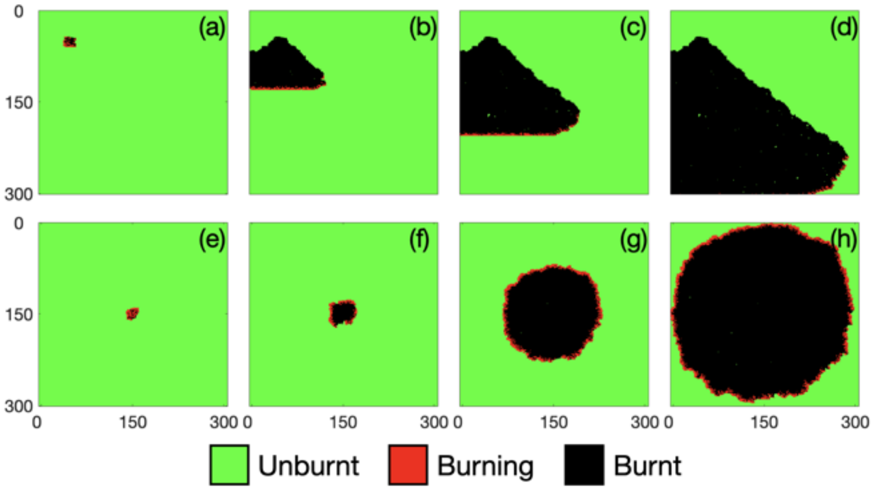

Figure 2.18: 300×300 *grid for a basic CA model with probability of spread weighted by wind; (a-d) Northern winds at* $15mph$*; (a) time step* 5*; (b) time step* 75*; (c) time step* 150*; (d) time step* 250*; (e-h) no winds; (e) time step* 5*; (f) time step* 20*; (g) time step* 80*; (h) time step* 150*.*

difference between this type of CA model and SERF is that the underlying CML model gives us more information regarding parameters other than the location of the fireline. SERF offers an opportunity to potentially learn about how the heat transfers from one area to the next, and includes the time delay between when the fireline crosses through the area and when the fire is completed. These are important features of a prescribed fire to study in order to mitigate the potential for firebrands to be blown outside of the burn zone.

2.4 Conclusion

This chapter describes and analyzes a Spatially Extended Radiant heat Fire model, SERF, combining a CA and CML framework, modeling radiant temperatures with data-driven parameters for fine-scale prescribed fire spread. Using a data set created in the New Jersey Pine Barrens over the course of five years, we built a spatially extended model using probability distributions for several parameters derived from the data set. The use of the data set is unique to SERF and helps to validate the accuracy of the simulations.

While SERF has shown excellent performance in reproducing many of the features of prescribed fires, and it is one of the first non-laboratory data-driven cellular automata models for prescribed fires, some parts of SERF still need refinement. In future work, we plan to explore a variety of modifications to increase its accuracy, as it under-performed in some critical parameter settings. We will perform a more advanced analysis of the SERF simulation outputs to assess how various parameters affect the model's accuracy. Furthermore, we will study the statistical properties of the spatial features of fire.

2.5 Appendix: Output Images

Figures for each of the five initial conditions (ignition types) are listed below. Each set of images from the data represents six particular time steps from the fire data. Each set of images from the SERF simulations represents six time steps from the simulation. Of note within these images is the similarity between the data set and SERF ignition types. Although the timing of each varied greatly, looking at the images clearly shows the successful representation of this data set through this model.

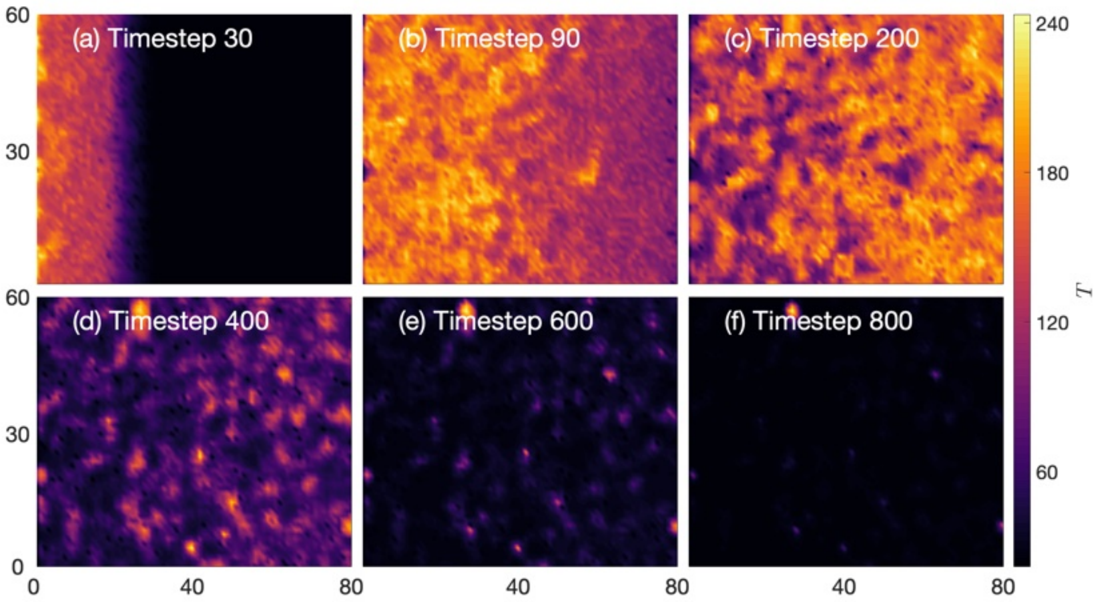

Figure 2.19: *Side ignition: SERF Simulation 4; a) time step 30; b) time step 90; c) time step 200; d) time step 400; e) time step 600; f) time step 800*

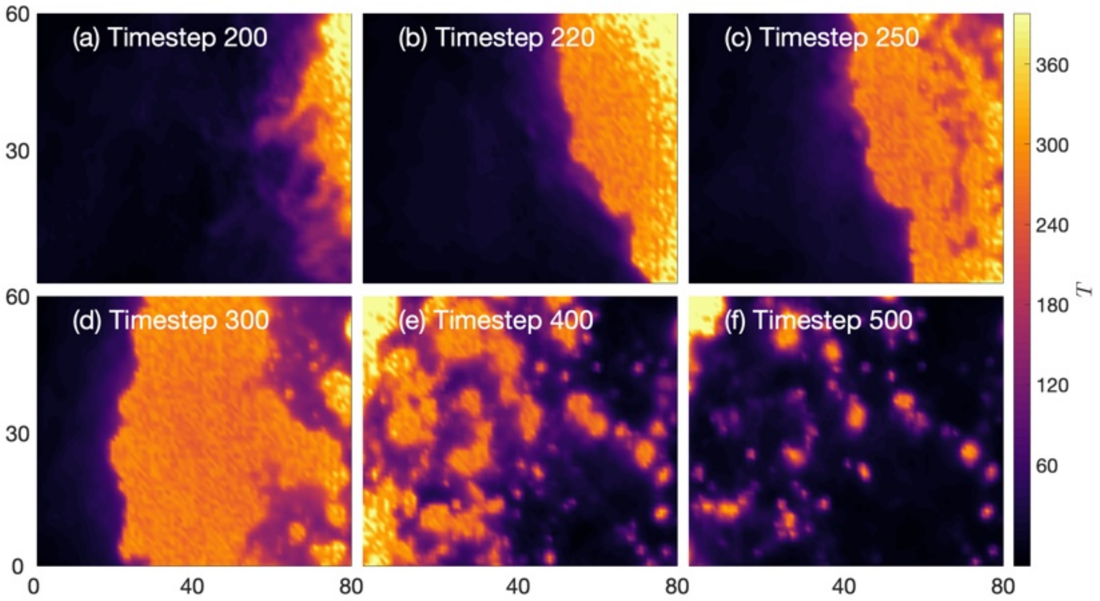

Figure 2.20: *Side ignition: data set Fire 120; a) time step 200; b) time step 220; c) time step 250; d) time step 300; e) time step 400; f) time step 500*

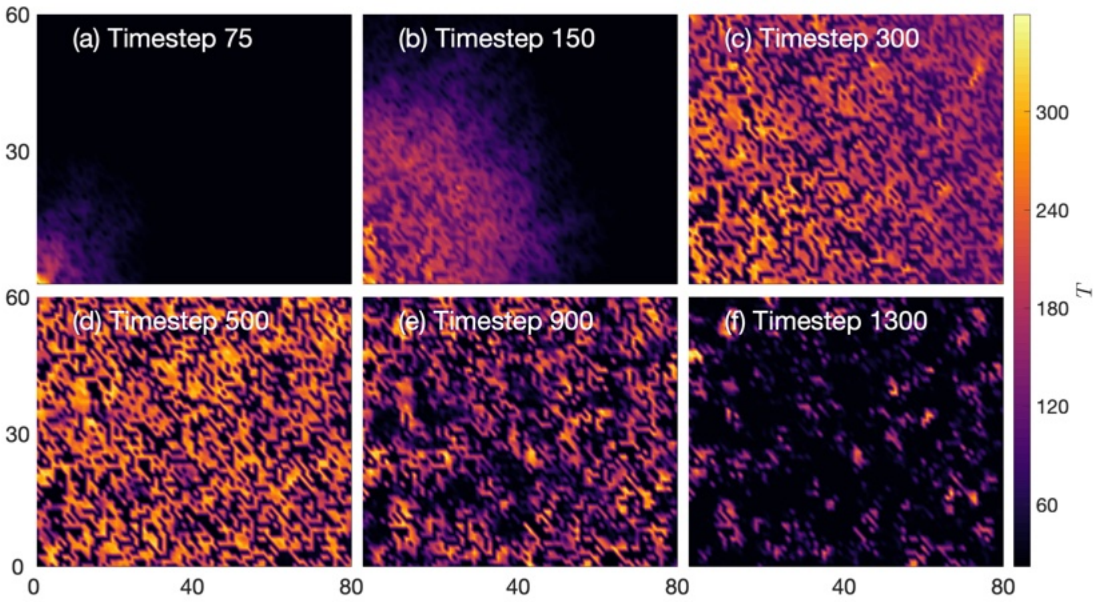

Figure 2.21: *Corner ignition: SERF Simulation 25; a) time step 75; b) time step 150; c) time step 300; d) time step 500; e) time step 900; f) time step 1300*

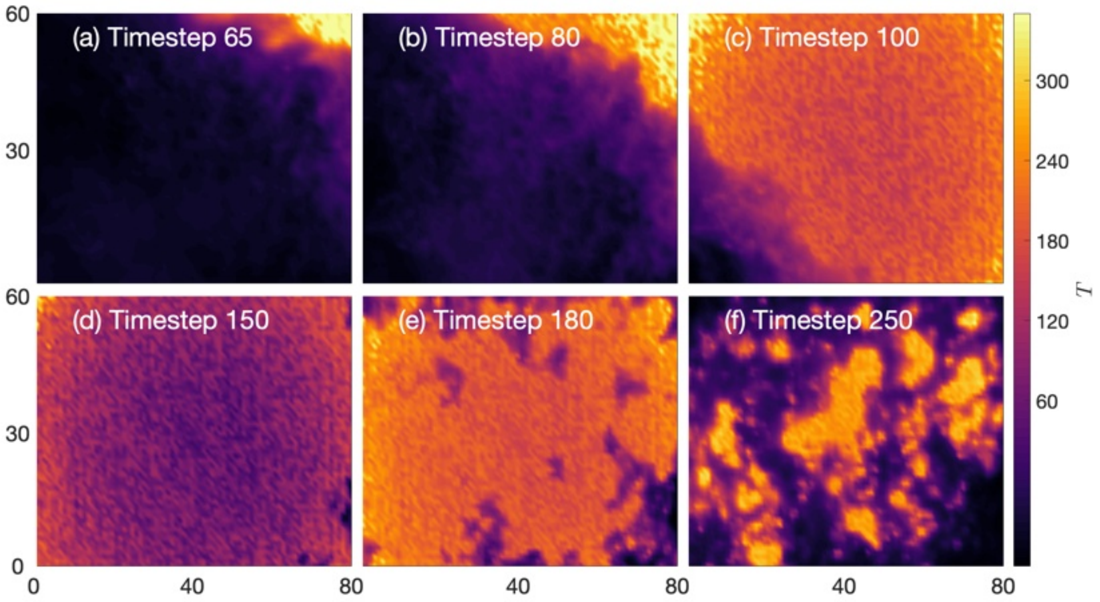

Figure 2.22: *Corner ignition: data set Fire 25; a) time step 65; b) time step 80; c) time step 100; d) time step 150; e) time step 180; f) time step 250*

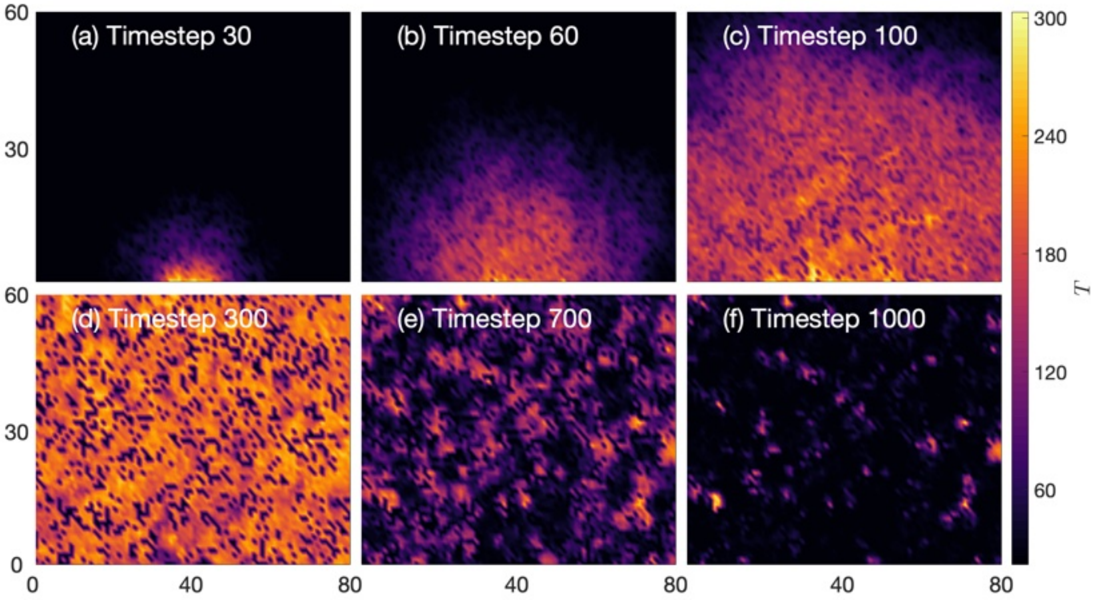

__Figure 2.23:__ Chunk ignition: SERF Simulation 45; a) time step 30; b) time step 70; c) time step 200; d) time step 300; e) time step 500; f) time step 700

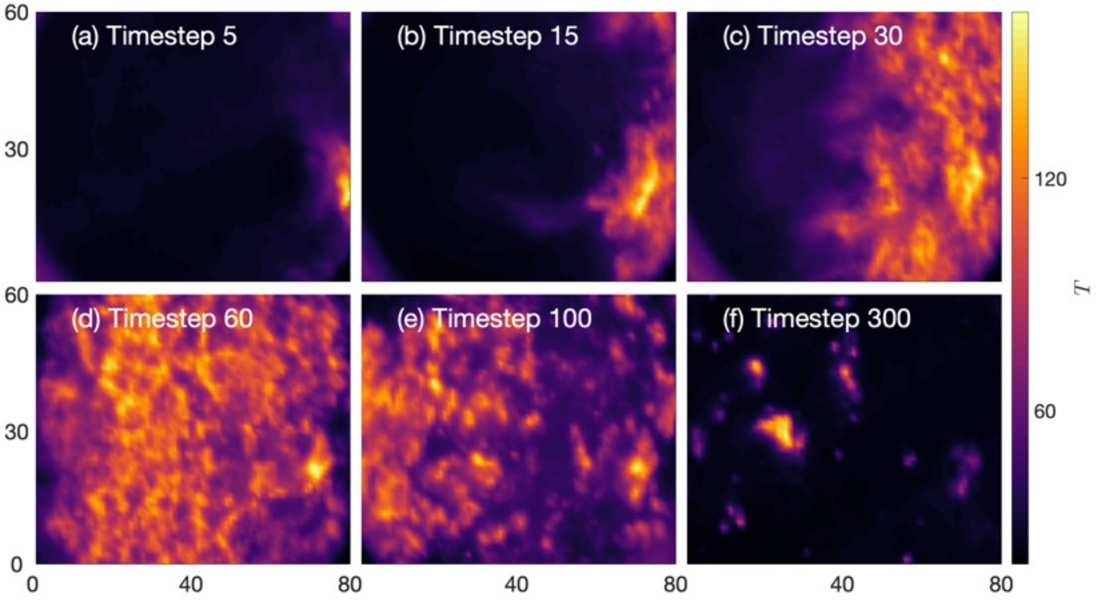

__Figure 2.24:__ Chunk ignition: data set Fire 145; a) time step 5; b) time step 15; c) time step 30; d) time step 60; e) time step 100; f) time step 300

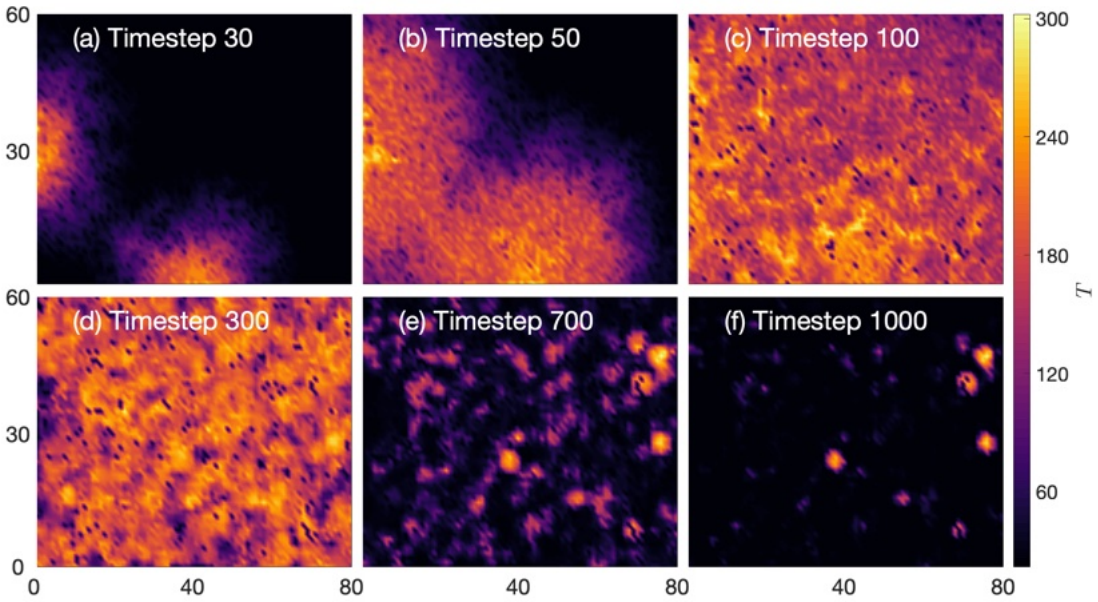

Figure 2.25: *Double Chunk ignition: SERF Simulation 90; a) time step 30; b) time step 50; c) time step 90; d) time step 200; e) time step 500; f) time step 800*

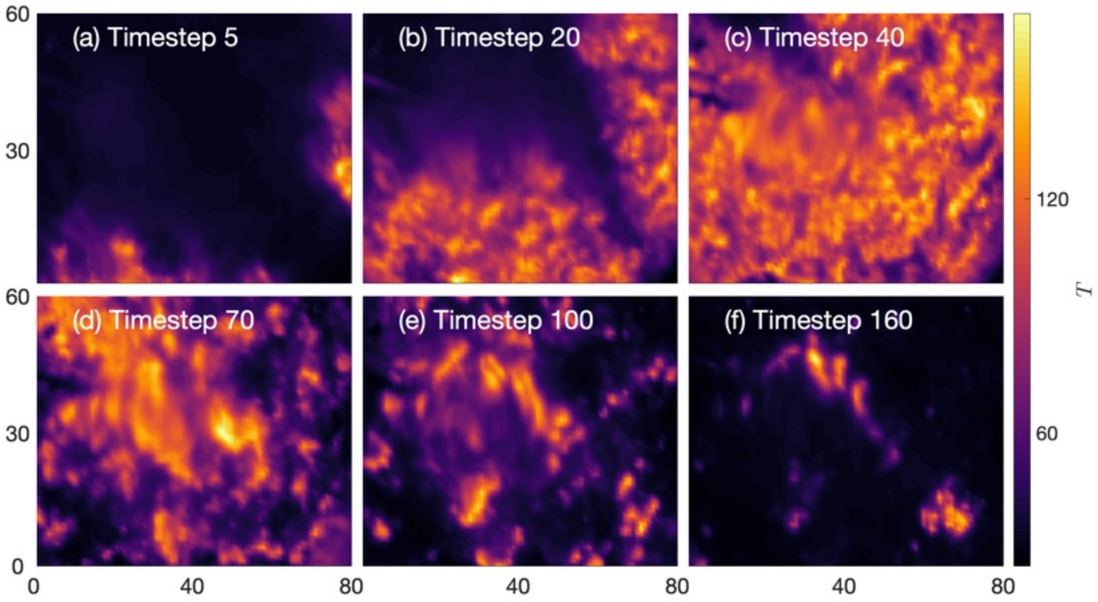

Figure 2.26: *Double Chunk ignition: data set Fire 3; a) time step 5; b) time step 20; c) time step 40; d) time step 70; e) time step 100; f) time step 160*

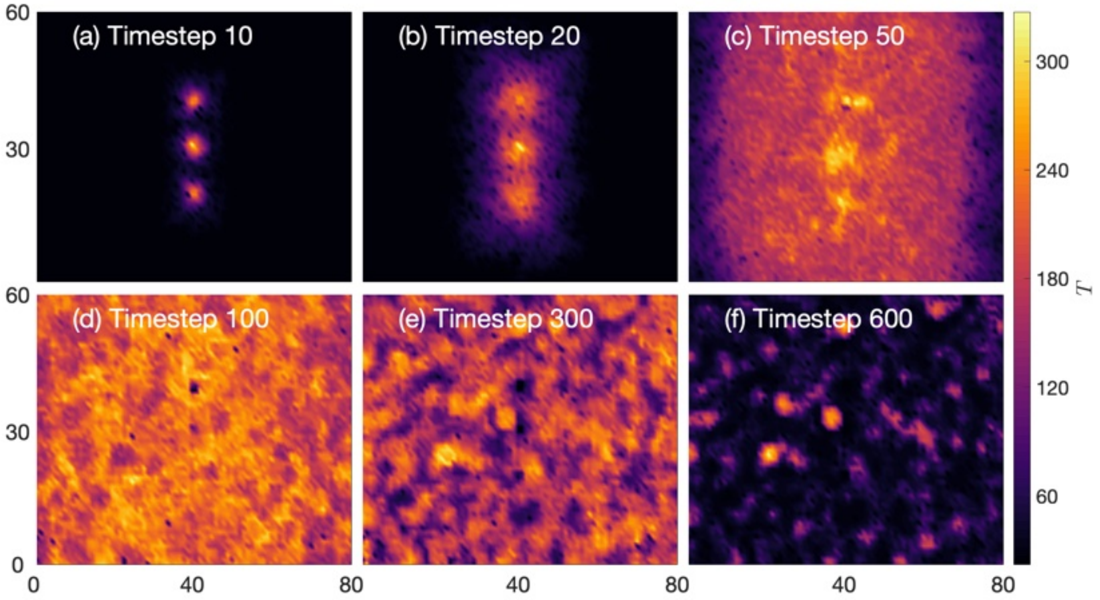

Figure 2.27: *Spotting ignition: SERF Simulation 63; a) time step 10; b) time step 20; c) time step 50; d) time step 100; e) time step 300; f) time step 600*

CHAPTER 3. DUET: Distribution of Understory using Elliptical Transport

The material presented below is part of the article published in *Ecological Modelling* (McDanold et al. 2023).

3.1 Basic description

Here we describe a mechanistic model called the Distribution of Understory using Elliptical Transport (DUET), using a frequently burned longleaf pine woodland in the southeastern U.S. as a case study. Two tree species with very different canopy and leaf shapes (pine needles vs. broad leaves) are used to test the model. DUET uses simplified fall trajectories to determine leaf litter and grass spatial patterns from a given overstory structure with specified wind conditions. For brevity, we define leaf litter as only dead leaves and needles. We propose a methodology to model leaf and needle shedding from trees, accumulation on the surface, decay and compaction over time, and the effects of litter buildup on grass growth. The model uses elliptical dispersal regions to represent the area covered by litter as a function of winds and aerodynamic characteristics of falling foliage, based on surface area and drag coefficients approximated from the average size and shape of an individual leaf. We verified the methodology by testing changes in tree height, size and shape of an average leaf, drag coefficients, and wind variance.

3.2 Model design

DUET accesses canopy structure data stored in three-dimensional voxelated density arrays and produces a discretized spatially explicit array of litter deposited on the ground resolved at meter scales. The deposition region from a voxel within the tree canopy is an elliptical area defined by gravity, local wind estimates, and aerodynamic drag of the foliage that is falling. Models are then used to account for litter decay and compression effects according to each species' characteristics, and grass growth is predicted based on tree shade and litter cover patterns.

3.2.1 Foliage trajectory and deposition

DUET uses species-dependent foliage bulk density for each canopy location in an explicitly resolved forest, woodland, or shrub layer within the domain of interest as input. Bulk density values are provided in a three-dimensional voxelated array. Such arrays can be developed from field measured or remotely sensed data (Linn et al. 2005; Pimont et al. 2016; Parsons et al. 2018). Voxel size depends on the application, but for the purposes of this work, we choose voxel resolution of 1 or 2 meters, depending on the simulation.

We assume that in the absence of wind, the foliage from each voxel falls predominantly downward with some oscillating lateral movement due to its unstable aerodynamics. This lateral movement during the fall creates a cone of flight paths from each canopy location that intersect the ground within a circle of radius, r_{ground}measured in meters. If the ground is flat, r_{ground} represents a minimally sized circular deposition footprint since any other trajectory induced by the presence of wind will be a longer distance with more dispersed patterns. This is not strictly true for sloped ground, which will be addressed in future work.

The radius of the resulting deposition pattern is dependent on the time (in seconds) the leaf requires to fall, t_{fall}, and the lateral distance the leaf could travel during that time, assuming minimal wind activity. We assume that the leaf reaches terminal vertical velocity quickly and therefore t_{fall} is defined using the height off the ground, H_C, divided by the terminal velocity, $v_{terminal}$; $v_{terminal}$ is dependent on the average mass and surface area for a leaf or needle for each species, m_{fol} and A_{fol}, the air density for the area, ρ_{air}, the acceleration due to gravity, g, and a predefined drag coefficient for the leaves or needles, C_d, either from literature or species-specific measurements, if available (Eq. 3.1 and 3.2).

$$t_{fall} = \frac{H_C}{v_{terminal}} \tag{3.1}$$

$$v_{terminal} = \sqrt{\frac{2m_{fol}g}{\rho_{air}A_{fol}C_d}} \tag{3.2}$$

To calculate r_{ground}, we define the effective radius of the voxel of horizontal dimension $dx \times dy$ to be the radius of the deposition circle if the foliage was located just above the ground when it fell, $r_{min} = \sqrt{dxdy/\pi}$. We then add to this minimum radius a distance contributed by oscillating lateral movement, r_{osc}, of the foliage as it falls from some height > 0:

$$r_{ground} = r_{min} + r_{osc} \tag{3.3}$$

We define $r_{osc} = L_H n_{steps}$, where L_H is found by the Cauchy momentum equation in Lagrangian form. This equation was developed to represent linear transport of a unit of material subjected to the forces acting on the unit as it travels through a given slow-moving fluid. We use this to represent the maximum horizontal distance that the leaf or needle can reach within each oscillation step it takes through the air during its descent. In the model, L_H is calculated by dividing a characteristic length proportional to $\sqrt{A_{fol}}$, where A_{fol} is the surface area of the leaf or needle, by the Froude number, Fr, which represents a measurement of buoyancy. To compute the Froude number, we assume minimal oscillation velocity $|u_0| = 0.01$. n_{steps} is the maximum number of steps the leaf or needle can take in the time within which it is falling, t_{fall}. We estimate that oscillation frequency of the falling foliage is N steps per second. Definition of this parameter and the proportion constant a could be refined in future work.

$$L_H = \frac{a\sqrt{A_{fol}}}{Fr} \quad Fr = \frac{|u_0|}{\sqrt{g\sqrt{A+_{fol}}}} \quad n_{steps} = \left\lceil t_{fall} \times \frac{Nsteps}{s} \right\rceil \tag{3.4}$$

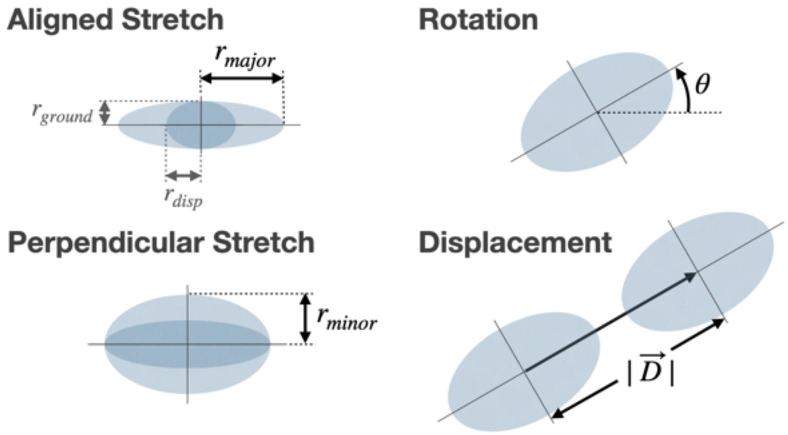

Figure 3.1: *Transformations from wind information for determining dispersal region of leaf or needle fallout; zonal wind stretch is defined using zonal standard deviation multiplied by fall time; meridional wind stretch is determined by meridional standard deviation multiplied by fall time; rotation and displacement are determined by the mean wind speed trajectory*

Given the circle defined by r_{ground} located at the center of the canopy voxel at coordinates (x_c, y_c) within the surface voxel, we now perform displacement, stretching, and rotation to this circle to find the dispersal area for the foliage (Fig. 3.1). These transformations deform the circle into an ellipse centered at (c_x, c_y) with radii r_{major} and r_{minor}, aligned along angle θ. To define these transformations, we use mean horizontal wind velocity components in the x and y directions, u and v, and their standard deviations, σ_u and σ_v. At the very least, this methodology requires estimates of wind velocities during the time when foliage is falling for each year since the last burn. If more information is available regarding the winds throughout the area, the model allows for the option to separate the year into equal sections (monthly, 4 seasons, 6-months, etc.), each with their own wind velocity components. This offers the opportunity to designate a particular time of year for each specific species to drop their foliage (as different species of trees might drop their foliage at different times of year) and implement related wind conditions for that time.

Using t_{fall}, the mean horizontal displacements in the x and y directions, D_x and D_y for the elliptical region can be computed by integrating the horizontal wind velocity over this time. For a discretized spatial and temporal system such as DUET, this collapses to $D_x = u_x t_{fall}$ and $D_y = u_y t_{fall}$, because of the terminal velocity approximation (gravitational force and drag force are equal) that translates to the foliage moving horizontally as the speed of the surrounding air.

We assume that the foliage rapidly reaches the horizontal velocity of the local wind in the i direction, U_i, based on its low inertia. With this assumption, the mean horizontal displacement, D_n, in the i direction is given by:

$$D_i = \int_0^h U_i(z) \frac{dz}{v_{terminal}} \tag{3.5}$$

For scenarios where the average ambient horizontal velocity over the height h is known, the formula collapses to:

$$D_i = \int_0^{t_{fall}} U_i dt = U_i t_{fall} \tag{3.6}$$

By adding components of displacement in the x and y directions, the net average horizontal movement of the foliage becomes $\vec{D} = D_x\vec{i} + D_y\vec{j}$ where $\vec{i}$ and $\vec{j}$ indicate the directions aligned with the x and y axes. The displaced center of the elliptical region for dispersal of the leaves or needles,

(c_x, c_y) can be computed as $c_x = x_c + D_x$ and $c_y = y_c + D_y$ where (x_c, y_c) is the center of the voxel distributing its leaves.

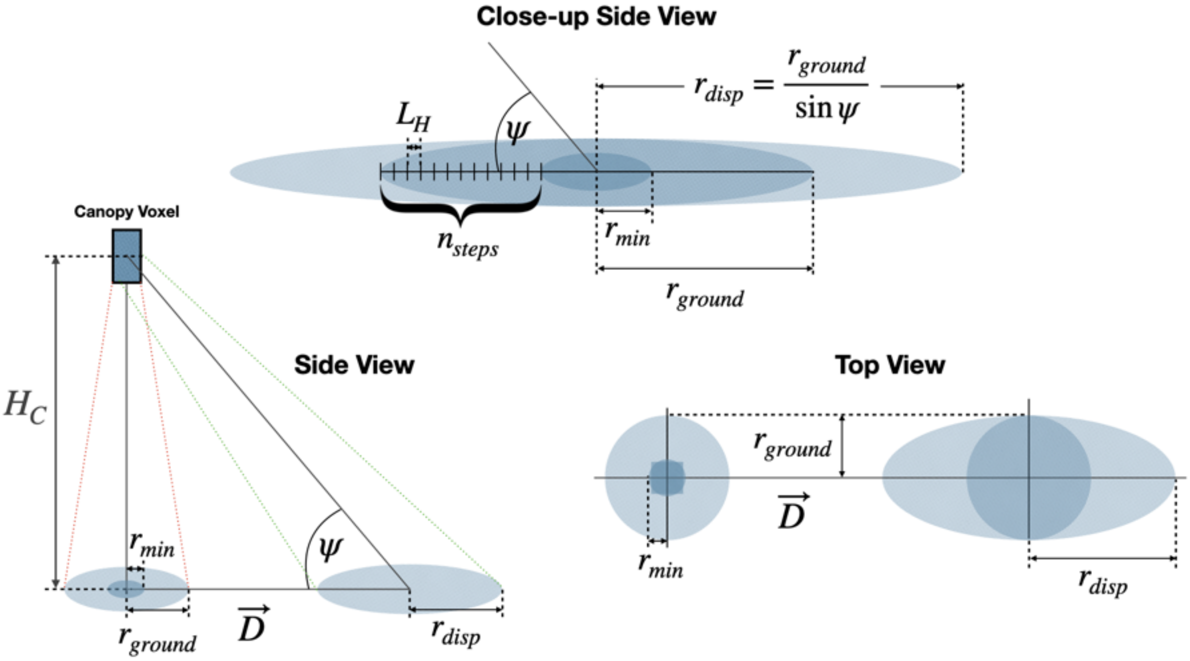

Figure 3.2: *Configuration for the change in major radius of the ellipse when center is displaced*

As the circle is displaced to a new location using u and v, the angle of incidence for the cone becomes an ellipse as shown in figure 3.2. The ellipse is now assumed to be aligned such that the major axis is directly in line with the displacement vector, $\vec{D}$. When the circular cross section with radius r_{ground} of the dispersion path takes on an angular trajectory onto the ground some non-zero horizontal distance from (x_c, y_c), the projected pattern on the ground is much more elliptical in nature. The projected ellipse is modeled with a minor axis that remains r_{ground} , and the major axis will be stretched into r_{disp} to account for the angle of incidence fall trajectory and the ground:

$$r_{disp} = \frac{r_{ground}}{\sin\phi} = r_{ground}\frac{\sqrt{H_C^2 + |\vec{D}|^2}}{H_C} \tag{3.7}$$

which equals r_{ground} for $\vec{D} = 0$.

For the two stretches, the standard deviation of the winds directly affects the breadth of the dispersal region. For instance, for high standard deviations in wind direction, the ellipse will be stretched into a broader area than for low standard deviation. This is to account for areas in which vast changes in wind directions occur rapidly during the time when the leaves are falling.

The standard deviations of the horizontal wind speeds, σ_u and σ_v, influence the aligned and perpendicular stretches of this displaced ellipse when multiplied by the time for the leaves to fall, t_{fall}:

$$r_{major} = r_{disp} + t_{fall}\sigma_u \qquad r_{minor} = r_{ground} + t_{fall}\sigma_v \tag{3.8}$$

The rotation of the ellipse is then determined by calculating the angle between u and v to align it with the displacement vector, $\vec{D}$ (Figure 3.1). Note that the stretches are mathematically calculated before the rotation of the ellipse. Once the rotation occurs, the stretches are affected by the rotation and are adjusted. In this way, the major and minor axes of the ellipse are affected by both directional wind vectors once the rotation has been applied.

In matrix notation, we can use projective coordinates to illustrate the process by which each of the original points within the unit circle move to their new coordinates in the transformed space. In equation 3.9 the first matrix on the left represents the displacement, the second the rotation, and the third the aligned and perpendicular stretches:

$$\forall (x,y) \in x^2 + y^2 \leq 1 :$$

$$\begin{bmatrix} 1 & 0 & D_x \\ 0 & 1 & D_y \\ 0 & 0 & 1 \end{bmatrix} \begin{bmatrix} \cos\theta & -\sin\theta & 0 \\ \sin\theta & \cos\theta & 0 \\ 0 & 0 & 1 \end{bmatrix} \begin{bmatrix} r_{major} & 0 & 0 \\ 0 & r_{minor} & 0 \\ 0 & 0 & 1 \end{bmatrix} \begin{bmatrix} x \\ y \\ 1 \end{bmatrix} = \begin{bmatrix} E_x \\ E_y \\ 1 \end{bmatrix} \tag{3.9}$$

This series of matrices can be expressed as $A\vec{x} = \vec{E}$ where $\vec{x}$ is any coordinate within the unit circle, $\vec{E}$ is the corresponding coordinate within the transformed elliptical space, and

$$A = \begin{bmatrix} r_{major}\cos\theta & -r_{minor}\sin\theta & D_x \\ r_{minor}\sin\theta & r_{minor}\cos\theta & D_y \\ 0 & 0 & 1 \end{bmatrix} \tag{3.10}$$

To find each point on the edge of the elliiptical region, we use

$$\vec{x} \in \left\{ \begin{bmatrix} x \\ y \\ 1 \end{bmatrix} \text{ s. th. } \begin{bmatrix} x \\ y \\ 1 \end{bmatrix} = \begin{bmatrix} \cos\phi \\ \sin\phi \\ 1 \end{bmatrix} \forall\ 0 \leq \phi \leq 2\pi \right\} \tag{3.11}$$

and we find the equations for the edge of the rotated and displaced ellipse:

$$\forall\ 0 \leq \phi \leq 2\pi :$$

$$\begin{bmatrix} E_x(\phi) \\ E_y(\phi) \end{bmatrix} = \begin{bmatrix} |r_{major}|\cos\phi\cos\theta - |r_{minor}|\sin\phi\sin\theta + D_x \\ |r_{minor}|\sin\phi\cos\theta + |r_{major}|\cos\phi\sin\theta + D_y \end{bmatrix} \tag{3.12}$$

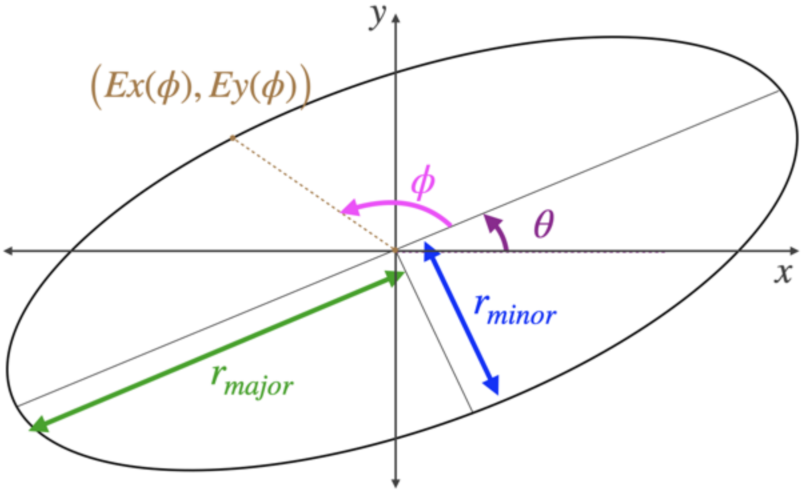

Figure 3.3: Rotated elliptical region for litter dispersal with θ = the rotation of the ellipse, ϕ defined as all radians between 0 and 2π, E_x and E_y as the displaced coordinates at the specific angle ϕ, and the radii defined using the wind information in equation 3.8

Figure 3.3 shows the rotated ellipse and the locations of the angles and measurements for these equations.

3.2.2 Mass dispersal within the elliptical region

Once the elliptical region is defined, DUET disperses a portion of the mass for each species from a canopy voxel to a particular location in the elliptical region. Each species drops a fraction of the mass within the voxel that is shed per year, ξ_{drop} or per time period during the year when foliage is shed, t_{drop}. ξ_{drop} is calculated using the inverse of the number of years a species requires to shed its entire canopy, a_{drop}; e.g., longleaf pine (*Pinus palustris*) needles are retained for two years (Stowe 2019). We chose to use a_{drop}=2 which makes ξ_{drop}=1/2.

As foliage falls along a mean trajectory, we assume that the distribution of the foliage within the deposition region is at its maximum at the center. Since the ellipse defines the outer limit of the potential deviation from the mean fall trajectory the foliage may achieve during its descent, we assume that the deposition load declines linearly from the center to any location on the perimeter of the deposition region. This means that the distribution of the foliage takes on a conical shape, so that the peak of the cone is located at the center of the ellipse, where the mean trajectory intersects the ground, and the distribution reaches zero at the perimeter of the elliptical fall pattern. In the absence of wind, as the dispersal region is circular, this process creates a circular cone distribution; in the presence of a wind field, the cone takes on the elliptical base for surface deposition.

Since the integrated mass over the elliptical area is ξ_{drop} times the mass within the source canopy cell, m_c, we can solve for the maximum mass of the conical distribution, m_{max}, which occurs at the center point of the ellipse, (c_x, c_y). We use the equation for the volume of a cone using the elliptical radii, r_{major} and r_{minor}:

$$\xi_{drop} m_c = \frac{1}{3}\pi r_{major} r_{minor} m_{max} \quad \rightarrow \quad m_{max} = \frac{3\xi_{drop} m_c}{\pi r_{major} r_{minor}} \tag{3.13}$$

Once the maximum of the conical distribution is known, the deposited mass of the litter at any given point within the elliptical region can be calculated using a linear function with m_{max} as the y-intercept. See section 3.2.5 for the numerical calculation of the mass dispersal.

For each year since the region was last burned, the elliptical deposition region is identified for foliage falling from all canopy voxels with foliage in them, and the resulting mass depositions are accumulated in appropriate ground-level voxels. This produces a layering effect with each layer tracked separately, representing the litter fall per year within the simulation where total litter load is the sum of the layers in one voxel.

3.2.3 Litter decay

Decay is an important process controlling litter mass. Olson (1963) illustrates well how variables decay among ecosystems. We postulate that the loss of litter mass accumulated in year, $m_{litter,year}$, with a decay rate for species S, $D_{S,year}$, can be written:

$$\frac{\partial m_{litter,year}}{\partial t} = -D_{S,year} m_{litter,year} \tag{3.14}$$

For mass accumulated in a single year, this becomes

$$m_{litter,year} = \left(1 - \exp -D_{S,year}\right) m_{litter,year-1} \tag{3.15}$$

Litter is dispersed per year with various wind conditions, which results in heterogeneous spatial deposition each year. We can imagine this as laying down variably thick litter layers across the forest floor, a layer for each year (or potentially season, depending on the species and location). As annual layers build up in different areas, the decay rate for each of these layers is affected by the number and thickness of layers that have accumulated above it (older layers are likely to have more mass above them). Thus, $D_{S,year}$ might be greater due to moisture retention and compaction when greater mass of litter is stacked above a specific year's layer by litter falling in more recent years (Stephens, Finney, and Schantz 2004; Mueller et al. 2021).

For this proof-of-concept demonstration, we approximate the annual decay of *year* layer, $D_{S,year}$, with the most recent year of deposition defined as Y_r, with the linear function:

$$D_{S,year} = \sum_{j=year+1}^{y_r} CP_s m_{litter,j} \tag{3.16}$$

where CP_s is a species- and area-specific compaction rate, and $m_{litter,j}$ is the mass of the litter deposited in this area during year j. Then we have:

$$\frac{\partial m_{litter,year}}{\partial t} = -\left[\sum_{j=year+1}^{y_r} CP_s m_{litter,j}\right] m_{litter,year} \tag{3.17}$$

$$\frac{\partial mass_{accum}}{\partial t} = \frac{\partial \sum_{j=1}^{y_r} m_{litter,j}}{\partial t} = -\sum_{j=1}^{y_r}\left[\sum_{k=j+1}^{y_r} CP_s m_{litter,k}\right] m_{litter,j} + m_{litter,y_r} \tag{3.18}$$

There are two long-term effects that result from this increasing decay rate with increasing depth: 1) the rate of change of the litter mass with time since last burn decreases with time and can stop changing when

$$\sum_{j=1}^{y_r}\left[\sum_{k=j+1}^{y_r} CP_s m_{litter,k}\right] m_{litter,j} = m_{litter,y_r} \tag{3.19}$$

and 2) over many years there is an homogenization of litter loads over time as locations where large amounts of litter falls also eventually gain higher decay rates (Stephens, Finney, and Schantz 2004).

3.2.4 Grass production

Grass production is affected by light availability, belowground competition, and inhibition from accumulated tree litter (Hiers et al. 2007; Pecot et al. 2007; Montgomery, Reich, and Palik 2010). The amount of grass is influenced by a litter cover factor, λ_l (Eq. 3.20), determined by the amount of litter covering the ground in a particular voxel, along with a shade factor, λ_s (eq. 3.21), determined by the voxel with the maximum density located above the voxel (x,y). Each of these factors are divided by $\rho_{max,species}$, the maximum density of a given species that can exist within a particular voxel.

$$\lambda_l = \frac{\min \rho_{litter}, \rho_{max,species}}{\rho_{max,species}} \tag{3.20}$$

$$\lambda_s = \frac{\max_z \rho_{species,x,y}(z)}{\rho_{max,species}} \tag{3.21}$$

Once these factors are determined, grass growth is calculated by taking a fraction of the maximum annual grass growth for the area, $grass_{ann,max}$ in mass/year:

$$grass_{x,y} = \exp - (g_l \lambda_l + g_s \lambda_s) \tag{3.22}$$

For maximum litter and shade cover, $\lambda_l = \lambda_s = 1$ and eq. 3.22 simplifies to $\exp - (g_l + g_s)$, where g_l and g_s represent the maximum inhibition of grass growth within the given area for litter cover or shade, respectively. Note that if ρ_{litter} and $\max_z \rho_{species,x,y}(z)$ are equal to 0, we have $\exp -0 = 1$, and there is no reduction in grass growth.

For circumstances in which only the average value of grass growth is known, we normalize these values by finding the average value for the grass across the entire domain using the sum of all of the grass values for every voxel, $grass_{x,y}$, and dividing by the number of cells in the domain, $H_x H_y$, with H_x = total voxels in the domain in the x direction, and H_y = total voxels in the domain in the y direction:

$$grass_{x,y} = \frac{\sum_{x,y} grass_{x,y}}{H_x H_y} \tag{3.23}$$

3.2.5 Numerical implementation

DUET has been designed to create numerical simulations of litter and grass for a designated virtual environment. The inputs for the system include a canopy voxel array and information regarding species and stems per hectare for the area to be simulated. The outputs for the system were designed to be usable by various existing fire or ecosystem models.

Model Inputs

DUET simulations begin the year of the last burn, in which the previously existing grass and litter have been consumed, leaving no grass or litter on the ground. This can potentially be adjusted for existing grass and litter in future work. The provided density array for the shrub or canopy fuels that exist in the area, ρ_f, must be four-dimensional with three spatial dimensions per species (fourth index is species), assuming no litter or grass. The first layer of this array may contain shrub or canopy fuel, however, as some species stretch into the ground-level voxels (depending on height to foliage on plants and vertical extent of the first cell).

A list of species-specific characteristics, and a list of wind values must also be provided. The species-specific values required include the maximum density of a species, $\rho_{max,species}$, average crown bulk density within the tree, ρ_{avg}, an average mass for a single leaf or needle, m_{fol}, an average surface area for a single leaf or needle, A_{fol}, a drag coefficient for the leaf or needle, C_D, a compaction rate, CP_s, a moisture level for the live leaf, M_s, and a timestep during which the leaves will be dropping from the tree, t_{drop}. For instance, the drag coefficient, C_D, can be approximated based on the shape of the leaf: a pine needle resembles a thin cylinder which could be approximately, $C_D = 0.6$, whereas a broadleaf resembles a piece of paper, which could be approximately $C_D = 2.43$.

Wind information must be provided for the area per time step. Although typically we use year-length time steps, the model can also use shorter time steps to account for the various times during the year that a particular species will lose its canopy. The wind file must list the year,

year, the step during the year, $year_t$, and the corresponding average wind speeds in the x and y directions at canopy height, u and v, along with their standard deviations, σ_u and σ_v. These can be directly measured for the area, or obtained from gridded meteorological datasets based either on observations [e.g. Livneh, (Livneh et al. 2013) or the Gridded surface Meteorological dataset (Gridmet) (Abatzoglou 2013)], downscaled climate model simulations [e.g. Multivariate Adaptive Constructed Analogs Comparison Project Phase 5 (MACA CMIP5) (Abatzoglou and Brown 2012)], or fine-scale atmospheric simulations [e.g. HIGRAD (Dupuy et al. 2011; Koo et al. 2012)]. If a fine-scale atmospheric model is used, the wind field presents as u and v values for each voxel in the domain array based on the vegetation structure itself, and DUET will calculate the $u, v, \sigma_u, and \sigma_v$ values for the vertical column corresponding to the canopy voxel dropping its leaves.

Numerical density calculations

Once the deposition distribution pattern for foliage originating from a particular canopy voxel and species has been defined by the equations in the previous sections, the mass of the foliage is added to the appropriate ground-level voxel. The mass contribution from each canopy or shrub voxel that contains m_c foliage bulk density to each of these ground voxels, $m_{x,y}$ is calculated using a weighting system based on the conical distribution model discussed above:

$$m_{x,y} = \frac{l_n(x,y)}{\sum_{n=1}^{E_n} l_n(x,y)} \xi_{drop} m_c \tag{3.24}$$

where l_n is the relative height of the cone distribution pattern within voxel (x,y), and E_n is the total number of surface voxels contained within the entire elliptical deposition region associated with this source canopy voxel. $l_n(x,y)$ is defined as:

$$l_n(x,y) = 1 - \frac{\sqrt{(c_x - x)^2 + (c_y - y)^2}}{\sqrt{(c_x - E_x)^2 + (c_y - E_y)^2}} \tag{3.25}$$

with (c_x, c_y) as the coordinate of the center of the ellipse and (E_x, E_y) as the corresponding coordinate for the edge of the ellipse such that there exists a straight line that passes through (c_x, c_y), (x, y), and (E_x, E_y). See the complete description for how (E_x, E_y) is calculated in section 3.2.1.

To illustrate how the numerical model applies the conical distribution for a given ellipse, Fig. 3.4 shows the predicted litter bulk density at each of the surface voxels within the defined elliptical region from a single canopy voxel located $20m$ high with wind values of $u = 9m/s$, $v = -9m/s$, $\sigma_u = 5m/s$, and $\sigma_v = 12m/s$:

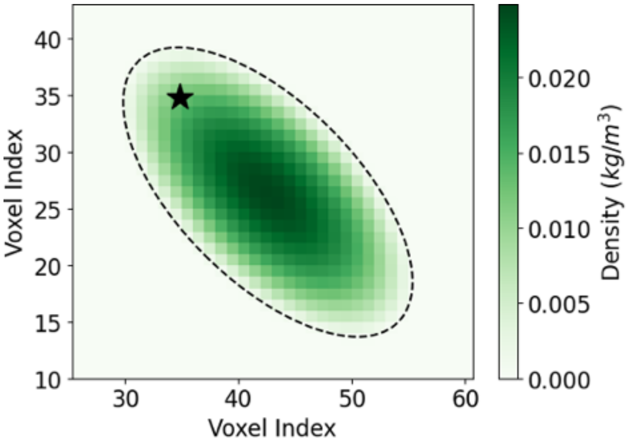

Figure 3.4: *Voxelated density array produced by the program for use within HIGRAD/FIRETEC fire behavior simulations; the star is the location of a canopy voxel with coordinates* $(35, 35, 10)$ *and wind values of* $u = 9$, $v = -9$, $\sigma_u = 5$, *and* $\sigma_v = 12m/s$

3.3 Results

3.3.1 Simulation setup

Tree maps

We consider four synthetic forests to examine the effects on litter dispersal of several species and environmental characteristics including the impact of tree height, drag coefficients, wind influence, average leaf surface area, and decay factors. To show the impact of tree height, we developed two maps with generalized species characteristics (a conifer species and a broadleaf species), each with a single small tree and a single large tree. Table 3.1 reports the specific measurements used in these short versus tall simulations. Note that the drag coefficients, compaction rates, and drop rates are nondimensional parameters.

Table 3.1: *Species specific parameters for short versus tall tree simulations*

Tree Type	Height (m)	Height to max crown radius (m)	Canopy base height (m)	m_{fol} (g)	A_{fol} (cm^2)	Decay $(\%/yr)$	Drag Coeff	Compact	Drop per year
Short, Conifer	10	7	5.5	1	0.5	1	0.6	0.2	$1/2$
Tall, Conifer	20	14	11	1	0.5	1	0.6	0.2	$1/2$
Short, Broadleaf	10	0	0	2.04	168	0.5	2.43	0.2	1
Short, Conifer	20	0	0	2.04	168	0.5	2.43	0.2	1

These parameter values represent average relative relationships developed from a dataset collected at Eglin Air Force Base in Florida, described in further detail below.

Drag coefficients are used to distinguish fall trajectories for coniferous needles versus broadleaves. We use a drag coefficient of 2.43 for the broadleaf described above, a relatively flat leaf that will have more oscillations due to the larger surface area than the conifer. For a coniferous needle, which has less surface area and therefore will oscillate less as it falls through the air, we use a drag coefficient of 0.6. A map using two identical trees at $10m$ tall, $5m$ height to maximum crown radius, and $0m$ canopy base height with drag coefficients 0.6 and 2.43 compares drag coefficient effects.

We also test the model in a domain populated using tree measurements collected at Eglin Air Force Base in Florida in 2008, a xeric longleaf pine sand-hill forest and grass area with a subtropical climate (Ottmar et al. 2015). The recorded tree locations span an area of approximately $67m \times 106m$. The terrain in this area was without slope at that scale. We used this tree dataset to populate a $400m \times 400m$ domain at $2m$ lateral resolution using random sampling of the original dataset while preserving measured stem density for a total of 2163 trees in the domain. This dataset included two species of trees: longleaf pine (*Pinus palistrus*) and turkey oak (*Quercis laevis*). We used this tree map to test various decay factors and wind field effects.

Wind conditions

To test the effect of winds on the litter deposition, several of the simulations used extreme wind conditions. Using the standard deviation of the winds as a metric for variability, we evaluated four idealized wind scenarios, including (1) a "no wind, no standard deviation" (NWNS) scenario where the litter deposition is solely reliant on height from the tree and atmospheric drag, and represents the circle with radius r_{ground}; (2) a "high wind, no standard deviation" (HWNS) scenario with strong winds of $15m/s$ coming directly from the southwest with no standard deviation in trajectory,

(3) a “no wind, high standard deviation” (NWHS) scenario where wind speeds average spatially to $0m/s$, but standard deviation is high at $8m/s$ in all directions, and (4) a “high wind, high standard deviation” (HWHS) scenario with high average wind speeds ($15m/s$), and high standard deviation ($8m/s$) in all directions.

Then, we examined litter deposition using a more realistic wind profile to incorporate wind gusts that likely cause the leaves to fall from the tree. For this purpose, we first spun up a wind field in HIGRAD using the same Eglin tree plot with a starting wind speed of $13.4112m/s$ at a height of $34m$, which is approximately $10m$ above the highest tree in the dataset. We used cyclic boundary conditions as described in Pimont et al. (2016). After allowing the wind to find a relatively steady state over 600 seconds, we then recorded and averaged the mean wind values and variances in each voxel over all time steps to find the average wind speeds and the standard deviation at any given voxel within the three-dimensional domain. We applied DUET using wind information averaged over all voxels from the ground up to the height of the given canopy voxel, H_C. The values for the wind scenarios ranged as:

$$1.1872m/s \leq u \leq 13.8865m/s \tag{3.26}$$

$$-1.04651m/s \leq v \leq 0.9614m/s \tag{3.27}$$

$$0.0m/s \leq \sigma_u \leq 24.3431m/s \tag{3.28}$$

$$0.0m/s \leq \sigma_v \leq 7.4149m/s \tag{3.29}$$

within the areas that contained the canopy voxels. Tables 3.2 and 3.3 include a list of all the simulations performed to test the functionality of DUET.

3.3.2 Basic model functionality

Effects of tree height

To test the model's ability to distinguish litter dispersal from short versus tall trees, we used a small domain with 1-m resolution and two general tree types, conifer and broadleaf (CTH and BTH simulations described in Table 3.2). We applied species characteristics as defined in table 3.1, with wind descriptions as defined in section 3.3.1 and table 3.2. Figures 3.5 and 3.6 show the results of the tree height comparison.

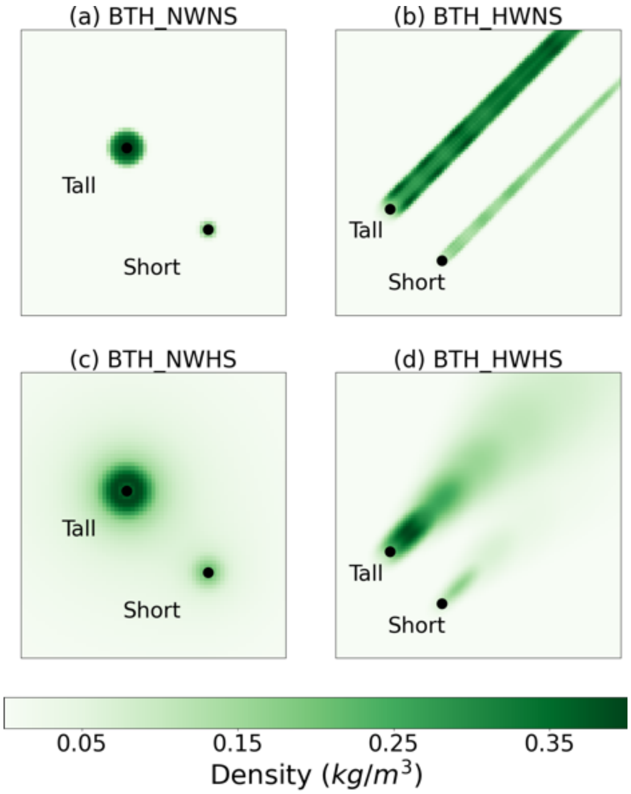

Figure 3.5: *Short versus tall broadleaf tree dispersal for four generalized wind events; a) no wind or standard deviation (NWNS), b) wind at* $15m/s$ *with no standard deviation (HWNS), c) no wind but* $8m/s$ *standard deviation (NWHS), and d)* $15m/s$ *winds with* $8m/s$ *standard deviation (HWHS); BTH = Broadleaf tree height; black dots are tree bole locations*

The broadleaf tree canopy represented here stretches down to the ground, while conifer trees have height to live crown distances of $5m$ and $10m$ for the short and tall trees, respectively. When no mean wind is present, litter accumulates primarily below and around trees. Taller trees result in a broader dispersal area (compare Figs. 3.5a , 3.5c, 3.6a, and 3.6c). With a positive mean wind, the dispersal area is stretched in the direction of the mean wind. For broadleaf trees, it begins closer to the base of the tree than for the conifer trees (compare figure 3.5b and 3.5d, and 3.6b and 3.6d). Figures 3.5c, 3.5d, 3.6c, and 3.6d also show that high wind standard deviations disperse the limited amount of litter from short trees leading to low litter bulk densities in any given voxel.

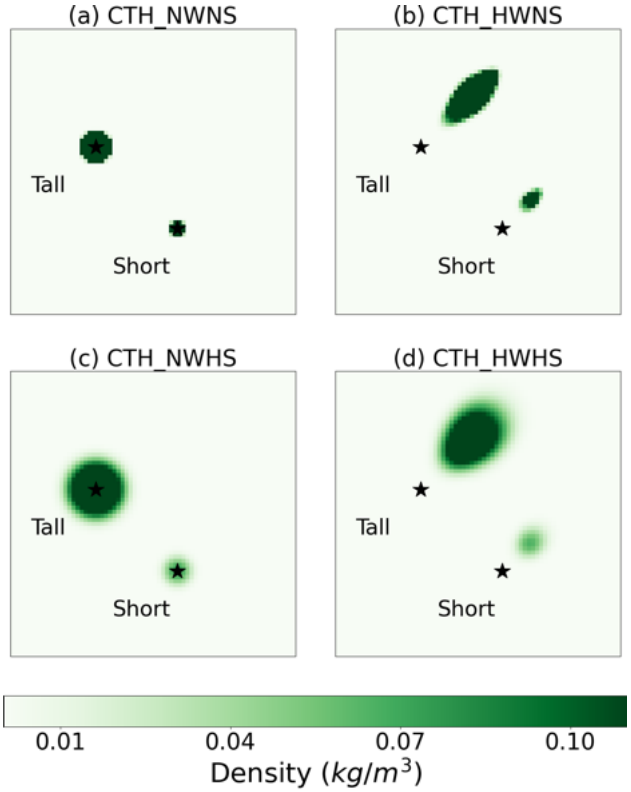

Figure 3.6: *Short versus tall conifer tree dispersal for four generalized wind events; a) no wind or standard deviation (NWNS), b) wind at* $15m/s$ *with no standard deviation (HWNS), c) no wind but* $8m/s$ *standard deviation (NWHS), and d)* $15m/s$ *winds with* $8m/s$ *standard deviation (HWHS); CTH = conifer tree height; black stars are tree bole locations*

Drag coefficient comparison

To demonstrate the influence of the drag coefficient on the litter dispersal region, we used a small domain with two trees, each of which were $10m$ tall, $5m$ maximum radius, $0m$ height to live crown, with drag coefficients 0.6 and 2.43. Figure 3.7 shows the results of the drag coefficient test.

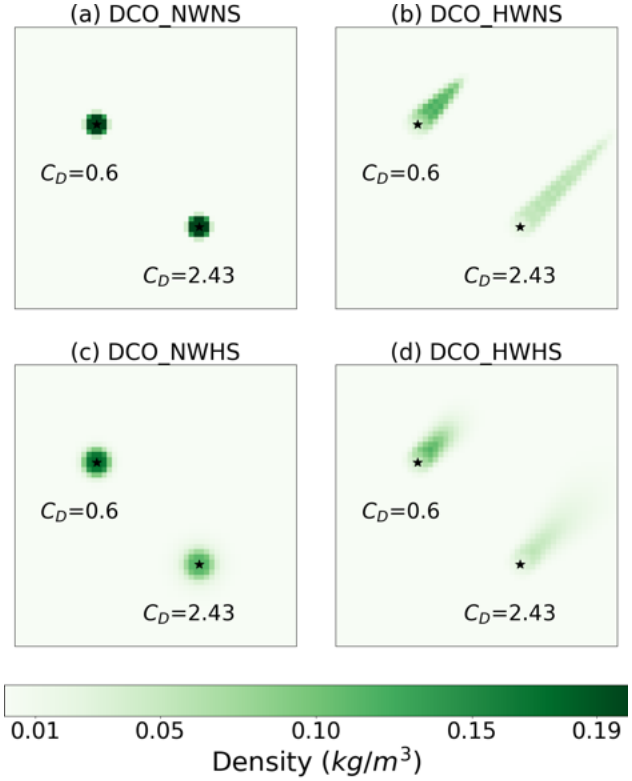

Figure 3.7: *Effect of the Drag Coefficient (DCO) on the dispersal region; all tree characteristics are identical except for the drag coefficient as labelled on the image where one drag coefficient is* 2.43 *which represents a flat leaf and the other is* 0.6 *which represents a needle falling; black stars are tree bole locations*

With the absence of wind influence, the drag coefficient does not affect the dispersal region, as shown in Fig. 3.7a. A larger drag coefficient expands the dispersal region due to the inverse relationship with terminal velocity, $v_{terminal}$ (Eq. 3.2). As $v_{terminal}$ increases, the time it takes for the foliage to fall (t_{fall}) increases, which in turn increases the maximum horizontal distance that the foliage can be transported and the greater dispersion that can occur, broadening the dispersal region. Figures 3.7b-d show these expansions clearly.

Decay factor comparison

To show the long-term effects of the decay factor on litter buildup, we ran three five-year simulations on a $400m \times 400m$ tree map using the two species described in table 3.1. The simulation tracks how the litter decays when deposited in the first of the five years with no other litter placed for the duration of the simulation (Fig. 3.8).

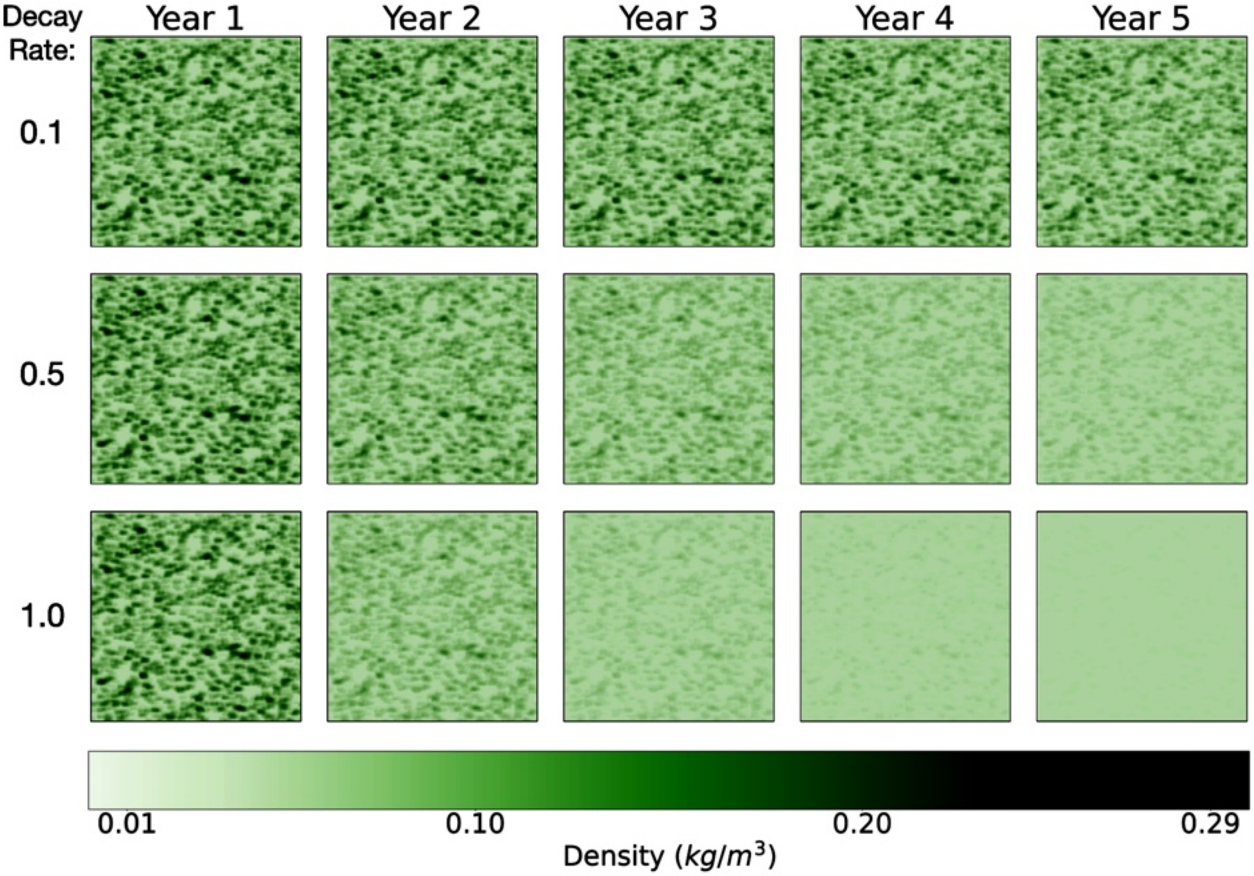

Figure 3.8: *Litter decay using (a) DECAY_1.0 = a decay rate of 1.0 in which there is a 63% loss of mass in one year, and (b) DECAY_0.1 = a decay rate of 0.1 in which there is a 63% loss of mass per 10 years, or approximately a 10% loss of mass per year*

To develop Fig. 3.8, we calculated the litter deposit for a single year with zero wind influence, and then applied the decay function with three different decay factors for 5 years without adding litter after the initial year. With a decay factor of 0.1, we lose $1-e^{-0.1} \approx 10\%$ of the mass each year; a decay factor of 0.5 results in a loss of $1-\exp^{-0.5} \approx 40\%$ mass per year; and a decay factor of 1.0 results in a loss of $1-\exp^{-1.0} \approx 63\%$ mass per year. In the figure, we begin with the same amount of litter dispersal for the first year, which is why the litter maps in the column for year 1 are identical.

Since the decay factor of 0.1 only results in 10% loss of mass per year, the mass on the ground remains for several years after the initial dispersal. In Fig. 3.8, the top row of year 5 is only slightly lighter than the top row of year 1, indicating only a slight loss of mass, or approximately $1-\exp^{-0.1(5)} \approx 40\%$ mass loss. In contrast, the decay factor of 1.0 results in a $1-\exp^{-1.0(5)}$ 99% loss of mass over five years, which can be seen in Fig. 3.8 in the bottom row on the right, which is almost completely devoid of litter.

3.3.3 Idealized forest area representation

Litter Buildup Under Randomized Wind Conditions

We performed simulations on a $400m$ by $400m$ domain with $2-m$ resolution to examine litter dispersion from trees of variable size and shape. We populated the domain with 2163 trees with heights ranging from $6.7m$ to $23.2m$, heights to live crown ranging from $0m$ to $17.7m$, and height to maximum crown radius ranging from $1.2m$ to $12.8m$. We chose random wind velocities that ranged as:

$$-8.998m/s \leq u \leq 5.308m/s \tag{3.30}$$

$$-8.805m/s \leq v \leq 7.433m/s \tag{3.31}$$

$$-7.871m/s \leq \sigma_u \leq 8.785m/s \tag{3.32}$$

$$-7.396m/s \leq \sigma_v \leq 7.330m/s \tag{3.33}$$

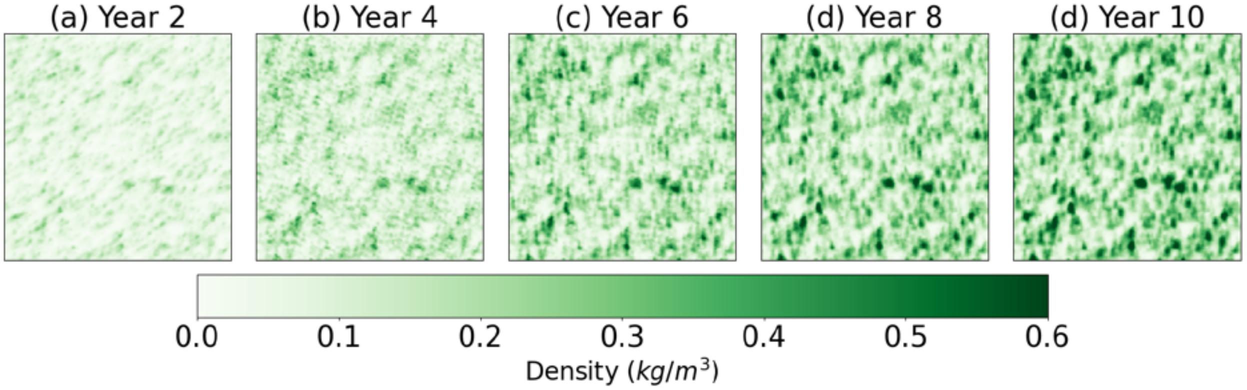

Figure 3.9: *Output for* 10 *years of litter deposition with random winds to show accumulation of surface litter over time*

Figure 3.9 shows the litter accumulation over ten years with overlapping ellipses. The layering effect for these elliptical dispersal regions is clearly shown in this figure. By year 10, there occurs a clear and direct connection with the canopy structure which is strengthened over time.

Litter deposition under gusty wind conditions

Because litter deposition from the canopy is sensitive to the variation in the wind fields, we next explored the influence of variation in winds through the large eddy simulation model HIGRAD, results of which are shown in Fig. 3.10.

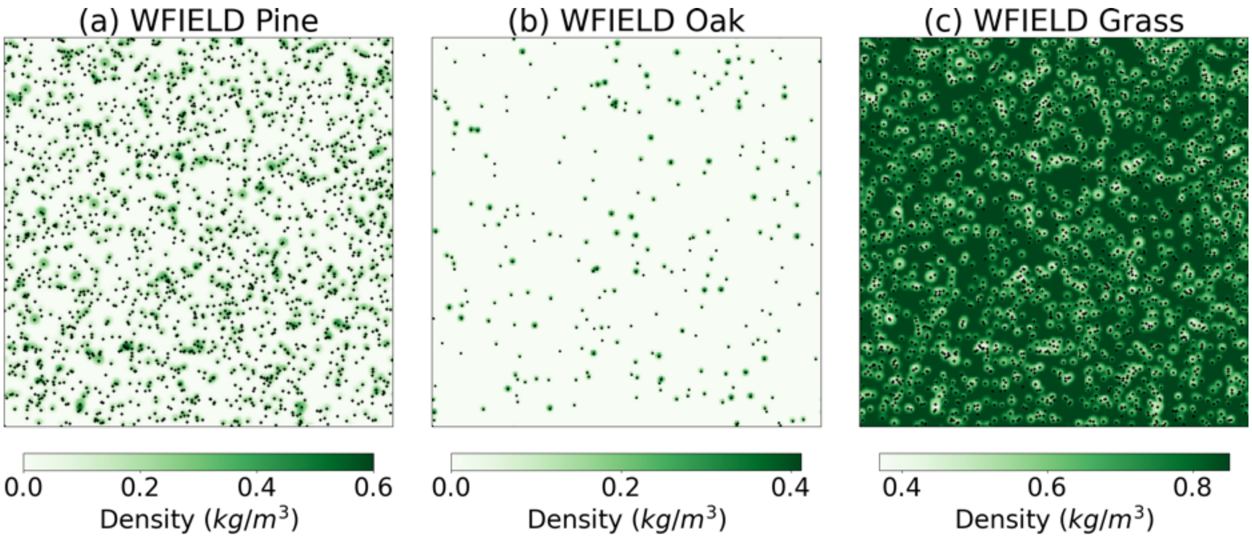

Figure 3.10: *WFIELD simulation; Litter deposition for (a) pine and (b) oak, and (c) grass biomass results from a DUET simulation using wind fields generated by HIGRAD, which captures wind gusts that cause the leaves to detach from the tree*

This more realistic wind field represents how we can account for the fully variable wind conditions for each spatial grid cell within the domain. Since the wind fields in these simulations are a function of the stand-scale drag, and include minimal wind speeds close to the ground, we can see that the dispersal regions are restricted closer to the tree locations. Within denser stands, the attenuation of mean windspeed dominates the distribution of litter, with occasional gusts distributing litter farther from originating voxels.

3.4 Discussion

The DUET model is capable of producing a heterogeneous surface litter and grass layer through a mechanistic representation of leaf litter and herbaceous spatial distribution based on tree canopy structure. Simulations explore critical phenomena that lead to the surface fuel deposition and growth patterns, and results agree with expected sensitivities to various canopy and wind parameters. However, there are processes that affect fuel distribution that are not yet included and continued efforts to validate the model are necessary.

3.4.1 Overstory Structure and composition

DUET produces modeled tree litter accumulation that is directly affected by overstory structure including the height and species-specific characteristics of the trees, in agreement with observations (Staelens et al. 2003; Nickmans et al. 2019). The model uses the height from which foliage is falling along with the average mass, surface area, and drag coefficient for the foliage (leaves or needles) to calculate the fall time for the foliage based on a terminal velocity approximation. In conjunction with the average wind speeds associated with the time period in which the foliage falls, this fall time helps to define the breadth of the dispersal pattern possible when falling needles or leaves reach the ground. The orientation of the wind-influenced fall path elongates the otherwise circular pattern into an elliptical region if the path is not straight down. Figures 3.5 and 3.6 in section 3.3.2 show effects of the height of the tree on the deposition region. Species foliage characteristics also influence the width of the deposition pattern. We compare oak leaves, which have a larger surface area and thus greater drag/mass, to pine needles. This slows down the fall speed of oak leaves relative to pine needles, increases the time aloft and allows for more lateral dispersion; therefore, the spread is generally broader for a given tree height (see Fig. 3.7). Since access to information on canopy structure is more readily available than understory structure, having a model that bases the understory on the canopy may provide the necessary precision for improving fire and ecosystem model inputs (Silva et al. 2016).

3.4.2 Wind influence

Wind events in the area directly affect when and how the litter falls from the tree (Staelens et al. 2003). In DUET, we use average wind speeds and standard deviations for the area to define the shape and size of the dispersal region. As wind is a main driver for mean horizontal movement of litter while it is falling, we use average wind speed to determine horizontal displacement as well as the orientation, and length of the ellipse in line with the horizontal trajectory. The standard deviation of wind speed affects how wide or narrow the ellipse becomes perpendicular to the displacement vector. We treat the influences of the wind standard deviations as having a diffusion type effect on the leaves or needles, resulting in a conical distribution of leaves when they land. While the majority of the leaves follow the mean path, the net pattern of foliage deposition from any single canopy source is a maximum at the center of the deposition pattern and the loadings fall off to zero linearly at the perimeter. While currently these wind trajectories are static inputs to the model, we hope to connect to a database in which we can implement recorded wind information for various time periods throughout the year and potentially expand DUET to include dynamic wind inputs. Figures 3.5, 3.6, 3.7, and 3.10 all show the effect wind conditions have on the elliptical regions and the heterogeneity of the result. In low wind conditions, the dispersal regions remain close to the tree boles, while high wind conditions result in wider spread. Future iterations of the model should incorporate a wind intensity vector that accounts for higher rates of litter drop during high wind events.

3.4.3 Decay Processes

Within DUET, decay processes affect how the bulk density, moisture level, and depth of litter changes over the years after deposition, as well as the inhibition of grass growth. With the layering effect created over years of litter accumulation, the decay processes are affected both by species-specific decay factors and depth of litter on top. Figure 3.8 shows three different decay factors and the resulting effect on the litter accumulation through the years after they fall. When a smaller decay factor is applied, the litter does not decay and reduce as much as a higher decay factor. When coupled with the layering effect shown in Fig. 3.9, the decay factor has a high influence on the spatial heterogeneity of litter on the ground over years.

3.4.4 Model Assumptions

As with any mathematical model, several assumptions were made within the design of DUET. First, we assumed that leaves reach their terminal vertical velocity immediately during the descent, whereas in reality, the time required to reach terminal velocity is typically reached asymptotically and depends on the air resistance and weight of the object. The latter assumption may be less critical for litter resulting from broad leaves than needles as drag forces lead needles to reach terminal velocity in a shorter time, but a full consideration of velocity is needed in future work.

Further, the decay functions used in DUET are appropriate for shorter timeframes and xeric sites of the southeastern U.S., but don't include nutrient cycling, including carbon:nitrogen, detritivore effects as described in De Smedt et al. (2018) and climatic effects on litter decomposition rates as described in Gavazov (2010). Further expanding the decay function and adding live and dead fuel moisture information, and grass senescence and decay to the model, would improve model accuracy and expand the range of ecosystems to which the model can be applied.

DUET does not currently include redistribution of litter by the wind or animal tracking once on the ground, which is observed predominantly in hardwood litter (Wade and Lunsford 1989). Many shrub species or trees in shrub stature contribute to the understory characteristics of many surface fire regimes, which are currently included as regular trees but can be added as an additional component to the model.

3.4.5 The need for validation

While the model produces heterogeneity that meets expected patterns for wind, tree height, and litter type, there is a need for both verification and validation. While verification of a model confirms that the model is correctly implemented, validation ensures that the model represents the real system it was built to represent accurately. In this study, we have presented verification of the DUET model by testing the model's representation of various idealized scenarios. However, validation must occur through spatially explicit field data, which are just now becoming available as scales to test DUET (Hawley et al. 2018). We view DUET as a series of hypotheses that brings together the basic influential processes involved in how the canopy affects litter buildup, which will be evaluated against these high-resolution observations in the future.

3.5 List of simulations

Table 3.2: *List of all simulations performed to test various attributes of DUET; PHT = Pine Height, OHT = Oak Height, DCO = Drag Coefficient, DECAY = Decay rate tests, LD = Large Domain, and WFIELD = Windfield; NWNS = No Winds, No Standard deviation; HWNS = High Winds, No Standard deviation; NWHS = No Winds, High Standard deviation; and HWHS = High Winds, High Standard deviation*

Simulation Name	Perturbed Parameter	Domain Size	$m/cell$	Trees	Winds
CHT_NWNS	Tree height	35 × 35 × 25 cells	$1m$	Conifers: $1@10m$, $1@20m$	$u, v, \sigma_u, \sigma_v = 0$
CHT_HWNS	Tree height	35 × 35 × 25 cells	$1m$	Conifers: $1@10m$, $1@20m$	$u, v, \sigma_u, \sigma_v = 20, 20, 0, 0$
CHT_NWHS	Tree height	35 × 35 × 25 cells	$1m$	Conifers: $1@10m$, $1@20m$	$u, v, \sigma_u, \sigma_v = 0, 0, 10, 10$
CHT_HWHS	Tree height	35 × 35 × 25 cells	$1m$	Conifers: $1@10m$, $1@20m$	$u, v, \sigma_u, \sigma_v = 20, 20, 10, 10$
BHT_NWNS	Tree height	35 × 35 × 25 cells	$1m$	Broadleaf: $1@10m$, $1@20m$	$u, v, \sigma_u, \sigma_v = 0$
BHT_HWNS	Tree height	35 × 35 × 25 cells	$1m$	Broadleaf: $1@10m$, $1@20m$	$u, v, \sigma_u, \sigma_v = 20, 20, 0, 0$
BHT_NWHS	Tree height	35 × 35 × 25 cells	$1m$	Broadleaf: $1@10m$, $1@20m$	$u, v, \sigma_u, \sigma_v = 0, 0, 10, 10$
BHT_HWHS	Tree height	35 × 35 × 25 cells	$1m$	Broadleaf: $1@10m$, $1@20m$	$u, v, \sigma_u, \sigma_v = 20, 20, 10, 10$
DCO_NWNS	Drag Co = 1.28 and 0.6	35 × 35 × 25 cells	$1m$	2 identical Conifers	$u, v, \sigma_u, \sigma_v = 0$
DCO_HWNS	Drag Co = 1.28 and 0.6	35 × 35 × 25 cells	$1m$	2 identical Conifers	$u, v, \sigma_u, \sigma_v = 20, 20, 0, 0$
DCO_NWHS	Drag Co = 1.28 and 0.6	35 × 35 × 25 cells	$1m$	2 identical Conifers	$u, v, \sigma_u, \sigma_v = 0, 0, 10, 10$
DCO_HWHS	Drag Co = 1.28 and 0.6	35 × 35 × 25 cells	$1m$	2 identical Conifers	$u, v, \sigma_u, \sigma_v = 20, 20, 10, 10$

Table 3.3: *List of all simulations performed to test various attributes of DUET; PHT = Pine Height, OHT = Oak Height, DCO = Drag Coefficient, DECAY = Decay rate tests, LD = Large Domain, and WFIELD = Windfield; NWNS = No Winds, No Standard deviation; HWNS = High Winds, No Standard deviation; NWHS = No Winds, High Standard deviation; and HWHS = High Winds, High Standard deviation*

Simulation Name	Perturbed Parameter	Domain Size	$m/cell$	Trees	Winds
DECAY˙0.1	Decay rate = 0.1	200 × 200 × 41 cells	$2m$	2163 trees - Oak and Pine	Various winds for 5 years
DECAY˙1.0	Decay rate = 1.0	200 × 200 × 41 cells	$2m$	2163 trees - Oak and Pine	Various winds for 5 years
DECAY˙0.5	Decay rate = 0.5	200 × 200 × 41 cells	$2m$	2163 trees - Oak and Pine	$u, v, \sigma_u, \sigma_v = 0$
WFIELD	wind field	200 × 200 × 41 cells	$1m$	2163 trees - Oak and Pine	Windfield developed in HIGRAD

CHAPTER 4. Detecting Chaos in Fire

The material presented below is part of the article that is in preparation for *Chaos: An Interdisciplinary Journal of Nonlinear Science*.

4.1 Introduction

For this project, we use a CFD model, HIGRAD-FIRETEC (Linn et al. 2002; Linn et al. 2005), a coupled atmospheric-fire behavior model (which we shall refer to as "FIRETEC" from here on) that has been utilized in numerous studies, including those examining fire propagation (Pimont et al. 2011), fire effects (Linn et al. 2002; Pimont et al. 2016), and the impact of fuel treatments (Marshall et al. 2020). We choose this model for our study due to the high-fidelity mass and energy resolutions present in FIRETEC.

Clements et al. (2015) demonstrated that low intensity fires are sensitive to shifts in near-surface wind dynamics through field collected data during nine burns on different plots. Linn et al. (2021) used one of those experimental burns to inform a FIRETEC simulation to further illustrate that small changes in the wind field can have a broad effect on fire behavior. Jonko et al. (2021) used an ensemble approach with FIRETEC simulations that focused on low-intensity fires in which they compared 45 simulations with identical conditions except for small perturbations in the ambient wind field. All of these studies clearly indicate that macroscopic fire behavior is sensitive to small perturbations in wind conditions. This sensitivity to small perturbations in initial conditions is a hallmark feature of chaos and nonlinear dynamics.

There have been several studies done on the nonlinear dynamics of fire behavior. Turcotte et al. (2007) found self-organized criticality in the frequency of forest fires relating to the area burned, promoting the concept of scale-invariance in fire occurrence. Similarly, Ricotta, Avena, and Marchetti (1999) also examined self-organizational trends in wildfire occurrence in Ligurnia, showing that the ignition mechanism may have the most impactful effect on how it organizes. The most recent example of chaos theory applied to fire behavior presents a discrete set of equations developed from a reaction-diffusion equation, similar to the derivation of Lorenz equations for wind dynamics (Mampel, Egorova, and Pagnini 2023; Lorenz 1963). We employ nonlinear time series analysis to detect the presence of chaos in model-derived fire behavior data (Kantz and Schreiber 2003; Malik 2020).

Although there is still some debate on specific mathematical properties of chaotic systems, a system can be defined as chaotic if it presents sensitivity to initial conditions and deterministic behavior (Lorenz 1963; Sander and Yorke 2015). Deterministic implies that if we input a unique input into the system, we will always see a corresponding unique output from the system. Sensitivity to initial conditions implies that if we introduce an arbitrarily small perturbation to that unique input, the corresponding output may change considerably. There are several methods for detecting the presence of deterministic chaos in a time series. The most well-known among these is estimating the maximal Lyapunov exponent, for which there exist several algorithms (Grassberger and Procaccia 1983; Wolf et al. 1985; Eckmann et al. 1986; Sato, Sano, and Sawada 1987; Rosenstein, Collins, and De Luca 1993; Touzé and Chaigne 2000; Akemann, Burda, and Kieburg 2019; Strogatz 2019). These methods measure the divergence between two trajectories that begin infinitesimally close together, with the maximal Lyapunov exponent representing the rate of this divergence. Another typical testing method involves calculating several different types of fractal dimensions. Each fractal dimension offers insights into the system dynamics over time and gives a measurement of complexity (Lai and Lerner 1998; Sprott and Rowlands 2001; Lacasa and Gómez-Gardeñes 2013; Strogatz 2019).

Accurately estimating Lyapunov exponents and fractal dimensions to determine the presence of chaos can be challenging when the time series have limited lengths since the existing methods fail to converge in such situations (Decoster and Mitchell 1991; Gencay and Dechert 1992). The techniques used in calculating Lyapunov exponents and some fractal dimensions require determining two parameters: the embedding dimension, the minimum dimension needed to reconstruct a topologically equivalent attractor to the attractor in the underlying data, and a time delay which removes any temporal correlations in the time series to avoid oversampling of the data which could suppress any chaotic signals. These parameters form the basis for phase-space reconstruction of the dynamical system underlying the time series, and Lyapunov exponents and fractal dimensions can be highly sensitive to the choices of these parameters. Reliable evaluation of the values for these parameters can be challenging for shorter time series with limited knowledge of the system, especially in the presence of noise (Wolf et al. 1985; Eckmann et al. 1986; Rosenstein, Collins, and De Luca 1993). Also, with a short time series, a time delay embedding can reduce the length of the series even further which increases the potential for lack of convergence in the method. On the other hand, without the embedding, we risk oversampling the data which flattens out the dynamics and can lead to false results. These methods are also computationally expensive, and often require manual investigation and adjustment of parameters for every series under study. However, as this project involves thousands of time series and will therefore require automation, individual time-series adjustments are not feasible.

Instead of these more classic chaos detection methods, we use the recently developed Chaos 0-1 test (C01) that uses ergodic theory and Fourier analysis to find the asymptotic growth rate of the mean squared displacement in a given time series (Gottwald and Melbourne 2004). We couple this test with an artificial neural network (ANN) that distinguishes between deterministic and stochastic series using ordinal analysis and permutation entropy (Boaretto et al. 2021). For our data, we develop a simulation using FIRETEC, with homogeneous fuels, moderate moisture levels, and low winds. Employing four variables produced by FIRETEC for each cell in the domain, we design several thousand one-dimensional time series from the curated simulation that we test for chaotic qualities using the C01 and ANN tests. We examine these results by variable and series format, and compare them to known phenomena in physical fire behavior. We show that all four variables modeled in FIRETEC display a wide range of behavior from stochastic to deterministic with chaos expressed through the majority of the results.

4.2 Data and Methods

We design these time series with "marginal" fire conditions defined as a fire whose conditions are designed to be just on the tipping point of extinguishment and sustainable combustion to propagate through the domain. The transition between these states tends to be highly sensitive to atmospheric and surface conditions. Since our time series are designed with this sensitivity in mind, we assume the simulation is straddling this transition point and will produce both non-chaotic and chaotic regimes. In addition, we know that fire behavior is nonlinear. The sensitivity to wind dynamics viewed in low-intensity fire field experiments (Clements et al. 2015) and previous FIRETEC simulations (Jonko et al. 2021; Linn et al. 2021) inspires the possibility that a transition into chaos is possible in these types of fires.

In this study, we generate time-series from simulations using FIRETEC, a coupled fire-atmosphere behavior model, to evaluate the chaotic qualities in simulated fire behavior. To assess the presence of chaos, we use the chaos 0-1 test developed by Gottwald and Melbourne (2004) and an artificial neural network developed by Boaretto et al. (2021) each of which is described in detail below.

4.2.1 Data

FIRETEC

Although there are various options within the FIRETEC model, we design our series to remove any stochastic functions, configuring the program to be fully deterministic. This includes removing the monte-carlo based radiation program and replacing it with a simpler radiation sink since convective heat transfer is the main fire spread mechanism, and turning off the options for firebrands or spotting as this phenomena is minimal in grass fires.

FIRETEC is a Eulerian CFD model simulating the spatio-temporal behavior of fire using Cartesian (X,Y,Z) spatial coordinates. We use a domain size of $X = 200$ and $Y = 1200$ with horizontal resolution of 2 m $\times$ 2 m for each cell. We have $Z = 41$ vertical cells employing a cubicly stretched grid ranging from ≈ 1.5 m tall near the surface to ≈ 40 m tall near the top of the atmosphere, resulting in a total domain height of 615 m as defined in Linn et al. (2005). Fuels (vegetation) are resolved in 3 dimensions at the model's grid resolution, and characterized by species variables such as moisture, height, and density. We limit our fuel to homogeneous grass to reduce the number of variables that could affect the fire behavior and change our results. Our grass is 0.3 m tall at 0.3 kg/m^2 with 15% moisture as designed in Jonko et al. (2021).

The advantage of using FIRETEC for this analysis is the large amount of information produced from the simulation. For this analysis, we use two fire variables: the temperature of the solid

(T) and the convective heat transfer (Q); and two wind variables: the horizontal wind magnitude ($UV = \sqrt{u^2 + v^2}$), and the vertical wind velocity (W). T is measured in Kelvin (K) and is defined as the temperature of the combination of the grass and the enclosed water (the “solid”), and is representative of the energy consumed by the fuel. The convective heat transfer, Q, can be defined as the energy transferred from the gas to the solid fuel in a cell and has units W/m^2. The wind variables are both defined in m/s. Each of these are recorded per cell for every time step. For a detailed description of the governing equations in FIRETEC for the variables we choose to study, please see Appendix A.

We simulate a wind field where the primary wind direction flows along the long side (Y) of the domain with an average speed of 6 m/s at $\approx$ 150 m high in the domain. Turbulence is generated through randomly placed blocks of vegetation in the lowest five layers of the domain ($1 \leq z \leq 5$) in which the number of blocks exponentially reduce as we get higher in the domain. These blocks interrupt the flow field, causing turbulence in the winds. Boundary conditions are defined to be cyclic perpendicular to the primary wind direction. Cyclic boundary conditions essentially make the domain laterally infinite as described in Linn et al. (2012), allowing flow to pass through the boundary on one side, and back into the domain on the other side and allows us to consider each x-coordinate as a separate “fire event” for our time series. To avoid any influence from the boundary conditions at the lower edge of the domain, we define an ignition transect two cells thick at 100 cells away from $Y = 0$. We “ignite” each $x \in X$ along this transect by removing all fuel moisture and linearly increasing T to 1000K over the first 3.5 seconds of the simulation (Linn et al. 2005). The laterally infinite domain coupled with an ignition line that spans the entire width creates an “infinite fireline,” which virtually eliminates any edge effects for the simulation that may interfere with the study.

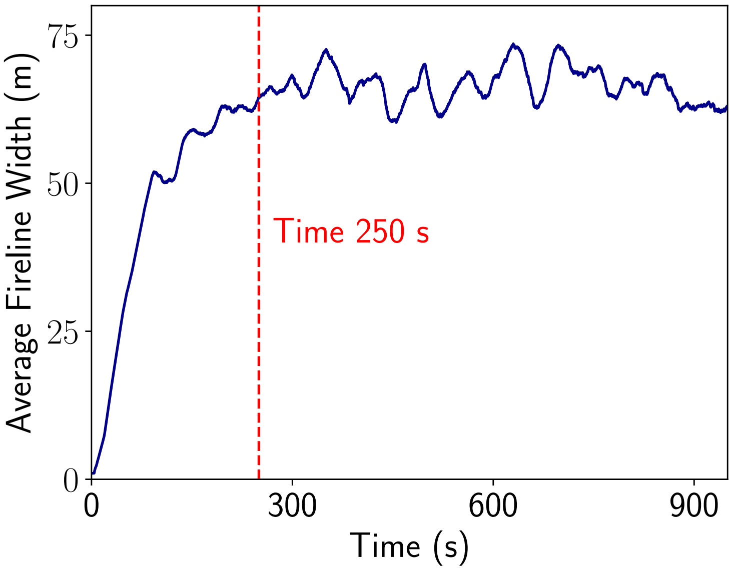

Figure 4.1: *Average fireline widths for each time step; vertical line at* 250 *s shows the starting point for each time series developed. Note that at* 250 *s, we have reached a level average state after the initial ramping of the fire behavior due to ignition.*

To avoid sampling any unusual fire behavior due to the non-physical ignition, we record simulation data from 250 seconds to 950 seconds, creating 7001 time steps per series with each time step representing 0.1 seconds of the simulation. This timing is chosen to allow for the full formation of the fire after the ignition, which can be determined by examining the average fireline width for each time step. The fireline width is defined as the distance between the cell that has a temperature $T \geq 500K$ and is farthest from the ignition, and the cell that is closest to the ignition to reach the same threshold. Once the average fireline width ceases growth beyond the noise of the simulated environment, we consider it to no longer reflect the non-physical characteristics of the ignition. Figure 4.1 shows the average fireline width for each time step of our simulation with a vertical line at 250 s, after which point the fireline width has stabilized. The end of the simulation is defined to be before the fireline reaches the end of the domain space.

Time Series

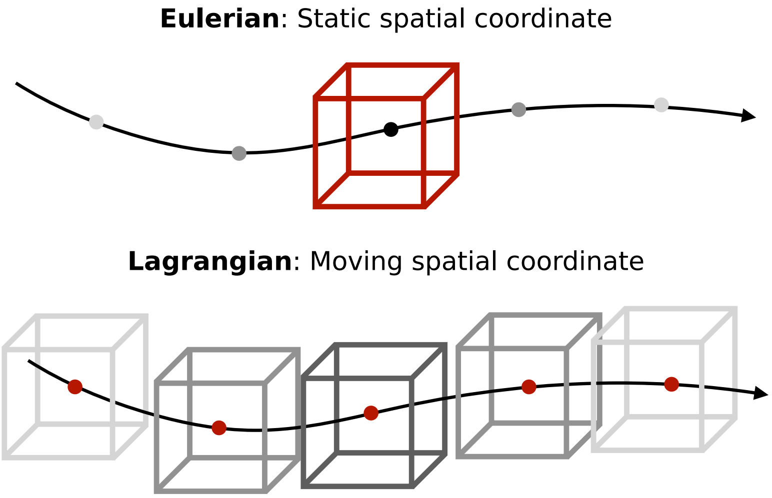

Figure 4.2: *Diagram to illustrate the difference between Lagrangian and Eulerian time series. Eurlerian series track how the fluid at a particular spatial location changes through time. Lagrangian style series track how a particular fluid parcel changes in space over time.*

FIRETEC output is Eulerian (values recorded for each cell per time step). To determine the presence of chaotic behavior in the changes for each variable through time and space, we choose a Lagrangian style time series (Fig. 4.2) to track how the energy moves through the domain in the form of heat. To convert the Eulerian data to a Lagrangian format we track the movement of the fireline through time for individual x-coordinates in the domain. The fireline, referred to hereafter as $Y_s(x)$, is defined as the series of spatial y-coordinates farthest from the ignition line that achieve a temperature of the solid $T \geq 500\text{K}$ for each time step $s \in S = \{250.0, 250.1, ..., 950.0\}$. Figure 4.3 shows a top down view of time step $s = 2800 = 280$ s from the simulation. Note the broad area that is actively on fire ($T \geq 500\text{K}$) in black. The off-white line at the top of the black area depicts the leading edge of the fire as it progresses upward.

Table 4.1: *Table showing the various time series types we developed that use each x-coordinate as a separate fire event. v represents the variable for the time series, n shows the offset from* $Y_s(x)$*, for all time steps s. See Eqns. 4.5 through 4.8.*

Name	Description
$F_v(x)$	Values of each variable $v \in V$ for the fireline locations
$I_{v,n}(x)$	Values of each variable for cells in front and behind in line with $F_v(x)$
$C_{v,n}(x)$	Difference between the values at the fireline and cells in front and behind in line with $F_v(x)$
$L_{v,n}(x)$	Values of each variable for the fireline locations and lateral cells to the left and right, perpendicular to $F_v(x)$
$O_{v,n}(x)$	Difference between the fireline and cells to the left and right, offset along the fireline

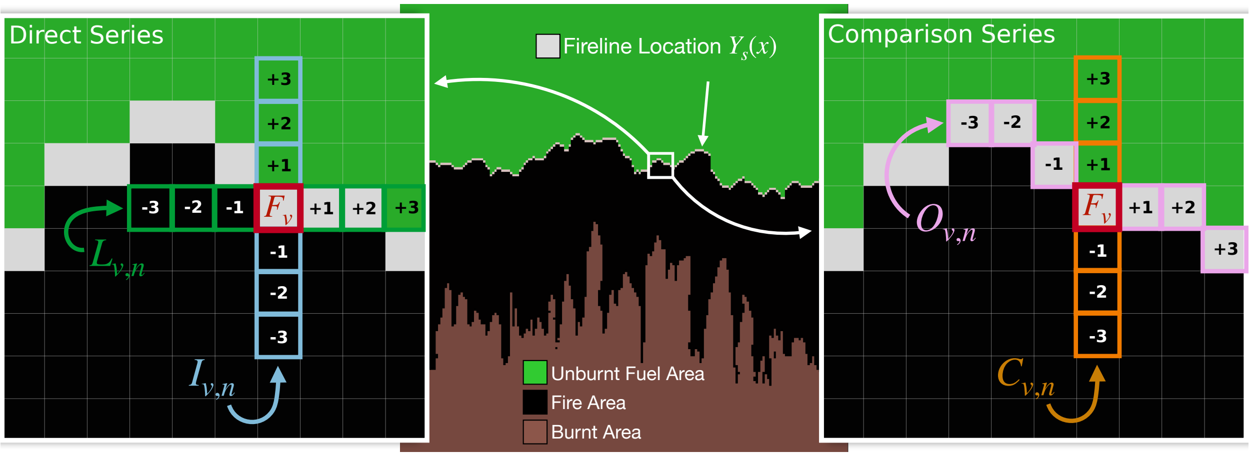

Figure 4.3: *Top down visualization of the time step related to 280 s from the FIRETEC simulation. The fireline location is defined as* $Y_s(x)$ *for the y-coordinate at location* $x \in X = \{5, 10, 15, ..., 195\}$ *at time* $s \in S = \{250.0, 250.1, ..., 950.0\}$*.* $F_v(x)$ *is the value of the variable* $v \in V = \{Q, T, UV, W\}$ *at location* $Y_s(x)$*. The fireline location is in off-white, the unburnt fuel area is in green, the burnt area is in brown and the locations that are actively on fire are in black. The small white box is blown up on either side to show the Direct time series and the Comparison time series. Direct takes values directly from the variable matrices; comparison finds the difference between* $F_v(x)$ *and the values at the particular offset (n) location*

Using the fireline, $Y_s(x)$, we develop a variety of time series that investigate the fire behavior from several perspectives. Table 4.1 gives a list of the time series developed from the x-coordinates in the domain and Fig. 4.3 shows visual representations. A full description of each style of time series is below.

To reduce computational expense for our analysis, the four series described in Table 4.1 are created using every 5 cells from $5 \leq x \leq 195$ and each of the four variables are described at the top of this section and in Appendix A. For the equations that follow, we define these sets:

$$V = \{Q, W, UV, T\}, \tag{4.1}$$

which defines the matrices of variables that are used in each of the series. Each of these variable matrices are 200×1200 cells, recorded from the FIRETEC simulation for each time step in the bottom vertical layer ($Z = 1$). Then we have,

$$X = \{5, 10, 15, ..., 195\}, \tag{4.2}$$

that defines the 39 x-coordinates used in this analysis. Likewise, the offset coordinates for each time series N, are defined such that:

$$N = \{-3, -2, -1, 1, 2, 3\}. \tag{4.3}$$

As defined above, $Y_s(x)$ is the y-coordinate for the fireline at time step s for a particular x-coordinate.

The base set of time series are built from the values of each variable at the fireline, $(x, Y_s(x))$:

$$F_v(x) = \{v(x, Y_s(x))\}_{s \in S} \tag{4.4}$$

We include a modified version of F_v defined as $\hat{F}_v$ in which we only consider every other time step in S, such that $S^* = \{250.0, 250.2, ..., 949.9\}$ and $\hat{F}_v(x) = \{v(x, Y_s(x))\}_{s \in S^*}$ for test validation purposes.

The first “Direct” series, $I_{v,n}(x)$, tracks each variable for the three coordinates in line with the movement of $F_v(x)$, in front and behind $F_v(x)$ $\forall n \in N$:

$$I_{v,n}(x) = \{v(x, Y_s(x) + n)\}_{s \in S}. \tag{4.5}$$

The second “Direct” series, $L_{v,n}(x)$ shows the value at corresponding lateral coordinates to the left or right of each specific $F_v(x)$ for all $v \in V$ and $n \in N$:

$$L_{v,n}(x) = \{v(x + n, Y_s(x))\}_{s \in S}. \tag{4.6}$$

The first “Comparison” series, $C_{v,n}(x)$, Finds the difference in the value at the fireline, $F_v(x)$, and those corresponding coordinates in front or behind $F_v(x)$ for all $v \in V$ and $n \in N$:

$$C_{v,n}(x) = \{v(x, Y_s(x) + n) - F_v(x)\}_{s \in S}. \tag{4.7}$$

$O_{v,n}(x)$ shows the difference between the value at the fireline and corresponding coordinates to the left or right of each coordinate, following the path of the fireline for all $v \in V$ and $n \in N$:

$$O_{v,n}(x) = \{v(x + n, F_s(x + n)) - F_v(x)\}_{s \in S}. \tag{4.8}$$

Note that each $v \in V$, $n \in N$, and $x \in X$ produce different series for each of these types, resulting in a total of 3900 different time series (975 per variable) used in this study. The above equations are visualized in Fig. 4.3. Since the I and L series are built directly from the variable values, we refer to them as the "Direct" series; then C and O are considered the "Comparison" series.

4.2.2 Chaos Detection Methods

We analyze each of the time series described in Sec. 4.2.1 using the chaos 0-1 test (C01) coupled with an artificial neural network (ANN) for distinguishing between stochastic and deterministic chaotic behaviors. An advantage of the two tests we use for this project is that they provide several different insights into the underlying system. The C01 test can identify whether the system is chaotic ($K \geq 0.5$) or non-chaotic ($K < 0.1$), and it is inconclusive when $K \in [0.1, 0.5)$. The inconclusive range for the C01 test does not necessarily infer the absence of chaotic dynamics in the system but that the results require a more in-depth analysis of the series before concluding the level of chaos present (Gottwald and Melbourne 2008). As designed, the C01 test was developed to identify *deterministic* chaos (Gottwald and Melbourne 2004, 2016). Thus, some of our results that indicate chaos may be stochastic as described in Sec. 4.2.2, and require an additional test to rule out stochasticity. The ANN test recognizes stochasticity with two results, classifying dynamics as stochastic ($\Omega < 0.1$) or deterministic ($\Omega \geq 0.1$).

The 0-1 Test

The chaos 0-1 test (C01) has been successfully applied for various time series of experimental data, demonstrating its robustness in identifying chaotic phenomena in different real-world settings (Litak et al. 2009; Litak, Syta, and Wiercigroch 2009; Savi et al. 2017; Ouannas et al. 2020). C01 analyzes the asymptotic growth rate between time steps in a given series (Gottwald and Melbourne 2004, 2009, 2016). The growth rate is defined as the slope of a line fit to changes in the mean squared displacement as the duration between time steps increases. When the series is chaotic, the rate will be close to 1, and the translated data will appear disorganized. If the series is non-chaotic, the growth rate will be close to or less than 0 and the translated data appears bounded and symmetric. For values that lie in between 0.1 and 0.5, an inspection of the visualizations for each step should be included to verify the existence of weak chaos or the presence of stability (Gottwald and Melbourne 2008).

The test involves four steps to calculate the asymptotic growth rate between values through time. For this description, we have reproduced all equations from Gottwald and Melbourne (2016). The first step translates each of the time series data points using sin and cos functions, similar to using the power spectra. Consider a time series $\phi(s),\ \ s = 1,...,n$. Then we translate for each $c \in \{C_n\}$:

$$p_c(n) = \sum_{s=1}^{n} \phi(s)\cos(sc) \qquad q_c(n) = \sum_{s=1}^{n} \phi(s)\sin(sc) \tag{4.9}$$

where we define $\{C_n\}$:

$$\{C_n\}_{n=1}^{100} \in_R \left[\frac{\pi}{5}, \frac{4\pi}{5}\right] \tag{4.10}$$

where values are randomly chosen from a uniform distribution and applied to this interval, then sorted from smallest to largest.

The second step in the process is to calculate the mean squared displacement for the p's and q's for each $c \in \{C_n\}$. Using the first tenth of the p and q values to avoid undersampling, we define n_{cut} as the closest integer to the total number of time steps divided by 10: $n_{cut} = N//10$ and for each $n \in [1,...,n_{cut}]$, we calculate:

$$M_{c_i}(n) = \lim_{N\to\infty} \frac{1}{N} \sum_{s=1}^{N} [p_{c_i}(s+n) - p_{c_i}(s)]^2 + [q_{c_i}(s+n) - q_{c_i}(s)]^2 \tag{4.11}$$

We then normalize the mean squared displacement using the squared mean of the series and an oscillation factor:

$$V_{osc}(c,n) = \left(\frac{1}{N}\sum_{s=1}^{N} \phi(s)\right)^2 \frac{1-\cos(cn)}{1-\cos(c)} \tag{4.12}$$

such that:

$$D_c(n) = M_c(n) - V_{osc}(c,n). \tag{4.13}$$

Finally, we calculate the asymptotic growth rate for the normalized mean squared displacement using a correlation method. Assuming we have $\vec{n} = \{1,2,3,...,n_{cut}\}$ and $\vec{D}_c = \{D_c(n)\}_{n=1}^{n_{cut}}$, we calculate:

$$K_c = corr\left(\vec{n},\vec{D}_c\right) = \frac{cov(\vec{n},\vec{D}_c)}{\sqrt{var\left(\vec{n}\right), var\left(\vec{D}_c\right)}} \tag{4.14}$$

where we use a typical covariance equation:

$$cov(a,b) = \frac{1}{n_{cut}} \sum_{s=1}^{n_{cut}} (a(s)-\bar{a})(b(s)-\bar{b}) \tag{4.15}$$

and $var(a) = cov(a,a)$. To avoid possible resonance for various c, we define the K value to be the median value of all calculated K_c which discounts any outliers in the results.

The advantage of the 0-1 test lies within the single value output and the visualizations for each step in the process. To illustrate the usefulness of the method, we used the Logistic map with a parameter known to be stable ($\mu = 3.5$), and one known to be chaotic ($\mu = 3.91$). In Fig. 4.4, the column on the left corresponds to the stable parameter, and the column on the right to the chaotic.

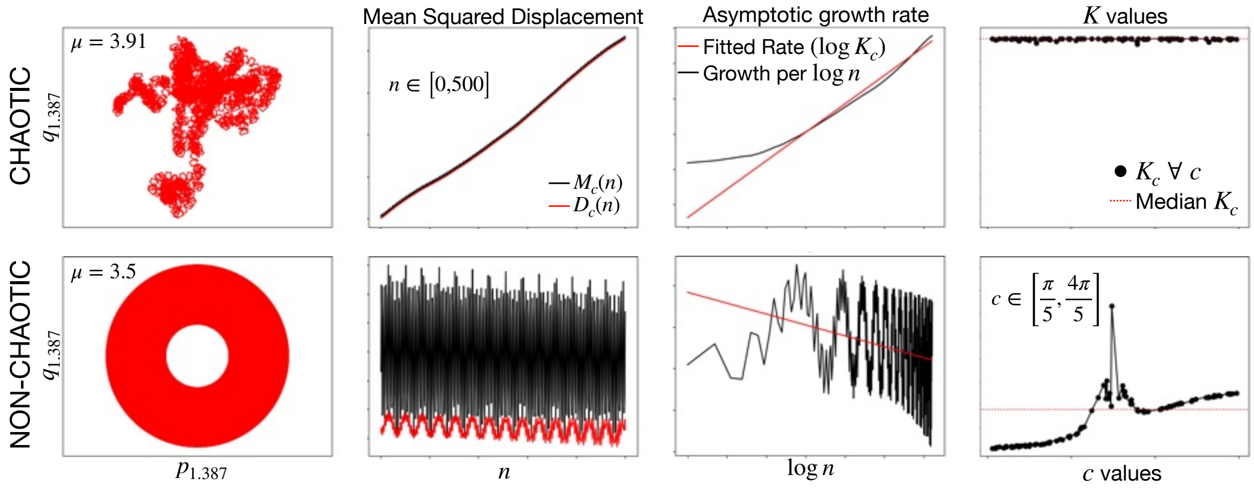

Figure 4.4: *Visual representation of four steps in the Chaos 0-1 test process. Top row relates to a chaotic parameter,* $\mu = 3.91$ *and bottom row relates to a non-chaotic parameter,* $\mu = 3.5$*. Left column is the visual graph of* p_c *versus* q_c*. Second column is the mean squared displacement between values for each c and each n, the third column represents the asymptotic growth rate of the mean squared displacement. The right column is the K results for each c, and the median value. Note the differences in each visual representation for each step.*

Each row represents a step in the process and the graphs clearly depict different behaviors for chaotic or stable systems, showing how easy this method is to interpret.

Figures 4.4a and b show graphs of the translated data for $\mu = 3.5$ (4.4a) and $\mu = 3.91$ (4.4b). In Fig. 4.4a, the stable behavior is structurally symmetric and organized, where in 4.4b we see the disorganization of the time series caused by the chaos. The second row from this image shows the mean squared displacement in blue and the normalized version in red. Figure 4.4c shows the stable case and Fig. 4.4d the chaotic. Note that if we fit a line to either the blue or red lines they will have the same slopes which indicates that this normalization process does not affect the growth rate we seek.

The third row of graphs in this figure (Fig. 4.4e and f) show the calculation of the growth rate. We can see that the growth rate in the stable case is declining which indicates stability, and the growth rate for the chaotic case is increasing, confirming the presence of chaos. The test translates the data using a variety of different translation variables between $\pi/5$ and $4\pi/5$. We then use the median growth rate for all of the transition variables so as to avoid resonance or outliers. The last row in Fig. 4.4 shows the calculated growth rate for several translation variables. We can see in Fig. 4.4g that the calculated growth rate for stable behavior in the Logistic map is below 0 when we discount the outlier. For the chaotic case in Fig. 4.4h, all of the values are within $[0.95, 1]$ which clearly indicates chaos as the values are all close to 1. Note that Fig. 4.4g shows the benefit of using the median value to avoid any effect caused by outliers.

Chaotic or Stochastic

Stochastic and chaotic time series have similar characteristics, which creates challenges in distinguishing between the two (Dämmig and Mitschke 1993; Rosso et al. 2007). A variety of methods have been developed for distinguishing these states, including using the Shannon entropy, using a Horizontal Visibility Graph method in conjunction with the correlation dimension, or incorporating machine learning algorithms (Rosso et al. 2007; Lacasa and Gómez-Gardeñes 2013; Boaretto et al. 2021). As with the Lyapunov exponent estimation, many of the above methods require phase-space reconstruction using the time delay embedding parameters. In our case, determining these parameters is challenging due to the short length of individual time series in our data and the lack of algorithms that can estimate these parameters for a large number of time series in an automatized way. Therefore, we choose to use the open source artificial neural network (ANN) that is designed to make this distinction using permutation entropy (PE) and does not require determination of time delay embedding parameters (Boaretto et al. 2021). PE finds ordinal relations between the values of time series and calculates the probability of these patterns. This approach gives a quantity of complexity or irregularity of the system and how it changes between time steps (Henry and Judge 2019).

Permutation entropy is calculated by investigating different sequences in each time series and finding the probability of each permutation. As an example, consider the series $\{B, D, A, C, E\}$. If we use ordinal analysis and split the series into sequences of length $r = 3$, we have $\{B, D, A\}$, $\{D, A, C\}$, and $\{A, C, E\}$ (Bandt and Pompe 2002; Henry and Judge 2019). We assign a permutation to each sequence based on the order of the letters and which come before or after the others in alphabetical sequence. The list of permutations for $r = 3$ includes $r! = 3! = 6$ possibilities: 123, 231, 312, 213, 321, 132.

Consider our first permutation: $\{B, D, A\}$. Since A is the lowest letter in alphabetical order, we assign it a 1. B is the next highest letter, so it becomes 2, and then D is now 3. This makes the permutation, $\{B, D, A\} = 231$. Similarly, we have $\{D, A, C\} = 312$ and $\{A, C, E\} = 123$. We then calculate the permutation entropy of order r for the series as $\sum_{i=1}^{r!} -p_i \log_2(p_i)$. where $r!$ is the total possible permutations of r and $p_i =$ the probability of the ith permutation (Bandt and Pompe 2002).

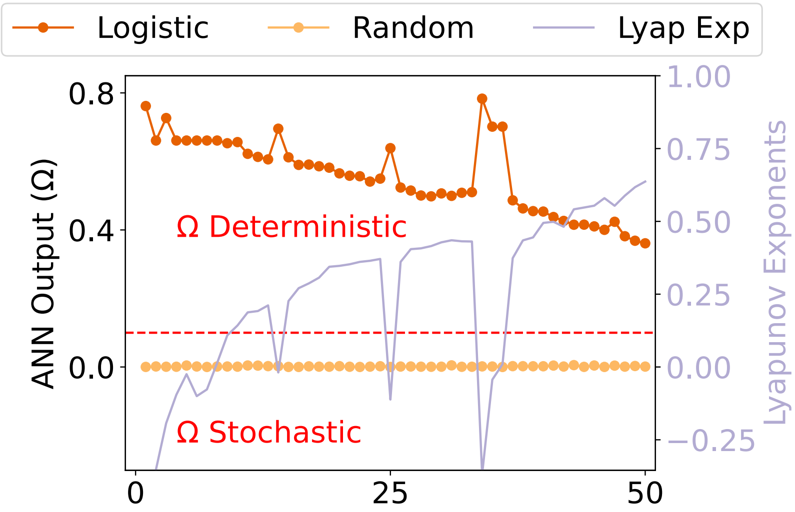

Figure 4.5: *Output for the artificial neural network (ANN) that detects determinism to distinguish between chaotic and stochastic behavior. The Logistic results show deterministic behavior for each run in which the run number relates to evenly spaced parameter values for* $\mu \in [3.5, 4.0]$. *The Random results show that all* 50 *normally random series accurately showed stochastic behavior.*

The ANN is trained on flicker noise to find the permutation entropy of the noise (Boaretto et al. 2021). Flicker noise is a well known stochastic process where the noise is generated from a power spectra in which the frequency is inversely proportional to the spectral density (Barnes and Allan 1966). The ANN then calculates the permutation entropy of the time series of order $r = 6$ and compares the entropy to that of the noise. If the values are similar, (< 0.1 difference) then the time series is stochastic. If the values differ (≥ 0.1), the time series is deterministic.

We validate the ANN using 50 normally distributed random series and the Logistic map with 50 parameter values evenly spaced in $3.5 \leq \mu \leq 4.0$. Fig. 4.5 shows that the ANN output is close to 0 for the normal random series, strongly indicating stochasticity. The logistic map also accurately presents as deterministic for all runs with $\mu \in [3.5, 4]$ in which the system toggles between deterministic chaos and stability. Note that in Fig. 4.5 we can see that there are spikes in the Ω output when the corresponding Lyapunov exponents are negative. Since negative Lyapunov exponents indicate highly deterministic non-chaotic behavior, this figure validates that the test is accurately distinguishing between deterministic and stochastic behaviors.

4.3 Results and Discussion

In the following figures, we represent all 975 series for each variable $v \in V = \{Q, W, UV, T\}$ divided into 39 series at the Fireline, $F_v(x)$, one for each x-coordinate with $x \in X = \{5, 10, 15, ..., 195\}$, and 234 for the $I_{v,n}(x)$ and $L_{v,n}(x)$ "Direct" series, and the "Comparison" series, $C_{v,n}(x)$ and $O_{v,n}(x)$, one for each offset coordinate $n \in \{-3, -2, -1, +1, +2, +3\}$ (Sec. 4.2.1).

Figure 4.6 summarizes the results for all 3900 time series and shows how each result for the tests is distributed among the variables. We see that the series are highly chaotic with 79.4% of the results showing chaos from the C01 test. The results are also highly deterministic with 84.9% of the series showing determinism from the ANN test. The highest variance in results from the C01 test occurs in UV and T, while the stochasticity is only showing in the winds, UV and W. Q exhibits the most deterministic chaos among the four variables. In the following sections, we dive into these results and hypothesize about the motivating factors for some of these outcomes.

4.3.1 Determinism and Stochasticity

If a series is deterministic, we can construct a map that inputs the value at a particular time step, applies the map, and outputs the value of the next time step with reasonable accuracy. Given that we designed our FIRETEC simulation to be fully deterministic, we expect that determinism to show in our results. We can see from the bar charts in Fig. 4.6 that the fire-induced variables are entirely deterministic. The wind variables, however, show stochasticity in 43% of the time series from W and 18% of all series using UV.

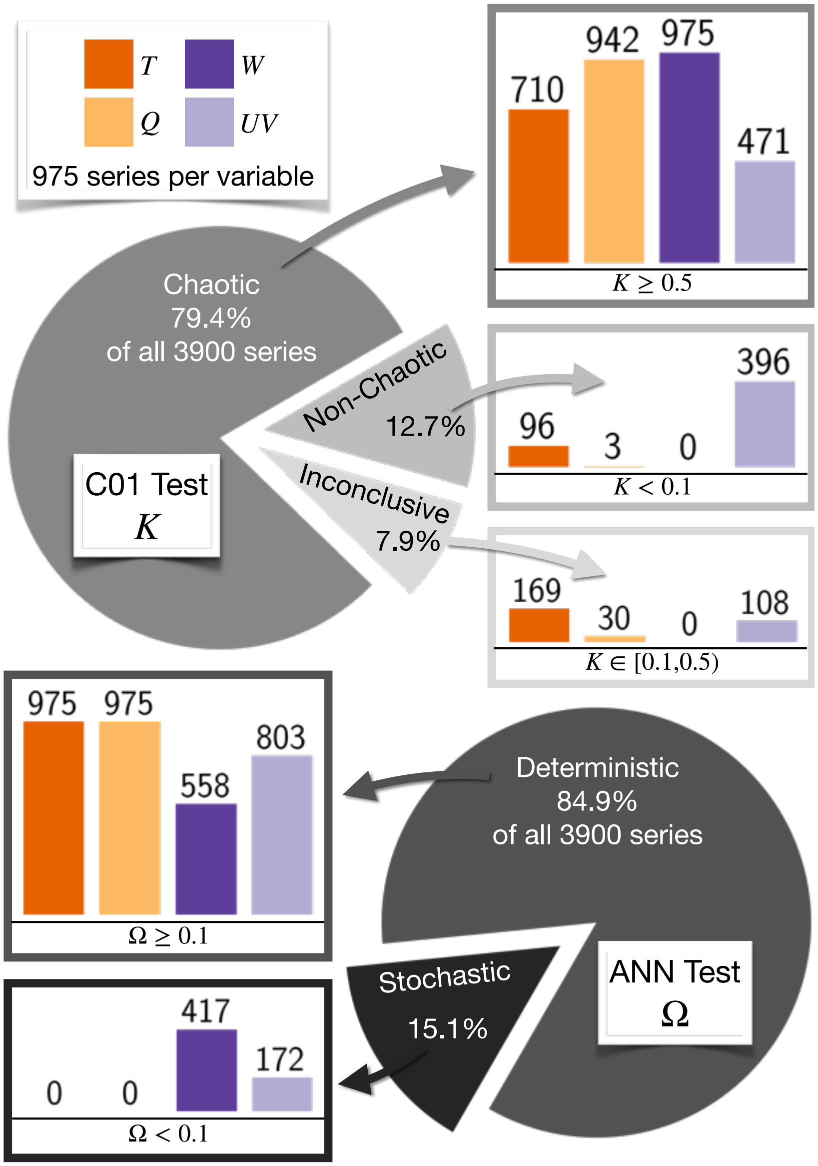

Figure 4.6: *Pie charts showing results for all* 3900 *time series per test. Top pie shows the results of the C01 test (*K*), and the distribution of the results by variable in the corresponding bar charts for each result. Bottom pie shows* Ω *values from the ANN test and their distribution across the variables. Bar charts show how many series of the* 975 *developed per variable that had the corresponding result.*

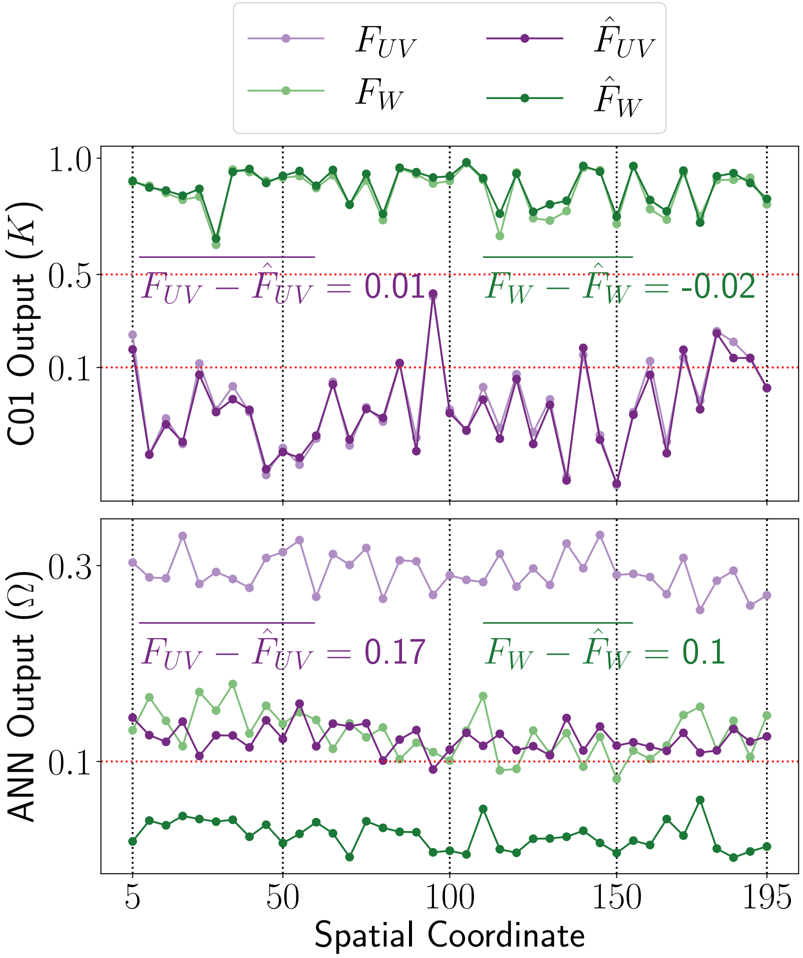

Figure 4.7: *Results for F_W and F_{UV} with the regular time series and another in which only every other time step was used ($\hat{F}_{UV}$ and $\hat{F}_W$). Note that the C01 test does not show sensitivity to the length of the series whereas both shorter time series for these variables shows significantly more stochasticity than the longer series.*

To investigate this phenomenon, we test a time series built from every other time step for each x-coordinate in F_v, doubling the length of the time step, δt from 0.01 seconds to 0.02. These series, $\hat{F}_v$, have only 3500 time steps instead of the original 7001. When we run the C01 and ANN tests on these new series, we see that the C01 test results are very similar for the short and longer series as can be seen in the top panel of Fig. 4.7. The ANN test results, however, change significantly (Fig. 4.7 bottom panel). In fact, the average difference in value for the C01 test is an order of magnitude less than the average difference for the ANN test. This indicates two things: (1) the

C01 test is less sensitive to the length of the series and the sampling rate than the ANN test and (2) the design of our time series in conjunction with the structure of the FIRETEC model is likely breaking the determinism in the system.

FIRETEC is deterministic in three spatial dimensions. However, we construct our time series as one-dimensional series through the domain. We hypothesize that due to the structure of FIRETEC, only knowing the variable values for one specific spatial location may not be enough to be able to map how the system will evolve moving forward. As a three-dimensional system, each cell is affected by the surrounding cells for atmospheric flow fields as well as fire-related dynamics. The interval between time steps, δt influences the radius around the specific cell that will affect the behavior for the next time step. That is, a smaller time step will require a limited amount of spatial information surrounding the target step because the three-dimensional flow fields and combustion processes will not progress as much in a shorter period of time. Alternatively, a longer time step requires knowledge of a correspondingly bigger spatial region since the amount of movement in the atmosphere will be much larger. Since our time series only represent the surface z-layer and a single x-coordinate, we do not include the spatial information for the surrounding cells. This is causing a break in the determinism of the series. Thus, as the time step gets smaller, the series reflect more of the deterministic behaviors, whereas the larger time step in $\hat{F}_v$ show more stochasticity as more information is missing from the deterministic map.

It is not surprising that the wind variables are most affected by the broken determinism, as they are intricately involved in the three-dimensional flow field and turbulence in the atmosphere. Since we limited our fuels to grasses that only exist in the surface layer of the domain, the fire will be more concentrated within that fuel area, and thus require less information from the surrounding spatial coordinates for prediction. Therefore, the fire variables are less affected by the δt. We

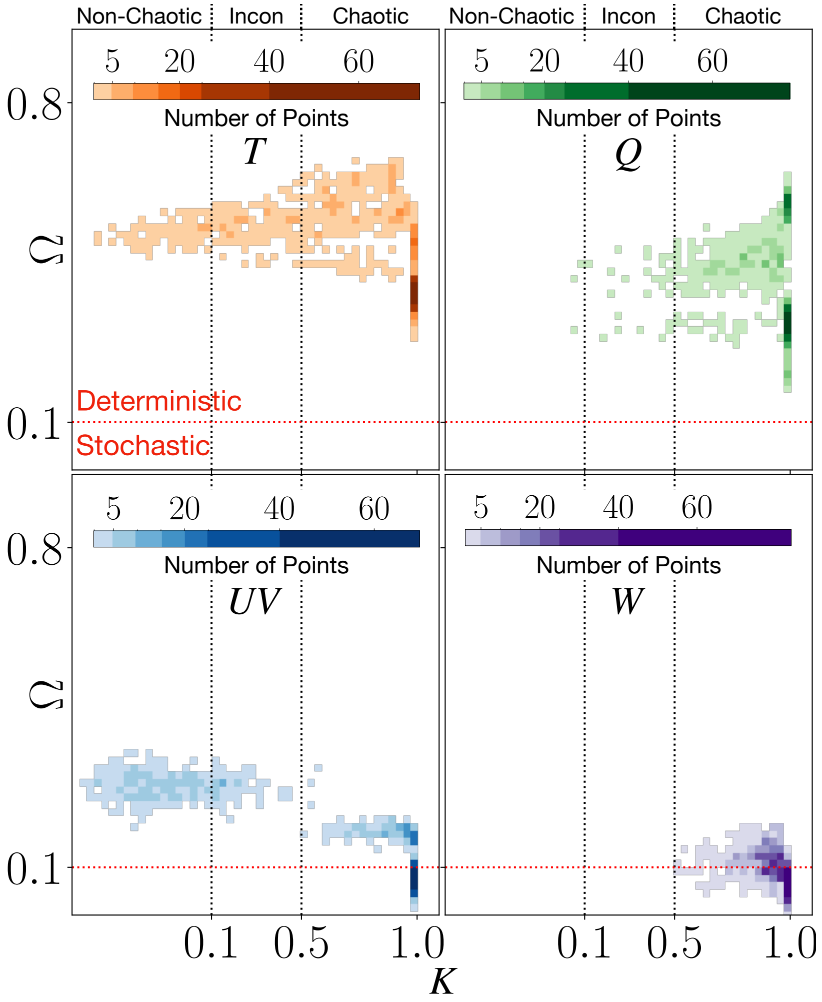

Figure 4.8: *Two-dimensional histogram plot for each variable. Red dotted lines delineate the two output results for the ANN test* (Ω) *with deterministic when* $\Omega \geq 0.1$ *and stochastic when* $\Omega < 0.1$. *Black dotted lines delineate the three output results for the C01 test* (K) *with Non-Chaotic when* $K < 0.1$, *Inconclusive when* $K \in [0.1, 0.5)$, *and Chaotic when* $K \geq 0.5$. *Each variable set contains* 975 *total series.*

expect that a canopy fire may have more influence from all three dimensions and therefore may be more sensitive to the δt.

4.3.2 Variable and spatial analysis

The results are separated by variable in Fig. 4.8 where we observe a cluster in the bottom right corner of each panel. This clustering indicates some consistency within the results for each variable. The W variable is the most tightly clustered in the bottom right of the graph, showing that those series were 100% chaotic from the C01 test with 57% of them being deterministic. The Q series has two clusters with 97% chaotic from the C01 test and 100% deterministic, which means Q has the most deterministic chaos in our set. T and UV are laterally spread out across the graph indicating a variety of C01 results. As stated above, the UV and W results are much lower on the graphs due to the lack of three-dimensional information for the map which likely caused a breakdown in the determinism for the system.

The four variables we investigated for this project are not entirely independent. Convective heat transfer (Q) is defined as the transfer of heat from one location to another due to the movement of air. Therefore, the behavior of Q is heavily dependent on the wind variables UV and W. Similarly, the temperature of the solid (T) is directly affected by the convective heat transfer from the surrounding fuel (see Appendix A.0.3). Thus, although we have separated these components to develop the time series for testing, we must also investigate the results of all four variables together for each type of series to evaluate our conclusions. Even though we have 64.3% of all of the series that are both deterministic and chaotic, we found that only 9% of the time series had all four variables simultaneously exhibit determinism and chaos, translating to only 88 series in each variable. Of those sets of 4 that have either non-chaotic or stochastic behavior for at least one variable, 41% are stochastic in at least one of the wind variables from the ANN test but the C01 test shows chaotic behavior in all 4. Based on the discussion above regarding the stochasticity caused by the length of time step, we may assume that many of those series are actually chaotic, but require a smaller time step for an accurate diagnosis.

Figure 4.9 shows the percentage of the deterministic chaos results for each spatial location per series type. In general, we see more correlation with the fireline within the direct series, except

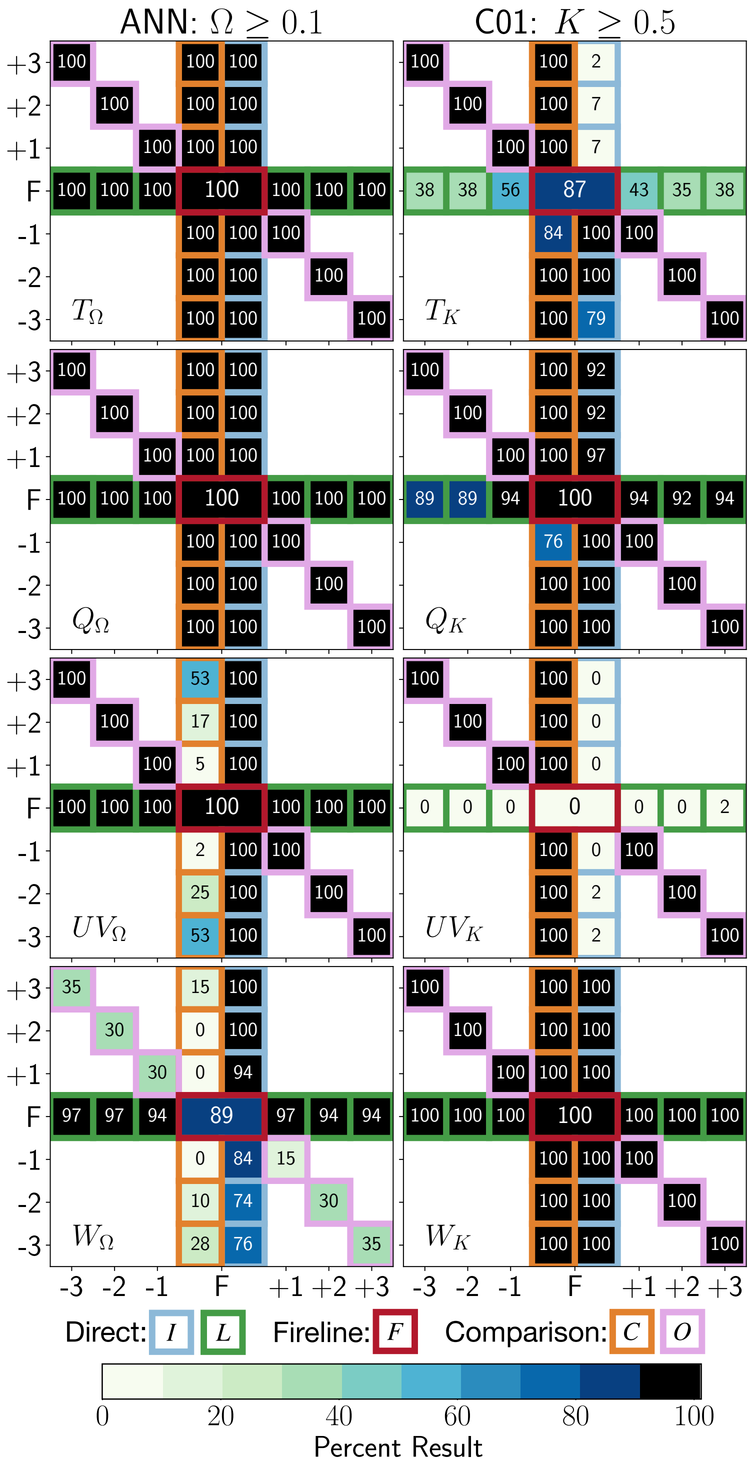

Figure 4.9: *Percentage of results for each series type and offset coordinate. Left column represents a deterministic ANN test ($\Omega \geq 0.1$). Right column represents a chaotic C01 test ($K \geq 0.5$). Rows correspond to variables and the colored borders relate to the series. Axes represent offset coordinates from the fireline F_v as $n \in N = \{-3, -2, ...2, 3\}$.*

in the case of T_K. We know the spatial coordinates immediately in front of the fireline are being heated by convection and are organizing to raise the temperature and begin the combustion process. Thus, we expect there to be less chaos present in the area immediately in front of the fireline. On the other hand, just behind the fireline we are fully engulfed in the fire and thus, we expect to have chaotic behavior as the wind and fuel interact with the ongoing combustion. Panel T_K in Fig. 4.9 shows this spatial phenomenon in our results as the spatial coordinates in front of the fireline ($+1$, $+2$, and $+3$) exhibit very little chaos while those spatial coordinates located behind the fireline (-1, -2, and -3) show highly chaotic results. The effect is less dramatic in panel Q_K as the percents of series showing chaos is still in the 90s in front of the fireline, but there is still a clear difference in front and behind the line. This is an indication that the variables within the fire are indeed chaotic, while those cells undergoing heating before combustion have a broader range of possible results.

The comparison series have much stronger results than the direct series and do not show the same correlation with the corresponding firelines. Only 14 series of type C are inconclusive and only 1 show non-chaotic behavior. This style of series is where the stochasticity shows in the winds. W_K in Fig. 4.9 shows that both comparison series are highly stochastic while the direct series are highly deterministic. We note in Fig. 4.9 that the stochasticity of W for the comparison series (W_Ω) increases as the spatial coordinates approach the fireline. Although these percentages are small (15% in $C_{W,F+3}$, 28% in $C_{W,F-3}$, and 35% for both $O_{W,F\pm3}$), the difference as we approach the fireline is significant with 0% determinism for $C_{W,\pm1}$, and 30% and 15% for $O_{W,F-1}$ and $O_{W,F+1}$ respectively. For the C series, we find something more pronounced in UV where we have 53% for $C_{UV,F\pm3}$ and 5% or less for $C_{UV,F\pm1}$. Since these are series built from the difference between each coordinate and the fireline itself, we assume the fireline is affecting the stochasticity of the winds

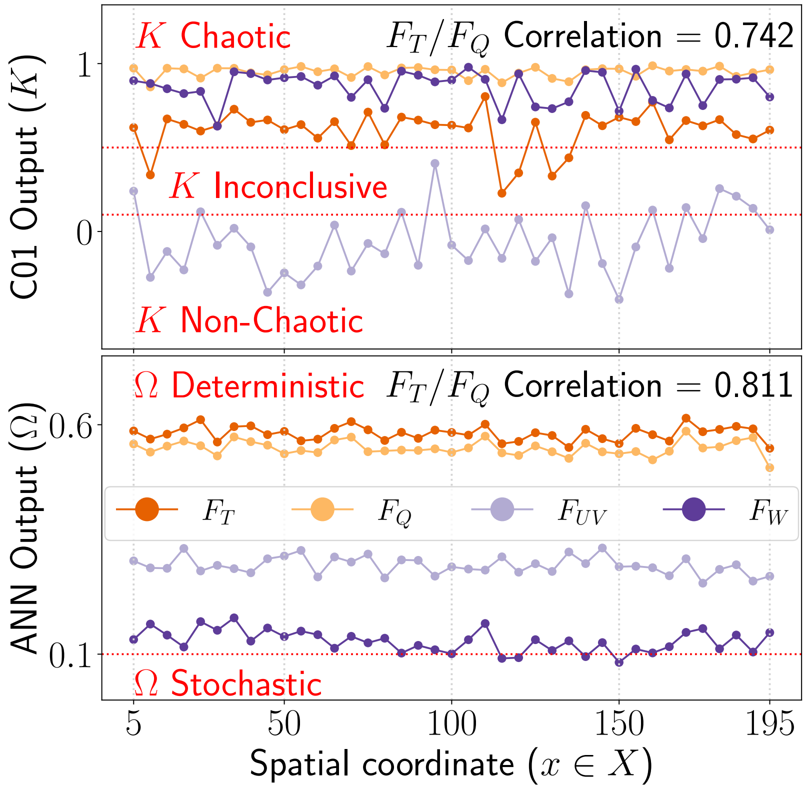

Figure 4.10: *Results per variable for $F_v(x)$ for all 39 spatial coordinates $x \in X = \{5, 10, 15, \dots 195\}$. Panel (a) represents the C01 output (K) and (b) shows ANN output (Ω).*

at the point of ignition, but as we get spatially farther away the values are less affected by the active combustion of that fireline cell.

We observe strong spatial similarity in the complexity of the fire variable dynamics, leading to high correlations in the outcomes. When we compare the two fireline time series F_T and F_Q in Fig.4.10, we see this high level of correlation; that is, when we see a local maximum in F_Q there is often a corresponding local maximum in F_T. The magnitude of these spikes in the C01 K (Fig. 4.10, top panel) result values are much larger in F_T, but the changes in values between neighboring spatial coordinates have similarities. Since the F_Q values are all close to 1, which is the maximum boundary result for this test, we hypothesize that the magnitude of changes between spatial coordinates are suppressed when the values approach that maximum. In the lower panel of

Fig. 4.10, we can see similar local maximum and minimum correspondence for these two variables as well in the ANN Ω output. For this determinism result, the magnitudes of the changes are more closely related, presumably because neither set of results is approaching a boundary for the test results.

4.3.3 Organizing Dynamics

We design these series in relation to the fireline, the point of transition between the combustion processes and the area being heated in front of the line. All of the F_{UV} series are non-chaotic or inconclusive and the other three variables are clustered with F_Q showing all deterministic chaos and the most clustered values for all series, as can be seen in Fig. 4.10. F_W is also all chaotic from the C01 test, but 4 series show stochastic behavior. F_T shows a high level of determinism from the ANN test, but 5 of the 39 series have an inconclusive C01 test. In Fig. 4.9, we see that F_{UV} shows no chaotic behavior at all at the fireline and very little in the surrounding cells from I and L, while these same spatial coordinates are 100% chaotic in W. We assume that this lack of chaos in the horizontal wind magnitude is due to the effects of entrainment. As the heat from the flames push the winds upwards during combustion, winds are drawn in from the surrounding atmosphere (Linn 2019). Since the domain is cyclic to create an infinite fireline, these winds are only drawn in from in front and behind the line. As a result, the horizontal winds close to the fireline self-organize into these indrafts, reducing the chaotic dynamics (Linn et al. 2012; Canfield et al. 2014).

From the work of Drossel and Schwabl (1992), Ricotta, Avena, and Marchetti (1999), and Turcotte et al. (2007) we know that fire is a self-organizing system. This implies that the system tends toward certain organizational patterns. In fire dynamics, this includes fire whirls and the development of counter-rotational vortices which lead to towers and troughs (Banerjee et al. 2020;

Lareau et al. 2022). The high level of correlation between F_v and the I_v series indicates that there is a relationship between the fireline and those corresponding coordinates in front and behind the line. This could be an indication of self-organizing behavior. In particular, our work recognizes some spatial commonalities in the series among the fire-induced variables T and Q. These commonalities may indicate new organizing dynamics that will need to be investigated further.

There are several previous publications regarding the "towers and troughs" organizational behavior in fire (Finney et al. 2015; Banerjee et al. 2020). This phenomenon shows the relationship between the atmospheric turbulence and the heat from the fire creating counter-rotational vortices in the area of the flames. The towers are large updrafts of wind that push the flames upwards, coupled with troughs in which the flames are suppressed by the drawing of that updraft into the tower (Banerjee et al. 2020). This is one example of a self-organizing behavior within fire dynamics. It is plausible that since we are using univariate time series, the variance in behavior is showing these towers and troughs inside the fireline. We postulate that if we could track the towers and troughs as the fire moves through the domain, we could begin to see how each of these series are affected by their position within this phenomenon.

4.3.4 Conclusions

This study produced a broad range of results, with implications that the dynamics represented in FIRETEC within the fire are indeed chaotic and not random. In particular, we find:

- **Stochasticity Comes From Series and Program Design.** Although we design the configuration of FIRETEC to be a deterministic algorithm, the time series for this project show some stochasticity. After investigation we find the determinism of the system to be sensitive to the length of the time step interval due to dimension reduction methods. More investigation into different time step intervals is needed.

- **Fire Variables are Chaotic.** Fire induced variables for the temperature of the fuel (T) and the convective heat transfer (Q) are deterministic and highly chaotic.
- **Spatial Relationships Affect Chaotic Signals.** In front of the fireline there is a significant decrease in chaotic dynamics from the fireline itself. This is not surprising as the chaotic qualities of the fire behavior are most likely not present until the moment of ignition.
- **More Work is Needed.** We discussed a variety of hypotheses in this paper, each of which should be investigated more thoroughly. In particular, more investigation into the stochastic signals using finer time step data may help to define the sensitivity of the determinism within the program.

CHAPTER 5. Conclusions

We set out to enhance existing fire models by providing support models and research to advance the field of fire science through mathematical modeling. We address how each of these projects accomplishes our goals in the following sections.

5.1 SERF

SERF uses a five-stage approach to how the radiant temperature changes through the life cycle of a given fuel cell. Stage one, *stable*, occurs before any temperature changes in the cell, and stage two represents the *warming* of each cell based on the radiant temperature of the surrounding eight cells. After ignition, stage three represents the *rising* of the radiant heat in the cell and stage four represents the *falling* of the heat after the fuel has been mostly consumed. The final stage represents the *cooling* off of the cell back to base temperature. This approach offers the opportunity to simplify the physical processes of fire behavior to save computational time while maintaining the relationships between stages of the burning process.

The significant contribution of this work is a novel, low-complexity, data-driven, spatially extended fire model that employs a coupled map lattice to increase the information provided by the model and inform the basic CA with continuous radiant heat output levels. This model can accurately represent the speed of the fire as it moves through the area. Moreover, it can accurately capture the unburnt proportion of land in the SERF simulations, the presence of lingering embers, the heat coefficients of the fuel on the ground, and the probability of transition between stages.

5.2 DUET

DUET provides complex, realistic and adjustable representations of tree leaf litter and grass distributions that directly relate to canopy structure, litter decay, and wind dynamics. Potential applications of this model include developing realistic heterogeneous surface fuel representations for spatially explicit fire behavior models and ecological examinations of ecosystem dynamics dependent on variable representation of litter biomass, including nutrient cycling within senescence processes and fine-scale fire behavior (Hiers et al. 2009). DUET can also be used to examine finer scale litter and grass dynamics that can influence coarser scale fuel and fire dynamics in current stand and landscape level ecosystem models (e.g. (Keane, Loehman, and Holsinger 2011; E. L. Loudermilk et al. 2011; Scheller et al. 2019)).

DUET has the flexibility to be calibrated for any forest type through the tree species characteristics, as well as environmental inputs and parameters. By representing leaf fall within an ellipse, the model allows for approximations within leaf traits, such as surface area and mass, and coarse dispersal functions. Using DUET, one could vary wind speeds and direction through time and characterize several possible surface fuel representations for simulating ecosystem or fire behavior within the area. Our results show how the drag coefficient, wind dynamics, and decay factors affect litter accumulation though space and time. Through species specific parameterization, the model can be calibrated for specific species or generalized for a broad range of species (e.g., conifer vs. broadleaves). Similarly, wind inputs can represent specific wind events or averaged values across a given area. Such mechanistic models are critical for representations of fine-scale heterogeneity driven by canopies, their influence on patterns of energy release from fires and resulting patterns of fire effects, as well as ecosystem renewal applications (R. J. Mitchell et al. 2006).

5.3 Detecting Chaos in Fire

A broad range of behaviors have been observed in low-intensity fires. Some experience sudden extinction, while others transition into high-intensity fire. This sensitivity has been studied with respect to initial wind conditions and moisture content (Wilson Jr. 1985; Jonko et al. 2021; Linn et al. 2021). In our study, we attempt to capture this potential transition point to test the system for the emergence of chaotic dynamics using a FIRETEC simulation, a coupled hydrodynamic-fire behavior model. We find the model presents a broad range of dynamical behaviors with 64.3% of all 3900 series as deterministically chaotic - a solid result that FIRETEC presents fire behavior with strong chaotic tendencies. The vast array of results that we found in this study supports the hypothesis that subtle differences in winds, fuel, or other environmental factors affect fire behavior. Many of the hypotheses that we make in this paper require significant research and comparison to real-life data.

5.4 Summary

These projects presented work to provide models and research to better understand low-intensity fire behavior. SERF provides the mathematical modeling community a novel combination of two modeling formats (cellular automata and coupled map lattice) in an effort to enhance the information that can be gained through a computationally inexpensive fire behavior model. The model provides the fire science community the potential to develop larger data sets of small-scale fire behavior to gain a better understanding of how the radiant heat moves through the area during a fire at very small-scales. DUET is a mechanistic model that ties the canopy arrangement to the forest floor by examining litter deposition according to tree species and placement and wind behavior. This enhances the abilities for large-scale fire behavior models to represent low-intensity fire by offering a more heterogeneous surface fuel arrangement for the fire to interact with in the modeling programs. DUET is a versatile tool for the fire science community and is currently being used by the Forest Service for investigating surface vegetation heterogeneity and the effect on fire behavior. The chaos study is the first step in examining whole system dynamics to better understand the motivating factors in fire behavior using FIRETEC. The project presented a variety of gaps in knowledge regarding how to examine large numbers of series efficiently and may lead to further work that will provide the mathematics community an expansion of the testing capabilities for data-driven chaos theory. The fire science community could benefit from the advanced knowledge that this project could lead to in the future.

CHAPTER 6. Deliverables

6.1 Articles

6.1.1 First Author

McDanold, Jenna S., and Nishant Malik. “Spatially Extended Radiant Heat Fire Model.” *Physical Review E* 107, no. 3 (March 23, 2023): 034133. https://doi.org/10.1103/PhysRevE.107.034133.

McDanold, Jenna S., Rodman R. Linn, Alex K. Jonko, Adam L. Atchley, Scott L. Goodrick, J. Kevin Hiers, Chad M. Hoffman, E. Louise Loudermilk, J.J. O’Brien, Russ A. Parsons, Carolyn Sieg, Julia A. Oliveto. “DUET - Distribution of Understory Using Elliptical Transport: A Mechanistic Model of Leaf Litter and Herbaceous Spatial Distribution Based on Tree Canopy Structure.” *Ecological Modelling* (September 1, 2023): 110425. https://doi.org/10.1016/j.ecolmodel.2023.110425.

McDanold, Jenna S., Alex Jonko, Rod Linn, Sophie Bonner, and Nishant Malik. ”Finding Chaos in Fire.” *Chaos: An Interdisciplinary Journal of Nonlinear Science.* In Prep.

6.1.2 Other

Wang Qing, Matthias Ihme, Rod R. Linn, Yi-Fan Chen, Vivian Yang, Fei Sha, Craig Clements, Jenna S. McDanold, and John Anderson. “A High-Resolution Large-Eddy Simulation Framework for Wildland Fire Predictions Using TensorFlow.” *International Journal of Wildland* Fire 32, no. 12 (October 18, 2023): 1711–25. https://doi.org/10.1071/WF22225.

Banesh, Divya, Jonas Lukasczyk, Jenna McDanold, and David Rogers. ”An Image-based Exploration of Prescribed Fire Simulation Ensembles.” *IEEE Transactions on Visualization and Computer Graphics*. Submitted to IEEE VIZ 2024 Conference in March, 2024. In Review.

6.2 Software

6.2.1 SERF

For SERF, we coded the simulation program in MATLAB and created visualizations of the dataset and output simulations using the MATLAB plotting programs. To begin the project, we cleaned the dataset described in section 2.2.1, by first taking the 3.1 million matrices of infrared data recorded and determining which contained heat by searching for a 30% variance in the values within each matrix through the terminal. We then used the time indexes for the fires to “stack” each matrix into a time series tensor for each individual fire in MATLAB, producing over 300 potential fires. We then visualized these fires to find useful fires without various impurities like condensation on the lens or a viewing area that was cut off by the end of the burn zone, resulting in the usable dataset of 74 fires. We calculated various metrics on the dataset fires and translated the data into several different forms, which can be seen in tables 6.1, 6.2, and 6.3.

6.2.2 DUET

For DUET, we programmed the equations in Fortran90 and Python. The Fortran90 program has been implemented into the LANL Tree-building program that creates the input files necessary for FIRETEC or QUIC-Fire. The code takes either a list of trees for a particular area, or generalized data involving trees per hectare and species information to create a fuel bed for these models and record them into four .dat files, one each for bulk density per cell, moisture level per cell, fuel depth per cell, and sizescale per cell. Sizescale is a parameter related to how the program recognizes fuel within a cell and allows atmospheric interaction with the fuel (i.e. how the wind moves through a field of grass). To accentuate the DUET part of the program, I added a section of the code that takes a given tree list that has a particular domain size, calculating the trees per hectare and general requirements for the species of trees, and expands the given tree list to cover a larger domain.

⋆ **A patent application has been submitted for the methodology of DUET as per the suggestion from the Intellectual Property Department of the Los Alamos National Laboratory. Currently, a copyright has been approved for the release of the DUET program.**

6.2.3 Chaos

This project was programmed in Python, using a variety of packages including numpy, matplotlib, scipy, pandas, ordpy, pypsr, os, sys, and csv.

The ANN test used in the project is open source at the following link:

https://github.com/brunorrboaretto/chaos_detection_ANN/ (Boaretto et al. 2021)

Table 6.1: *All data analysis performed on the dataset received from the USDA Forest Service; Each line contains information regarding how the data was analyzed and the resulting outputs for each fire*

Cell	Label	Description
1	Main tensor	Flux values for a single fire: z-direction is time
2	File Names	List of file names for each time step (z-layer) in the tensor - correlates to original files within directories and subdirectories for the original raw data
3	Video Info - side	Side video information for the flux video of each fire from the dataset
4	Video info - top	Top video information for the flux video of each fire from the dataset
5	Original fire number	Correlates to the first number from the original array of 191 fires after reducing the number of fires to 114
6	Min, Thresh, Max	Minimum flux value from tensor, threshold value, maximum flux value - values determined over all values in the tensor
7	0-1-2 Matrix	Translates the original tensor into a 3-color matrix using the threshold value from cell 6 with unburnt, burning, and burnt as the three values
8	0-1-2 Video	Video created from 3-color array within cell 7
9	Total Flux	Sum of flux values from all cells and all time steps for each fire
10	Single Cell Array	Each fire split into vectors for each cell across all time steps
11	Max Position Matrix	First layer: matrix of all max values for each cell throughout all time steps Second layer: x-value of corresponding max value Third layer: y-value of corresponding max value Fourth layer: time step of corresponding max value
12	Surface Plot Info	Information regarding saved surface plot of all max values for each cell
13	Previous fire number	Fire number relating to the list of 114 fires after switch to 75 fires

Table 6.2: *All data analysis performed on the dataset received from the USDA Forest Service; Each line contains information regarding how the data was analyzed and the resulting outputs for each fire*

Cell	Label	Description
14	Max Time Matrix	First layer: time step for first ”burning” moment in each cell Second layer: time step for max flux in each cell third layer: time step for last ”burning” moment in each cell
15	Max Value Differences	Matrix of Value differences within the max flux matrix: finds the difference between each cell and its neighbor; 8 layers for the 8 neighbors of each cell: 1 = N, 2 = NE, 3 = E, 4 = SE, 5 = S, 6 = SW, 7 = W, 8 = NW, 9 = firenum, 10 = x-value, 11 = y-value
16	Max Time Differences	Matrix of Value differences within the max flux matrix: finds the difference in time steps between the max value for each cell and its neighbor’s max cell ; 8 layers for the 8 neighbors of each cell: 1 = N, 2 = NE, 3 = E, 4 = SE, 5 = S, 6 = SW, 7 = W, 8 = NW, 9 = firenum, 10 = x-value, 11 = y-value
17	Change Matrix	Value differences for each time step for each cell and its neighbors: 1 = N, 2 = NE, 3 = E, 4 = SE, 5 = S, 6 = SW, 7 = W, 8 = NW, 9 = firenum, 10 = x-value, 11 = y-value
18	Temp Matrix	New tensor with Celsius values correlating to infrared values
19	Final Burned Area	The last time step of the 0-1-2 tensor
20	Flux Difference	Finds the difference in flux values from one time step to the next for each cell
21	Flux Statistics	Minimum and maximum flux values per cell
22	Temp Statistics	Corresponding temperatures for cell 21
23	Temp Difference	Transforms the flux values from cell 20 into temperatures
24	Max Temps	Lists only the maximum temperatures for each cell
25	K-matrix	Finds the highest maximum temp for all cells and finds the proportion of that maximum that each cell reaches

Table 6.3: *All data analysis performed on the dataset received from the USDA Forest Service; Each line contains information regarding how the data was analyzed and the resulting outputs for each fire*

Cell	Label	Description
26	State matrix	Finds the state for each timestep in each cell 1 = Basetemps 2 = Warming 3 = Burning and rising 4 = Burning and falling 5 = Cooling
27	Transition Matrix	Finds the Markov chain transition matrix for the fire

Bibliography

Abatzoglou, John T. 2013. “Development of gridded surface meteorological data for ecological applications and modelling.” *International Journal of Climatology* 33 (1): 121–131. ISSN: 1097-0088. https://doi.org/10.1002/joc.3413.

Abatzoglou, John T., and Timothy J. Brown. 2012. “A comparison of statistical downscaling methods suited for wildfire applications.” *International Journal of Climatology* 32 (5): 772–780. ISSN: 1097-0088. https://doi.org/10.1002/joc.2312.

Adair, E. Carol, William J. Parton, Steven J. Del Grosso, Whendee L. Silver, Mark E. Harmon, Sonia A. Hall, Ingrid C. Burke, and Stephen C. Hart. 2008. “Simple three-pool model accurately describes patterns of long-term litter decomposition in diverse climates.” *Global Change Biology* 14 (11): 2636–2660. ISSN: 1365-2486. https://doi.org/10.1111/j.1365-2486.2008.01674.x.

Agee, James K. 1996. “The influence of forest structure on fire behavior.” In *Proceedings of the 17th annual forest vegetation management conference,* 52–68.

Airey-Lauvaux, Catherine, Andrew D. Pierce, Carl N. Skinner, and Alan H. Taylor. 2022. “Changes in fire behavior caused by fire exclusion and fuel build-up vary with topography in California montane forests, USA.” *Journal of Environmental Management* 304 (February): 114255. ISSN: 0301-4797. https://doi.org/10.1016/j.jenvman.2021.114255.

Akemann, Gernot, Zdzislaw Burda, and Mario Kieburg. 2019. “From integrable to chaotic systems: Universal local statistics of Lyapunov exponents.” *EPL (Europhysics Letters)* 126, no. 4 (June): 40001. ISSN: 0295-5075. https://doi.org/10.1209/0295-5075/126/40001.

Albini, Frank A. 1976. *Computer-based models of wildland fire behavior: a user’s manual.* Intermountain Forest / Range Experiment Station, Forest Service, US ... https://www.google.com/books/edition/Computer_based_Models_of_Wildland_Fire_B/iJ9lMi9OvJYC?hl=en&gbpv=0.

Alexandridis, A., D. Vakalis, C. I. Siettos, and G. V. Bafas. 2008. “A cellular automata model for forest fire spread prediction: The case of the wildfire that swept through Spetses Island in 1990.” *Applied Mathematics and Computation* 204, no. 1 (October): 191–201. ISSN: 0096-3003. https://doi.org/10.1016/j.amc.2008.06.046.

Almeida, Rodolfo Maduro, and Elbert E. N. Macau. 2011. “Stochastic cellular automata model for wildland fire spread dynamics.” *Journal of Physics: Conference Series* 285 (March): 012038. ISSN: 1742-6596. https://doi.org/10.1088/1742-6596/285/1/012038.

Alvarez, Albert, Marc Gracia, and Javier Retana. 2012. “Fuel types and crown fire potential in Pinus halepensis forests.” *European Journal of Forest Research* 131, no. 2 (March 1, 2012): 463–474. ISSN: 1612-4677. https://doi.org/10.1007/s10342-011-0520-6.

Andrews, Patricia L. 2018. “The Rothermel surface fire spread model and associated developments: A comprehensive explanation.” *Gen. Tech. Rep. RMRS-GTR-371. Fort Collins, CO: U.S. Department of Agriculture, Forest Service, Rocky Mountain Research Station. 121 p.* 371. https://doi.org/10.2737/RMRS-GTR-371.

Arthur, Mary A., Heather D. Alexander, Daniel C. Dey, Callie J. Schweitzer, and David L. Loftis. 2012. “Refining the Oak-Fire Hypothesis for Management of Oak-Dominated Forests of the Eastern United States.” *Journal of Forestry* 110, no. 5 (July): 257–266. ISSN: 00221201. https://doi.org/10.5849/jof.11-080.

Asmussen, Søren, ed. 2003. “Markov Chains.” In *Applied Probability and Queues,* 3–38. New York, NY: Springer. ISBN: 978-0-387-21525-9. https://doi.org/10.1007/0-387-21525-5_1.

Atchley, Adam L., Rodman Linn, Alex Jonko, Chad M. Hoffman, Jeffrey D. Hyman, Francois Pimont, Carolyn Sieg, and Richard S. Middleton. 2021. “Effects of fuel spatial distribution on wildland fire behaviour.” *International Journal of Wildland Fire* 30, no. 3 (January): 179–189. ISSN: 1448-5516, 1448-5516. https://doi.org/10.1071/WF20096.

Babl-Plauche, E. K., H. D. Alexander, C. M. Siegert, J. L. Willis, and A. I. Berry. 2022. “Mesophication of upland oak forests: Implications of species-specific differences in leaf litter decomposition rates and fuelbed composition.” *Forest Ecology and Management* 512 (May): 120141. ISSN: 0378-1127. https://doi.org/10.1016/j.foreco.2022.120141.

Bandt, Christoph, and Bernd Pompe. 2002. “Permutation Entropy: A Natural Complexity Measure for Time Series.” *Physical Review Letters* 88, no. 17 (April): 174102. https://doi.org/10.1103/PhysRevLett.88.174102.

Banerjee, Tirtha, Troy Holland, Kurt Solander, Marlin Holmes, and Rodman Linn. 2020. “Identifying Characteristics of Wildfire Towers and Troughs.” *Atmosphere* 11, no. 8 (August): 796. ISSN: 2073-4433. https://doi.org/10.3390/atmos11080796.

Banks, J., J. Brooks, G. Cairns, G. Davis, and P. Stacey. 1992. “On Devaney’s Definition of Chaos.” *The American Mathematical Monthly* 99 (4): 332–334. ISSN: 0002-9890. https://doi.org/10.1080/00029890.1992.11995856.

Barnes, J.A., and D.W. Allan. 1966. “A statistical model of flicker noise.” *Proceedings of the IEEE* 54, no. 2 (February): 176–178. ISSN: 1558-2256. https://doi.org/10.1109/PROC.1966.4630.

Berg, Björn, and Mikael Lönn. 2022. “Long-Term Effects of Climate and Litter Chemistry on Rates and Stable Fractions of Decomposing Scots Pine and Norway Spruce Needle Litter—A Synthesis.” *Forests* 13, no. 1 (January): 125. ISSN: 1999-4907. https://doi.org/10.3390/f13010125.

Bergman, Theodore L., Adrienne S. Lavine, Frank P. Incropera, and David P. DeWitt. 2011. *Fundamentals of Heat and Mass Transfer.* 7th edition. Hoboken, NJ: Wiley, April 12, 2011. ISBN: 978-0-470-50197-9.

Berjak, Stephen G, and John W Hearne. 2002. “An improved cellular automaton model for simulating fire in a spatially heterogeneous Savanna system.” *Ecological Modelling* 148, no. 2 (February): 133–151. ISSN: 0304-3800. https://doi.org/10.1016/S0304-3800(01)00423-9.

Blauw, Luke G., Niki Wensink, Lisette Bakker, Richard S. P. van Logtestijn, Rien Aerts, Nadejda A. Soudzilovskaia, and J. Hans C. Cornelissen. 2015. “Fuel moisture content enhances nonadditive effects of plant mixtures on flammability and fire behavior.” *Ecology and Evolution* 5 (17): 3830–3841. ISSN: 2045-7758. https://doi.org/10.1002/ece3.1628.

Boaretto, B. R. R., R. C. Budzinski, K. L. Rossi, T. L. Prado, S. R. Lopes, and C. Masoller. 2021. "Discriminating chaotic and stochastic time series using permutation entropy and artificial neural networks." *Scientific Reports* 11, no. 1 (August): 15789. ISSN: 2045-2322. https://doi.org/10.1038/s41598-021-95231-z.

Bond, W. J., F. I. Woodward, and G. F. Midgley. 2005. "The global distribution of ecosystems in a world without fire." *New Phytologist* 165 (2): 525–538. ISSN: 1469-8137. https://doi.org/10.1111/j.1469-8137.2004.01252.x.

Braga-Neto, Ulisses. 2005. "Small-sample error estimation: mythology versus mathematics." In *Mathematical Methods in Pattern and Image Analysis,* 5916:304–314. SPIE, August. https://doi.org/10.1117/12.619331.

Bright, Benjamin C., Andrew T. Hudak, Arjan J. H. Meddens, Todd J. Hawbaker, Jennifer S. Briggs, and Robert E. Kennedy. 2017. "Prediction of Forest Canopy and Surface Fuels from Lidar and Satellite Time Series Data in a Bark Beetle-Affected Forest." *Forests* 8, no. 9 (September): 322. https://doi.org/10.3390/f8090322.

Broadleaf. 2024. In *Merriam-Webster.* Merriam-Webster. Accessed June 18, 2024. https://www.merriam-webster.com/dictionary/broadleaf.

Brown, Ray, and Leon O. Chua. 1996. "Clarifying chaos: examples and counterexamples." *International Journal of Bifurcation and Chaos* 06 (02): 219–249. ISSN: 0218-1274. https://doi.org/10.1142/S0218127496000023.

Burgan, Robert E. 1984. *BEHAVE: Fire Behavior Prediction and Fuel Modeling System, Fuel Subsystem.* U.S. Department of Agriculture, Forest Service, Intermountain Forest / Range Experiment Station.

Campbell-Lochrie, Zakary, Carlos Walker-Ravena, Michael Gallagher, Nicholas Skowronski, Eric V. Mueller, and Rory M. Hadden. 2021. "Investigation of the role of bulk properties and in-bed structure in the flow regime of buoyancy-dominated flame spread in porous fuel beds." *Fire Safety Journal,* Fire Safety Science: Proceedings of the 13th International Symposium, 120 (March): 103035. ISSN: 0379-7112. https://doi.org/10.1016/j.firesaf.2020.103035.

Canfield, J. M., Rodman Linn, J. A. Sauer, M. Finney, and Jason Forthofer. 2014. "A numerical investigation of the interplay between fireline length, geometry, and rate of spread." *Agricultural and Forest Meteorology* 189-190 (June): 48–59. ISSN: 0168-1923. https://doi.org/10.1016/j.agrformet.2014.01.007.

Carpenter, Dana O., Melanie K. Taylor, Mac A. Callaham, J. Kevin Hiers, E. Louise Loudermilk, Joseph J. O'Brien, and Nina Wurzburger. 2021. "Benefit or Liability? The Ectomycorrhizal Association May Undermine Tree Adaptations to Fire After Long-term Fire Exclusion." *Ecosystems* 24, no. 5 (August): 1059–1074. ISSN: 1435-0629. https://doi.org/10.1007/s10021-020-00568-7.

Cellular Automata. 2022. In *American Heritage Dictionary,* 5th ed. HarperCollins. Accessed June 19, 2024.

Çengel, Y.A., and A.J. Ghajar. 2019. *Heat and Mass Transfer: Fundamentals & Applications.* McGraw-Hill Education. ISBN: 978-0-07-339819-8. https://books.google.com/books?id=RiXCvgEACAAJ.

Chandler, Craig C., Theodore G. Storey, and Charles D. Tangren. 1963. *Prediction of Fire Spread Following Nuclear Explosions.* Research Paper 418076. Pacific Southwest Forest and Range Experiment Station, Berkeley, California: US Forest Service, September 30, 1963. https://apps.dtic.mil/sti/citations/tr/AD0418076.

Clark, Terry L., Mary Ann Jenkins, Janice Coen, and David Packham. 1996. "A Coupled Atmosphere-Fire Model: Convective Feedback on Fire-Line Dynamics" (June 1, 1996). ISSN: 1520-0450. https://doi.org/10.1175/1520-0450(1996)035⟨0875:ACAMCF⟩2.0.CO;2.

Clements, Craig B., Neil P. Lareau, Daisuke Seto, Jonathan Contezac, Braniff Davis, Casey Teske, Thomas J. Zajkowski, et al. 2015. "Fire weather conditions and fire–atmosphere interactions observed during low-intensity prescribed fires – RxCADRE 2012." *International Journal of Wildland Fire* 25, no. 1 (December): 90–101. ISSN: 1448-5516, 1448-5516. https://doi.org/10.1071/WF14173.

Clements, Craig B., and Daisuke Seto. 2015. "Observations of Fire–Atmosphere Interactions and Near-Surface Heat Transport on a Slope." *Boundary-Layer Meteorology* 154, no. 3 (March 1, 2015): 409–426. ISSN: 1573-1472. https://doi.org/10.1007/s10546-014-9982-7.

Coen, Janice L., W. Schroeder, S. Conway, and L. Tarnay. 2020. "Computational modeling of extreme wildland fire events: A synthesis of scientific understanding with applications to forecasting, land management, and firefighter safety." *Journal of Computational Science* 45 (September): 101152. ISSN: 1877-7503. https://doi.org/10.1016/j.jocs.2020.101152.

Conifer. 2024. In *Merriam-Webster.* Merriam-Webster. Accessed June 18, 2024. https://www.merriam-webster.com/dictionary/conifer.

Cornelissen, Johannes H. C., Saskia Grootemaat, Lieneke M. Verheijen, William K. Cornwell, Peter M. van Bodegom, René van der Wal, and Rien Aerts. 2017. "Are litter decomposition and fire linked through plant species traits?" *New Phytologist* 216 (3): 653–669. ISSN: 1469-8137. https://doi.org/10.1111/nph.14766.

Curry, John R., and Wallace L. Fons. 1938. "Rate of Spread of Surface Fires in the Ponderosa Pine Type of California." *Journal of Agricultural Research* 57, no. 4 (August 15, 1938): 239–267.

Dämmig, M, and F Mitschke. 1993. "Estimation of Lyapunov exponents from time series: the stochastic case." *Physics Letters A* 178, no. 5 (July): 385–394. ISSN: 0375-9601. https://doi.org/10.1016/0375-9601(93)90865-W.

De Smedt, Pallieter, Safaa Wasof, Tom Van de Weghe, Martin Hermy, Dries Bonte, and Kris Verheyen. 2018. "Macro-detritivore identity and biomass along with moisture availability control forest leaf litter breakdown in a field experiment." *Applied Soil Ecology* 131 (October): 47–54. ISSN: 0929-1393. https://doi.org/10.1016/j.apsoil.2018.07.010.

Decoster, Gregory P., and Douglas W. Mitchell. 1991. "The efficacy of the correlation dimension technique in detecting determinism in small samples." *Journal of Statistical Computation and Simulation* 39, no. 4 (September): 221–229. ISSN: 0094-9655. https://doi.org/10.1080/00949659108811357.

Dell, Jane E., Lora A. Richards, Joseph J. O'Brien, E. Louise Loudermilk, Andrew T. Hudak, Scott M. Pokswinski, Benjamin C. Bright, J. Kevin Hiers, Brett W. Williams, and Lee A. Dyer. 2017. "Overstory-derived surface fuels mediate plant species diversity in frequently burned longleaf pine forests." *Ecosphere* 8 (10): e01964. ISSN: 2150-8925. https://doi.org/10.1002/ecs2.1964.

Drossel, B., and F. Schwabl. 1992. "Self-organized critical forest-fire model." *Physical Review Letters* 69, no. 11 (September): 1629–1632. https://doi.org/10.1103/PhysRevLett.69.1629.

Duff. 2024. In *Merriam-Webster.* Merriam-Webster. Accessed June 18, 2024. https://www.merriam-webster.com/dictionary/duff.

Dupuy, J.-L., Rodman Linn, V. Konovalov, F. Pimont, J. A. Vega, and E. Jiménez. 2011. "Exploring three-dimensional coupled fire–atmosphere interactions downwind of wind-driven surface fires and their influence on backfires using the HIGRAD-FIRETEC model." *International Journal of Wildland Fire* 20, no. 6 (January): 734–750. ISSN: 1448-5516, 1448-5516. https://doi.org/10.1071/WF10035.

Eckmann, J. -P., S. Oliffson Kamphorst, D. Ruelle, and S. Ciliberto. 1986. "Liapunov exponents from time series." *Physical Review A* 34, no. 6 (December): 4971–4979. https://doi.org/10.1103/PhysRevA.34.4971.

Edge, Engineers, and Engineers Edge LLC. *Nusselt Number for Forced Convection.* Accessed December 15, 2023. https://www.engineersedge.com/heat_transfer/nusselt_number_13856.htm.

Etheridge, D. E. 1958. "The effect on variations in decay of moisture content and rate of growth in subalpine spruce." *Canadian Journal of Botany* 36, no. 1 (January): 187–206. ISSN: 0008-4026. https://doi.org/10.1139/b58-016.

Ferrari, James B., and Shinya Sugita. 1996. "A spatially explicit model of leaf litter fall in hemlock–hardwood forests." *Canadian Journal of Forest Research* 26, no. 11 (November): 1905–1913. ISSN: 0045-5067. https://doi.org/10.1139/x26-215.

Finney, Mark A. 1998. *FARSITE, Fire Area Simulator–model Development and Evaluation.* U.S. Department of Agriculture, Forest Service, Rocky Mountain Research Station.

Finney, Mark A., Jack D. Cohen, Jason M. Forthofer, Sara S. McAllister, Michael J. Gollner, Daniel J. Gorham, Kozo Saito, Nelson K. Akafuah, Brittany A. Adam, and Justin D. English. 2015. "Role of buoyant flame dynamics in wildfire spread." *Proceedings of the National Academy of Sciences* 112, no. 32 (August): 9833–9838. https://doi.org/10.1073/pnas.1504498112.

FLIR. 2018. *FLIR LEPTON 1.6 ENGINEERING DATA SHEET.* Accessed August 11, 2022. https://www.manualslib.com/manual/1557936/Flir-Lepton-1-6.html.

Fons, Wallace L. 1946. “Analysis of Fire Spread in Light Forest Fuels.” *Journal of Agricultural Research* 72, no. 13 (February 1, 1946). https://www.google.com/books/edition/Journal_of_Agricultural_Research/Ls1FAQAAIAAJ?hl=en&gbpv=0.

Forrester, David I., and Jürgen Bauhus. 2016. “A Review of Processes Behind Diversity-Productivity Relationships in Forests.” *Current Forestry Reports* 2, no. 1 (March): 45–61. ISSN: 2198-6436. https://doi.org/10.1007/s40725-016-0031-2.

Frandsen, William H. 1971. “Fire spread through porous fuels from the conservation of energy.” *Combustion and Flame* 16, no. 1 (February 1, 1971): 9–16. ISSN: 0010-2180. https://doi.org/10.1016/S0010-2180(71)80005-6.

Freire, Joana Gouveia, and Carlos Castro DaCamara. 2019. “Using cellular automata to simulate wildfire propagation and to assist in fire management.” *Natural Hazards and Earth System Sciences* 19, no. 1 (January): 169–179. ISSN: 1561-8633. https://doi.org/10.5194/nhess-19-169-2019.

Gajardo, John, Mariano García, and David Riaño. 2014. “Applications of Airborne Laser Scanning in Forest Fuel Assessment and Fire Prevention.” In *Forestry Applications of Airborne Laser Scanning: Concepts and Case Studies,* edited by Matti Maltamo, Erik Næsset, and Jari Vauhkonen, 439–462. Dordrecht: Springer Netherlands. ISBN: 978-94-017-8663-8. https://doi.org/10.1007/978-94-017-8663-8_22.

García-Palacios, Pablo, E. Ashley Shaw, Diana H. Wall, and Stephan Hättenschwiler. 2016. “Temporal dynamics of biotic and abiotic drivers of litter decomposition.” *Ecology Letters* 19 (5): 554–563. ISSN: 1461-0248. https://doi.org/10.1111/ele.12590.

Gavazov, Konstantin S. 2010. “Dynamics of alpine plant litter decomposition in a changing climate.” *Plant and Soil* 337, no. 1 (December): 19–32. ISSN: 1573-5036. https://doi.org/10.1007/s11104-010-0477-0.

Gencay, Ramazan, and W. Davis Dechert. 1992. “An algorithm for the n Lyapunov exponents of an n-dimensional unknown dynamical system.” *Physica D: Nonlinear Phenomena* 59, no. 1 (October): 142–157. ISSN: 0167-2789. https://doi.org/10.1016/0167-2789(92)90210-E.

Gennaro, Matthieu de, Yann Billaud, Yannick Pizzo, Savitri Garivait, Jean-Claude Loraud, Mahmoud El Hajj, and Bernard Porterie. 2017. “Real-time wildland fire spread modeling using tabulated flame properties.” *Fire Safety Journal,* Fire Safety Science: Proceedings of the 12th International Symposium, 91 (July): 872–881. ISSN: 0379-7112. https://doi.org/10.1016/j.firesaf.2017.03.006.

Ghisu, Tiziano, Bachisio Arca, Grazia Pellizzaro, and Pierpaolo Duce. 2015. “An optimal Cellular Automata algorithm for simulating wildfire spread.” *Environmental Modelling & Software* 71 (September): 1–14. ISSN: 1364-8152. https://doi.org/10.1016/j.envsoft.2015.05.001.

Gisborne, H. T. 1927. “The Objectives of Forest Fire-Weather Research.” *Journal of Forestry* 25, no. 4 (April 1, 1927): 452–456. ISSN: 0022-1201. https://doi.org/10.1093/jof/25.4.452.

Goodwin, Nicholas R., Nicholas C. Coops, and Darius S. Culvenor. 2006. “Assessment of forest structure with airborne LiDAR and the effects of platform altitude.” *Remote Sensing of Environment* 103, no. 2 (July): 140–152. ISSN: 0034-4257. https://doi.org/10.1016/j.rse.2006.03.003.

Gottwald, Georg A., and Ian Melbourne. 2004. “A new test for chaos in deterministic systems.” *Proceedings of the Royal Society of London. Series A: Mathematical, Physical and Engineering Sciences* 460, no. 2042 (February): 603–611. https://doi.org/10.1098/rspa.2003.1183.

———. 2008. “Comment on “Reliability of the 0-1 test for chaos”.” *Physical Review E* 77, no. 2 (February): 028201. https://doi.org/10.1103/PhysRevE.77.028201.

———. 2009. “On the validity of the 0–1 test for chaos.” *Nonlinearity* 22, no. 6 (May): 1367–1382. ISSN: 0951-7715. https://doi.org/10.1088/0951-7715/22/6/006.

———. 2016. *Chaos Detection and Predictability.* 221–247. Berlin, Heidelberg: Springer. ISBN: 978-3-662-48410-4. https://doi.org/10.1007/978-3-662-48410-4_7.

Grassberger, Peter, and Itamar Procaccia. 1983. “Estimation of the Kolmogorov entropy from a chaotic signal.” *Physical Review A* 28, no. 4 (October): 2591–2593. https://doi.org/10.1103/PhysRevA.28.2591.

Greene, D. F., and E. A. Johnson. 1989. “A Model of Wind Dispersal of Winged or Plumed Seeds.” *Ecology* 70 (2): 339–347. ISSN: 1939-9170. https://doi.org/10.2307/1937538.

Griffiths, Deryn. 1999. “Improved Formula for the Drought Factor in McArthur’s Forest Fire Danger Meter.” *Australian Forestry* 62, no. 2 (January 1, 1999): 202–206. ISSN: 0004-9158. https://doi.org/10.1080/00049158.1999.10674783.

Hanberry, Brice B. 2021. “Transition from Fire-Dependent Open Forests: Alternative Ecosystem States in the Southeastern United States.” *Diversity* 13, no. 9 (September): 411. ISSN: 1424-2818. https://doi.org/10.3390/d13090411.

Hawley, Christie M., E. Louise Loudermilk, Eric M. Rowell, and Scott Pokswinski. 2018. “A novel approach to fuel biomass sampling for 3D fuel characterization.” *MethodsX* 5 (January 1, 2018): 1597–1604. ISSN: 2215-0161. https://doi.org/10.1016/j.mex.2018.11.006.

Hawley, L. F. 1926. “Theoretical Considerations Regarding Factors which Influence Forest Fires.” *Journal of Forestry* 24, no. 7 (November 1, 1926): 756–763. ISSN: 0022-1201. https://doi.org/10.1093/jof/24.7.756.

Haykin, Simon. 1998. *Neural Networks: A Comprehensive Foundation.* Prentice Hall PTR. https://doi.org/10.5555/521706.

Henry, Miguel, and George Judge. 2019. “Permutation Entropy and Information Recovery in Nonlinear Dynamic Economic Time Series.” *Econometrics* 7, no. 1 (March): 10. ISSN: 2225-1146. https://doi.org/10.3390/econometrics7010010.

Herault, Alexis, Annamaria Vicari, Alessia Ciraudo, and Ciro Del Negro. 2009. "Forecasting lava flow hazards during the 2006 Etna eruption: Using the MAGFLOW cellular automata model." *Computers & Geosciences,* Modelling and Simulation of Dangerous Phenomena for Hazard Mapping, 35, no. 5 (May): 1050–1060. ISSN: 0098-3004. https://doi.org/10.1016/j.cageo.2007.10.008.

Hernández Encinas, L., S. Hoya White, A. Martín del Rey, and G. Rodríguez Sánchez. 2007. "Modelling forest fire spread using hexagonal cellular automata." *Applied Mathematical Modelling* 31, no. 6 (June): 1213–1227. ISSN: 0307-904X. https://doi.org/10.1016/j.apm.2006.04.001.

Heylighen, Francis. 2001. "The science of self-organization and adaptivity." *The encyclopedia of life support systems* 5 (3): 253–280. https://www.academia.edu/download/3243859/science_of_self_organization.pdf.

Hiers, J. Kevin, Joseph J. O'Brien, Rodney E. Will, and Robert J. Mitchell. 2007. "Forest Floor Depth Mediates Understory Vigor in Xeric Pinus Palustris Ecosystems." *Ecological Applications* 17 (3): 806–814. ISSN: 1939-5582. https://doi.org/10.1890/06-1015.

Hiers, J. Kevin, Joseph J. O'Brien, R. J. Mitchell, John M. Grego, and E. Louise Loudermilk. 2009. "The wildland fuel cell concept: an approach to characterize fine-scale variation in fuels and fire in frequently burned longleaf pine forests." *International Journal of Wildland Fire* 18, no. 3 (May): 315–325. ISSN: 1448-5516, 1448-5516. https://doi.org/10.1071/WF08084.

Hoffman, Chad M., Carolyn H. Sieg, Rodman Linn, William Mell, Russell A. Parsons, Justin P. Ziegler, and J. Kevin Hiers. 2018. "Advancing the Science of Wildland Fire Dynamics Using Process-Based Models." *Fire* 1, no. 2 (September): 32. https://doi.org/10.3390/fire1020032.

Hudak, Andrew T., Nicholas L. Crookston, Jeffrey S. Evans, David E. Hall, and Michael J. Falkowski. 2008. "Nearest neighbor imputation of species-level, plot-scale forest structure attributes from LiDAR data." *Remote Sensing of Environment,* Earth Observations for Terrestrial Biodiversity and Ecosystems Special Issue, 112, no. 5 (May): 2232–2245. ISSN: 0034-4257. https://doi.org/10.1016/j.rse.2007.10.009.

Hunt, Brian R., and Edward Ott. 2015. "Defining chaos." *Chaos: An Interdisciplinary Journal of Nonlinear Science* 25 (9): 097618. ISSN: 1054-1500. https://doi.org/10.1063/1.4922973.

Hyde, Peter, Ralph Dubayah, Wayne Walker, J. Bryan Blair, Michelle Hofton, and Carolyn Hunsaker. 2006. "Mapping forest structure for wildlife habitat analysis using multi-sensor (LiDAR, SAR/InSAR, ETM+, Quickbird) synergy." *Remote Sensing of Environment* 102, no. 1 (May): 63–73. ISSN: 0034-4257. https://doi.org/10.1016/j.rse.2006.01.021.

Iniguez, Jose M., Thomas W. Swetnam, and Stephen R. Yool. 2008. "Topography affected landscape fire history patterns in southern Arizona, USA." *Forest Ecology and Management,* Impacts of forest ecosystem management on greenhouse gas budgets, 256, no. 3 (July 30, 2008): 295–303. ISSN: 0378-1127. https://doi.org/10.1016/j.foreco.2008.04.023.

Jarron, Lukas R., Nicholas C. Coops, William H. MacKenzie, Piotr Tompalski, and Pamela Dykstra. 2020. “Detection of sub-canopy forest structure using airborne LiDAR.” *Remote Sensing of Environment* 244 (July): 111770. ISSN: 0034-4257. https://doi.org/10.1016/j.rse.2020.111770.

Jonard, Mathieu, Frederic Andre, and Quentin Ponette. 2006. “Modeling Leaf Dispersal in Mixed Hardwood Forests Using a Ballistic Approach.” *Ecology* 87 (9): 2306–2318. ISSN: 1939-9170. https://doi.org/10.1890/0012-9658(2006)87[2306:MLDIMH]2.0.CO;2.

Jonko, Alexandra K., Kara M. Yedinak, Juliana L. Conley, and Rodman Linn. 2021. “Sensitivity of Grass Fires Burning in Marginal Conditions to Atmospheric Turbulence.” *Journal of Geophysical Research: Atmospheres* 126 (13): e2020JD033384. ISSN: 2169-8996. https://doi.org/10.1029/2020JD033384.

Kantz, Holger, and Thomas Schreiber. 2003. *Nonlinear Time Series Analysis.* 2nd ed. Cambridge University Press.

Kauwe, Steven K., Jake Graser, Antonio Vazquez, and Taylor D. Sparks. 2018. “Machine Learning Prediction of Heat Capacity for Solid Inorganics.” *Integrating Materials and Manufacturing Innovation* 7, no. 2 (June): 43–51. ISSN: 2193-9772. https://doi.org/10.1007/s40192-018-0108-9.

Keane, Robert E. 2008. “Biophysical controls on surface fuel litterfall and decomposition in the northern Rocky Mountains, USA.” *Canadian Journal of Forest Research* 38, no. 6 (June): 1431–1445. ISSN: 0045-5067. https://doi.org/10.1139/X08-003.

Keane, Robert E., James K. Agee, Peter Fulé, Jon E. Keeley, Carl Key, Stanley G. Kitchen, Richard Miller, and Lisa A. Schulte. 2008. “Ecological effects of large fires on US landscapes: benefit or catastrophe?A.” *International Journal of Wildland Fire* 17, no. 6 (December 12, 2008): 696–712. ISSN: 1448-5516. https://doi.org/10.1071/WF07148.

Keane, Robert E., Rachel A. Loehman, and Lisa M. Holsinger. 2011. “The FireBGCv2 landscape fire and succession model: a research simulation platform for exploring fire and vegetation dynamics.” *Gen. Tech. Rep. RMRS-GTR-255. Fort Collins, CO: U.S. Department of Agriculture, Forest Service, Rocky Mountain Research Station. 137 p.* 255. https://doi.org/10.2737/RMRS-GTR-255.

Keane, Robert E., and Matt Reeves. 2012. “Use of Expert Knowledge to Develop Fuel Maps for Wildland Fire Management.” In *Expert Knowledge and Its Application in Landscape Ecology,* edited by Ajith H. Perera, C. Ashton Drew, and Chris J. Johnson, 211–228. New York, NY: Springer. ISBN: 978-1-4614-1034-8. https://doi.org/10.1007/978-1-4614-1034-8_11.

Khastagir, Anirban, Niranjali Jayasuriya, and Muhammed A. Bhuyian. 2018. “Assessment of fire danger vulnerability using McArthur’s forest and grass fire danger indices.” *Natural Hazards* 94, no. 3 (December 1, 2018): 1277–1291. ISSN: 1573-0840. https://doi.org/10.1007/s11069-018-3476-8.

Kilgore, Bruce M., and Rodney W. Sando. 1975. “Crown-Fire Potential in a Sequoia Forest After Prescribed Burning.” *Forest Science* 21, no. 1 (March 1, 1975): 83–87. ISSN: 0015-749X. https://doi.org/10.1093/forestscience/21.1.83.

Koo, Eunmo, Rodman Linn, Patrick J. Pagni, and Carleton B. Edminster. 2012. "Modelling firebrand transport in wildfires using HIGRAD/FIRETEC." *International Journal of Wildland Fire* 21, no. 4 (March): 396–417. ISSN: 1448-5516, 1448-5516. https://doi.org/10.1071/WF09146.

Kremens, Robert L. 2019. *Personal Interview on Fire Dynamics.*

Kronholm, Kalle, and Karl W. Birkeland. 2005. "Integrating spatial patterns into a snow avalanche cellular automata model." *Geophysical Research Letters* 32 (19). ISSN: 1944-8007. https://doi.org/10.1029/2005GL024373.

La Puma, Inga P., Richard G. Lathrop, and Nicholas S. Keuler. 2013. "A large-scale fire suppression edge-effect on forest composition in the New Jersey Pinelands." *Landscape Ecology* 28, no. 9 (November): 1815–1827. ISSN: 1572-9761. https://doi.org/10.1007/s10980-013-9924-7.

Lacasa, Lucas, and Jesús Gómez-Gardeñes. 2013. "Correlation Dimension of Complex Networks." *Physical Review Letters* 110, no. 16 (April): 168703. https://doi.org/10.1103/PhysRevLett.110.168703.

Lai, Ying-Cheng, and David Lerner. 1998. "Effective scaling regime for computing the correlation dimension from chaotic time series." *Physica D: Nonlinear Phenomena* 115, no. 1 (April): 1–18. ISSN: 0167-2789. https://doi.org/10.1016/S0167-2789(97)00230-3.

Lareau, Neil P., Nicholas J. Nauslar, Evan Bentley, Matthew Roberts, Samuel Emmerson, Brian Brong, Matthew Mehle, and James Wallman. 2022. "Fire-Generated Tornadic Vortices." *Bulletin of the American Meteorological Society* 103, no. 5 (May): E1296–E1320. ISSN: 0003-0007, 1520-0477. https://doi.org/10.1175/BAMS-D-21-0199.1.

Lin, Guigang, M. Luke McCormack, Chengen Ma, and Dali Guo. 2017. "Similar below-ground carbon cycling dynamics but contrasting modes of nitrogen cycling between arbuscular mycorrhizal and ectomycorrhizal forests." *New Phytologist* 213 (3): 1440–1451. ISSN: 1469-8137. https://doi.org/10.1111/nph.14206.

Linn, Rodman. 1997. *A transport model for prediction of wildfire behavior.* Technical report LA-13334-T. Los Alamos National Lab., NM (United States), July. https://doi.org/10.2172/505313.

———. 2019. "Fluid dynamics of wildfires: Once a wildfire is ignited, complex interactions with the local winds affect how it behaves." *Physics Today* 72, no. 11 (November): 70. ISSN: 0031-9228. https://doi.org/10.1063/PT.3.4350.

Linn, Rodman, J. M. Canfield, P. Cunningham, C. Edminster, J. -L. Dupuy, and F. Pimont. 2012. "Using periodic line fires to gain a new perspective on multi-dimensional aspects of forward fire spread." *Agricultural and Forest Meteorology* 157 (May): 60–76. ISSN: 0168-1923. https://doi.org/10.1016/j.agrformet.2012.01.014.

Linn, Rodman, Jon Reisner, Jonah J. Colman, and Judith Winterkamp. 2002. "Studying wildfire behavior using FIRETEC." *International Journal of Wildland Fire* 11 (4): 233–246. ISSN: 1448-5516. https://doi.org/10.1071/wf02007.

Linn, Rodman, Judith Winterkamp, Jonah J. Colman, Carleton Edminster, and John D. Bailey. 2005. “Modeling interactions between fire and atmosphere in discrete element fuel beds.” *International Journal of Wildland Fire* 14, no. 1 (March): 37–48. ISSN: 1448-5516, 1448-5516. https://doi.org/10.1071/WF04043.

Linn, Rodman, Judith L. Winterkamp, James H. Furman, Brett Williams, J. Kevin Hiers, Alexandra Jonko, Joseph J. O’Brien, Kara M. Yedinak, and Scott Goodrick. 2021. “Modeling Low Intensity Fires: Lessons Learned from 2012 RxCADRE.” *Atmosphere* 12, no. 2 (February): 139. ISSN: 2073-4433. https://doi.org/10.3390/atmos12020139.

Litak, G., A. Syta, M. Budhraja, and L. M. Saha. 2009. “Detection of the chaotic behaviour of a bouncing ball by the 0–1 test.” *Chaos, Solitons & Fractals* 42, no. 3 (November): 1511–1517. ISSN: 0960-0779. https://doi.org/10.1016/j.chaos.2009.03.048.

Litak, Grzegorz, Arkadiusz Syta, and Marian Wiercigroch. 2009. “Identification of chaos in a cutting process by the 0–1 test.” *Chaos, Solitons & Fractals* 40, no. 5 (June): 2095–2101. ISSN: 0960-0779. https://doi.org/10.1016/j.chaos.2007.09.093.

Litter. 2022. In *American Heritage Dictionary,* 5th ed. HarperCollins. Accessed June 19, 2024.

Liu, Yuxuan, Hu Liu, Yaoming Zhou, and Cong Sun. 2018. “Spread vector induced cellular automata model for real-time crown fire behavior simulation.” *Environmental Modelling & Software* 108 (October): 14–39. ISSN: 1364-8152. https://doi.org/10.1016/j.envsoft.2018.07.005.

Livneh, Ben, Eric A. Rosenberg, Chiyu Lin, Bart Nijssen, Vimal Mishra, Kostas M. Andreadis, Edwin P. Maurer, and Dennis P. Lettenmaier. 2013. “A Long-Term Hydrologically Based Dataset of Land Surface Fluxes and States for the Conterminous United States: Update and Extensions.” *Journal of Climate* 26, no. 23 (December): 9384–9392. ISSN: 0894-8755, 1520-0442. https://doi.org/10.1175/JCLI-D-12-00508.1.

Lopes, A. M. G., M. G. Cruz, and D. X. Viegas. 2002. “*FireStation* — an integrated software system for the numerical simulation of fire spread on complex topography.” *Environmental Modelling & Software* 17, no. 3 (January 1, 2002): 269–285. ISSN: 1364-8152. https://doi.org/10.1016/S1364-8152(01)00072-X.

Lorenz, Edward N. 1963. “Deterministic Nonperiodic Flow.” *Journal of the Atmospheric Sciences* 20, no. 2 (March): 130–141. ISSN: 0022-4928, 1520-0469. https://doi.org/10.1175/1520-0469(1963)020⟨0130:DNF⟩2.0.CO;2.

Loudermilk, E. L., W. P. Cropper, R. J. Mitchell, and H. Lee. 2011. “Longleaf pine (Pinus palustris) and hardwood dynamics in a fire-maintained ecosystem: A simulation approach.” *Ecological Modelling* 222, no. 15 (August): 2733–2750. ISSN: 0304-3800. https://doi.org/10.1016/j.ecolmodel.2011.05.004.

Loudermilk, E. Louise, Gary L. Achtemeier, Joseph J. O’Brien, J. Kevin Hiers, and Benjamin S. Hornsby. 2014. “High-resolution observations of combustion in heterogeneous surface fuels.” *International Journal of Wildland Fire* 23, no. 7 (September): 1016–1026. ISSN: 1448-5516, 1448-5516. https://doi.org/10.1071/WF13160.

Loudermilk, E. Louise, J. Kevin Hiers, Joseph J. O'Brien, Robert J. Mitchell, Abhinav Singhania, Juan C. Fernandez, Wendell P. Cropper, and K. Clint Slatton. 2009. "Ground-based LIDAR: a novel approach to quantify fine-scale fuelbed characteristics." *International Journal of Wildland Fire* 18, no. 6 (September): 676–685. ISSN: 1448-5516, 1448-5516. https://doi.org/10.1071/WF07138.

Loudermilk, E.Louise, J.Kevin Hiers, and Joseph J. O'Brien. 2017. "The Role of Fuels for Understanding Fire Behavior and Fire Effects." In *Ecological Restoration and Management of Longleaf Pine Forests,* 1st, 107–122. CRC Press, September. ISBN: 978-0-367-65773-4. https://doi.org/10.1201/9781315152141-6.

Mahmoud, Hussam, and Akshat Chulahwat. 2017. "A Probabilistic Cellular Automata Framework for Assessing the Impact of WUI Fires on Communities." *Procedia Engineering,* Urban Transitions Conference, Shanghai, September 2016, 198 (January): 1111–1122. ISSN: 1877-7058. https://doi.org/10.1016/j.proeng.2017.07.153.

Malik, Nishant. 2020. "Uncovering transitions in paleoclimate time series and the climate driven demise of an ancient civilization." *Chaos: An Interdisciplinary Journal of Nonlinear Science* 30, no. 8 (August): 083108. https://doi.org/10.1063/5.0012059.

———. 2024. *Personal Interview on Math Terminology.*

Mampel, J., V. Egorova, and G. Pagnini. 2023. "Predicting the arrival of the unpredictable: An approach for foreseeing the transition to chaos of wildfire propagation." *Communications in Nonlinear Science and Numerical Simulation* (July). https://bird.bcamath.org/handle/20.500.11824/1636.

Mandel, J., S. Amram, J. D. Beezley, G. Kelman, A. K. Kochanski, V. Y. Kondratenko, B. H. Lynn, B. Regev, and M. Vejmelka. 2014. "Recent advances and applications of WRF-SFIRE." *Natural Hazards and Earth System Sciences* 14, no. 10 (October 31, 2014): 2829–2845. ISSN: 1561-8633. https://doi.org/10.5194/nhess-14-2829-2014.

Mandelbrot, Benoit B. 1982. *The fractal geometry of nature.* San Francisco : W.H. Freeman. ISBN: 978-0-7167-1186-5. http://archive.org/details/fractalgeometryo00beno.

Manzello, Samuel L., Sayaka Suzuki, Michael J. Gollner, and A. Carlos Fernandez-Pello. 2020. "Role of firebrand combustion in large outdoor fire spread." *Progress in Energy and Combustion Science* 76 (January): 100801. ISSN: 0360-1285. https://doi.org/10.1016/j.pecs.2019.100801.

Margolis, Stephen B., and Bernard J. Matkowsky. 1983. "Nonlinear Stability and Bifurcation in the Transition from Laminar to Turbulent Flame Propagation." *Combustion Science and Technology* 34, nos. 1-6 (October): 44–77. ISSN: 0010-2202. https://doi.org/10.1080/00102208308923687.

Marshall, Ginny, Dan K. Thompson, Kerry Anderson, Brian Simpson, Rodman Linn, and Dave Schroeder. 2020. "The Impact of Fuel Treatments on Wildfire Behavior in North American Boreal Fuels: A Simulation Study Using FIRETEC." *Fire* 3, no. 2 (June): 18. ISSN: 2571-6255. https://doi.org/10.3390/fire3020018.

McArthur, A.G. 1966. “Weather and Grassland Fire Behaviour.” *Forestry Timber Bureau Australia* 100, no. 23 (December 14, 1966). https://doi.org/10.5555/19660605795.

McDanold, Jenna S., Rodman Linn, Alex K. Jonko, Adam L. Atchley, Scott L. Goodrick, J. Kevin Hiers, Chad M. Hoffman, et al. 2023. “DUET - Distribution of Understory using Elliptical Transport: A mechanistic model of leaf litter and herbaceous spatial distribution based on tree canopy structure.” *Ecological Modelling* 483 (September): 110425. ISSN: 0304-3800. https://doi.org/10.1016/j.ecolmodel.2023.110425.

McDanold, Jenna S., and Nishant Malik. 2023. “Spatially extended radiant heat fire model.” *Physical Review E* 107, no. 3 (March): 034133. https://doi.org/10.1103/PhysRevE.107.034133.

McGranahan, Devan Allen, and Carissa L. Wonkka. 2020. *Ecology of Fire-Dependent Ecosystems: Wildland Fire Science, Policy, and Management.* Boca Raton: CRC Press, December 29, 2020. ISBN: 978-0-429-48709-5. https://doi.org/10.1201/9780429487095.

McLauchlan, Kendra K., Philip E. Higuera, Jessica Miesel, Brendan M. Rogers, Jennifer Schweitzer, Jacquelyn K. Shuman, Alan J. Tepley, et al. 2020. “Fire as a fundamental ecological process: Research advances and frontiers.” *Journal of Ecology* 108 (5): 2047–2069. ISSN: 1365-2745. https://doi.org/10.1111/1365-2745.13403.

Mell, William, Mary Ann Jenkins, Jim Gould, and Phil Cheney. 2007. “A physics-based approach to modelling grassland fires.” *International Journal of Wildland Fire* 16, no. 1 (February 20, 2007): 1–22. ISSN: 1448-5516. https://doi.org/10.1071/WF06002.

Menning, Kurt M., and Scott L. Stephens. 2007. “Fire Climbing in the Forest: A Semiqualitative, Semiquantitative Approach to Assessing Ladder Fuel Hazards.” *Western Journal of Applied Forestry* 22, no. 2 (April 1, 2007): 88–93. ISSN: 0885-6095. https://doi.org/10.1093/wjaf/22.2.88.

Midgley, Meghan G., Edward Brzostek, and Richard P. Phillips. 2015. “Decay rates of leaf litters from arbuscular mycorrhizal trees are more sensitive to soil effects than litters from ectomycorrhizal trees.” *Journal of Ecology* 103 (6): 1454–1463. ISSN: 1365-2745. https://doi.org/10.1111/1365-2745.12467.

Mitchell, R J, J K Hiers, J J O’Brien, S B Jack, and R T Engstrom. 2006. “Silviculture that sustains: the nexus between silviculture, frequent prescribed fire, and conservation of biodiversity in longleaf pine forests of the southeastern United States.” *Canadian Journal of Forest Research* 36, no. 11 (November): 2724–2736. ISSN: 0045-5067. https://doi.org/10.1139/x06-100.

Mitchell, R.j., R.h. Marrs, M.g. Le Duc, and M.h.d. Auld. 1999. “A study of the restoration of heathland on successional sites: changes in vegetation and soil chemical properties.” *Journal of Applied Ecology* 36 (5): 770–783. ISSN: 1365-2664. https://doi.org/10.1046/j.1365-2664.1999.00443.x.

Montgomery, Rebecca A., Peter B. Reich, and Brian J. Palik. 2010. “Untangling positive and negative biotic interactions: views from above and below ground in a forest ecosystem.” *Ecology* 91 (12): 3641–3655. ISSN: 1939-9170. https://doi.org/10.1890/09-1663.1.

Mueller, Eric V., Michael R. Gallagher, Nicholas Skowronski, and Rory M. Hadden. 2021. "Approaches to Modeling Bed Drag in Pine Forest Litter for Wildland Fire Applications." *Transport in Porous Media* 138, no. 3 (July): 637–660. ISSN: 1573-1634. https://doi.org/10.1007/s11242-021-01637-8.

Nickmans, Hans, Mathieu Jonard, Kris Verheyen, and Quentin Ponette. 2019. "Modelling leaf dispersal and nutrient return in tree species mixtures." *Forest Ecology and Management* 436 (March): 68–78. ISSN: 0378-1127. https://doi.org/10.1016/j.foreco.2019.01.001.

Noble, I. R., A. M. Gill, and G. a. V. Bary. 1980. "McArthur's fire-danger meters expressed as equations." *Australian Journal of Ecology* 5 (2): 201–203. ISSN: 1442-9993. https://doi.org/10.1111/j.1442-9993.1980.tb01243.x.

O'Brien, Joseph J., E. Louise Loudermilk, J. Kevin Hiers, Scott M. Pokswinski, Benjamin Hornsby, Andrew T. Hudak, Dexter Strother, Eric Rowell, and Benjamin C. Bright. 2016. "Canopy-Derived Fuels Drive Patterns of In-Fire Energy Release and Understory Plant Mortality in a Longleaf Pine (Pinus palustris) Sandhill in Northwest Florida, USA." *Canadian Journal of Remote Sensing* 42, no. 5 (September): 489–500. ISSN: 0703-8992, 1712-7971. https://doi.org/10.1080/07038992.2016.1199271.

Olson, Jerry S. 1963. "Energy Storage and the Balance of Producers and Decomposers in Ecological Systems." *Ecology* 44 (2): 322–331. ISSN: 0012-9658. https://doi.org/10.2307/1932179.

Ottmar, Roger D., J. Kevin Hiers, Bret W. Butler, Craig B. Clements, Matthew B. Dickinson, Andrew T. Hudak, Joseph J. O'Brien, et al. 2015. "Measurements, datasets and preliminary results from the RxCADRE project – 2008, 2011 and 2012." *International Journal of Wildland Fire* 25, no. 1 (November): 1–9. ISSN: 1448-5516, 1448-5516. https://doi.org/10.1071/WF14161.

Ouannas, Adel, Amina-Aicha Khennaoui, Shaher Momani, and Viet-Thanh Pham. 2020. "The discrete fractional duffing system: Chaos, 0–1 test, C complexity, entropy, and control." *Chaos: An Interdisciplinary Journal of Nonlinear Science* 30, no. 8 (August): 083131. ISSN: 1054-1500. https://doi.org/10.1063/5.0005059.

Overstory. 2022. In *American Heritage Dictionary,* 5th ed. HarperCollins. Accessed June 19, 2024.

Parsons, Russell A., Rodman Linn, Francois Pimont, Chad M. Hoffman, Jeremy Sauer, Judith Winterkamp, Carolyn H. Sieg, and W. Matt Jolly. 2017. "Numerical Investigation of Aggregated Fuel Spatial Pattern Impacts on Fire Behavior." *Land* 6, no. 2 (June): 43. ISSN: 2073-445X. https://doi.org/10.3390/land6020043.

Parsons, Russell A., Francois Pimont, Lucas Wells, Greg Cohn, W. Matt Jolly, Francois de Coligny, Eric Rigolot, Jean-Luc Dupuy, William Mell, and Rodman Linn. 2018. "Modeling thinning effects on fire behavior with STANDFIRE." *Annals of Forest Science* 75, no. 1 (January): 7. ISSN: 1297-966X. https://doi.org/10.1007/s13595-017-0686-2.

Pecot, Stephen D., Robert J. Mitchell, Brian J. Palik, E. Barry Moser, and J. Kevin Hiers. 2007. "Competitive responses of seedlings and understory plants in longleaf pine woodlands: separating canopy influences above and below ground." *Canadian Journal of Forest Research* 37, no. 3 (March): 634–648. ISSN: 0045-5067. https://doi.org/10.1139/X06-247.

Pimont, François, Jean-Luc Dupuy, Rodman Linn, and Sylvain Dupont. 2011. "Impacts of tree canopy structure on wind flows and fire propagation simulated with FIRETEC." *Annals of Forest Science* 68, no. 3 (April): 523–530. ISSN: 1297-966X. https://doi.org/10.1007/s13595-011-0061-7.

Pimont, François, Russell Parsons, Eric Rigolot, François de Coligny, Jean-Luc Dupuy, Philippe Dreyfus, and Rodman Linn. 2016. "Modeling fuels and fire effects in 3D: Model description and applications." *Environmental Modelling & Software* 80 (June): 225–244. ISSN: 1364-8152. https://doi.org/10.1016/j.envsoft.2016.03.003.

Potter, Brian E. 2012a. "Atmospheric interactions with wildland fire behaviour – I. Basic surface interactions, vertical profiles and synoptic structures." *International Journal of Wildland Fire* 21, no. 7 (July): 779–801. ISSN: 1448-5516. https://doi.org/10.1071/WF11128.

———. 2012b. "Atmospheric interactions with wildland fire behaviour – II. Plume and vortex dynamics." *International Journal of Wildland Fire* 21, no. 7 (July): 802–817. ISSN: 1448-5516. https://doi.org/10.1071/WF11129.

Prescott, Cindy E., and Sue J. Grayston. 2013. "Tree species influence on microbial communities in litter and soil: Current knowledge and research needs." *Forest Ecology and Management,* Influence of tree species on forest soils: New evidence from field studies, 309 (December): 19–27. ISSN: 0378-1127. https://doi.org/10.1016/j.foreco.2013.02.034.

Prior, Lynda D., Brett P. Murphy, and David M. J. S. Bowman. 2018. "Conceptualizing Ecological Flammability: An Experimental Test of Three Frameworks Using Various Types and Loads of Surface Fuels." *Fire* 1, no. 1 (June): 14. https://doi.org/10.3390/fire1010014.

Progias, Pavlos, and Georgios Ch. Sirakoulis. 2013. "An FPGA processor for modelling wildfire spreading." *Mathematical and Computer Modelling* 57, no. 5 (March): 1436–1452. ISSN: 0895-7177. https://doi.org/10.1016/j.mcm.2012.12.005.

Quintiere, James G. 1998. *Principles of Fire Behavior.* Delmar Publishers. ISBN: 978-0-8273-7732-5.

Rebba, Ramesh, Sankaran Mahadevan, and Shuping Huang. 2006. "Validation and error estimation of computational models." *Reliability Engineering & System Safety,* The Fourth International Conference on Sensitivity Analysis of Model Output (SAMO 2004), 91, no. 10 (October): 1390–1397. ISSN: 0951-8320. https://doi.org/10.1016/j.ress.2005.11.035.

Reisner, Jon, Shannon Wynne, Len Margolin, and Rodman Linn. 2000. "Coupled Atmospheric–Fire Modeling Employing the Method of Averages." *Monthly Weather Review* 128, no. 10 (October): 3683–3691. ISSN: 1520-0493, 0027-0644. https://doi.org/10.1175/1520-0493(2001)129⟨3683:CAFMET⟩2.0.CO;2.

Ricotta, Carlo, Giancarlo Avena, and Marco Marchetti. 1999. "The flaming sandpile: self-organized criticality and wildfires." *Ecological Modelling* 119, no. 1 (July): 73–77. ISSN: 0304-3800. https://doi.org/10.1016/S0304-3800(99)00057-5.

Riegel, Gregg M., Richard F. Miller, and William C. Krueger. 1992. "Competition for Resources Between Understory Vegetation and Overstory Pinus Ponderosa in Northeastern Oregon." *Ecological Applications* 2 (1): 71–85. ISSN: 1939-5582. https://doi.org/10.2307/1941890.

Robbins, Zachary J., E. Louise Loudermilk, Matthew J. Reilly, Joseph J. O'Brien, Kate Jones, Christopher T. Gerstle, and Robert M. Scheller. 2022. "Delayed fire mortality has long-term ecological effects across the Southern Appalachian landscape." *Ecosphere* 13 (6): e4153. ISSN: 2150-8925. https://doi.org/10.1002/ecs2.4153.

Rogers, Jack C., and T. Miller. 1963. *Survey of the Thermal Threat of Nuclear Weapons.* Unclassified Version IMU-4021. Department of Defense, Washington, D.C.: Office of Civil Defense, November.

Rosenstein, Michael T., James J. Collins, and Carlo J. De Luca. 1993. "A practical method for calculating largest Lyapunov exponents from small data sets." *Physica D: Nonlinear Phenomena* 65, no. 1 (May): 117–134. ISSN: 0167-2789. https://doi.org/10.1016/0167-2789(93)90009-P.

Rosso, O. A., H. A. Larrondo, M. T. Martin, A. Plastino, and M. A. Fuentes. 2007. "Distinguishing Noise from Chaos." *Physical Review Letters* 99, no. 15 (October): 154102. https://doi.org/10.1103/PhysRevLett.99.154102.

Rothermel, Richard C. 1972. *A Mathematical Model for Predicting Fire Spread in Wildland Fuels.*

Rothermel, Richard C., and Hal E. Anderson. 1966. *Fire Spread Characteristics Determined in the Laboratory.* Intermountain Forest & Range Experiment Station, Forest Service, U.S. Department of Agriculture.

Rothman, Daniel H. 1988. "Cellular-automaton fluids: A model for flow in porous media." *GEOPHYSICS* 53, no. 4 (April): 509–518. ISSN: 0016-8033. https://doi.org/10.1190/1.1442482.

Rowell, Eric, E. Louise Loudermilk, Christie Hawley, Scott Pokswinski, Carl Seielstad, LLoyd Queen, Joseph J. O'Brien, Andrew T. Hudak, Scott Goodrick, and J. Kevin Hiers. 2020. "Coupling terrestrial laser scanning with 3D fuel biomass sampling for advancing wildland fuels characterization." *Forest Ecology and Management* 462 (April): 117945. ISSN: 0378-1127. https://doi.org/10.1016/j.foreco.2020.117945.

Ruiz, Luis A., Txomin Hermosilla, Francisco Mauro, and Miguel Godino. 2014. "Analysis of the Influence of Plot Size and LiDAR Density on Forest Structure Attribute Estimates." *Forests* 5, no. 5 (May): 936–951. https://doi.org/10.3390/f5050936.

Sander, Evelyn, and James A. Yorke. 2015. "The Many Facets of Chaos." *International Journal of Bifurcation and Chaos* 25, no. 04 (April): 1530011. ISSN: 0218-1274. https://doi.org/10.1142/S0218127415300116.

Sato, Shinichi, Masaki Sano, and Yasuji Sawada. 1987. "Practical Methods of Measuring the Generalized Dimension and the Largest Lyapunov Exponent in High Dimensional Chaotic Systems." *Progress of Theoretical Physics* 77, no. 1 (January): 1–5. ISSN: 0033-068X. https://doi.org/10.1143/PTP.77.1.

Sauer, Carl O. 1950. "Grassland, Climax, Fire, and Man." *Rangeland Ecology & Management/Journal of Range Management Archives* 3 (1): 16–21. https://journals.uair.arizona.edu/index.php/jrm/article/download/4355/3966.

Savi, Marcelo A., Francisco Heitor I. Pereira-Pinto, Flavio M. Viola, Aline Souza de Paula, Davide Bernardini, Grzegorz Litak, and Giuseppe Rega. 2017. "Using 0–1 test to diagnose chaos on shape memory alloy dynamical systems." *Chaos, Solitons & Fractals* 103 (October): 307–324. ISSN: 0960-0779. https://doi.org/10.1016/j.chaos.2017.06.016.

Scheller, Robert, Alec Kretchun, Todd J. Hawbaker, and Paul D. Henne. 2019. "A landscape model of variable social-ecological fire regimes." *Ecological Modelling* 401 (June): 85–93. ISSN: 0304-3800. https://doi.org/10.1016/j.ecolmodel.2019.03.022.

Seielstad, C.A., and L.P. Queen. 2003. "Using Airborne Laser Altimetry to Determine Fuel Models for Estimating Fire Behavior." *Journal of Forestry* 101, no. 4 (June): 10–15. ISSN: 0022-1201. https://doi.org/10.1093/jof/101.4.10.

Shah, Sami Ullah, Marta Yebra, Albert I. J. M. Van Dijk, and Geoffrey J. Cary. 2022. "Relating McArthur fire danger indices to remote sensing derived burned area across Australia." *International Journal of Wildland Fire* 32, no. 2 (November 15, 2022): 133–148. ISSN: 1448-5516. https://doi.org/10.1071/WF21108.

Silva, Carlos A., Andrew T. Hudak, Lee A. Vierling, E. Louise Loudermilk, Joseph J. O'Brien, J. Kevin Hiers, Steve B. Jack, et al. 2016. "Imputation of individual longleaf pine (Pinus palustris Mill.) tree attributes from field and LiDAR data." *Canadian Journal of Remote Sensing. 42(5): 554-573.* 42 (5): 554–573. ISSN: 0703-8992. https://doi.org/10.1080/07038992.2016.1196582.

Sivakumar, B. 2004. "Chaos theory in geophysics: past, present and future." *Chaos, Solitons & Fractals,* Fractals in Geophysics, 19 (2): 441–462. ISSN: 0960-0779. https://doi.org/10.1016/S0960-0779(03)00055-9.

Skowronski, Nicholas S., Michael R. Gallagher, and Timothy A. Warner. 2020. "Decomposing the Interactions between Fire Severity and Canopy Fuel Structure Using Multi-Temporal, Active, and Passive Remote Sensing Approaches." *Fire* 3, no. 1 (March): 7. ISSN: 2571-6255. https://doi.org/10.3390/fire3010007.

Sprott, J. C., and G. Rowlands. 2001. "Improved correlation dimension calculation." *International Journal of Bifurcation and Chaos* 11, no. 07 (July): 1865–1880. ISSN: 0218-1274. https://doi.org/10.1142/S021812740100305X.

Staelens, Jeroen, Lieven Nachtergale, Sebastiaan Luyssaert, and Noël Lust. 2003. "A model of wind-influenced leaf litterfall in a mixed hardwood forest." *Canadian Journal of Forest Research* 33, no. 2 (February): 201–209. ISSN: 0045-5067. https://doi.org/10.1139/x02-174.

Stephens, S. L., M. A. Finney, and H. Schantz. 2004. "Bulk density and fuel loads of ponderosa pine and white fir forest floors: impacts of leaf morphology." *Northwest Science* 78 (2): 93–110. ISSN: 0029-344X. https://www.cabdirect.org/cabdirect/abstract/20043105936.

Stochastic. 2022. In *American Heritage Dictionary,* 5th ed. HarperCollins. Accessed June 19, 2024.

Stoler, Aaron B., and Rick A. Relyea. 2011. "Living in the litter: the influence of tree leaf litter on wetland communities." *Oikos* 120 (6): 862–872. ISSN: 1600-0706. https://doi.org/10.1111/j.1600-0706.2010.18625.x.

Stowe, Johnny. 2019. "AFTER ACTION: Witnessing drought in longleaf pine country." *Wildfire Magazine* 4.

Strogatz, Steven H. 2019. *Nonlinear Dynamics and Chaos: With Applications to Physics, Biology, Chemistry, and Engineering.* 2nd ed. Boca Raton: CRC Press, May. ISBN: 978-0-429-49256-3. https://doi.org/10.1201/9780429492563.

Sullivan, Andrew L. 2009. "Wildland surface fire spread modelling, 1990–2007. 1: Physical and quasi-physical models." *International Journal of Wildland Fire* 18, no. 4 (June 29, 2009): 349–368. ISSN: 1448-5516. https://doi.org/10.1071/WF06143.

Tinkham, Wade T., Alistair M.S. Smith, Chad M. Hoffman, Andrew T. Hudak, Michael J. Falkowski, Mark E. Swanson, and Paul E. Gessler. 2012. "Investigating the influence of LiDAR ground surface errors on the utility of derived forest inventories." *Canadian Journal of Forest Research* 42, no. 3 (March): 413–422. ISSN: 0045-5067. https://doi.org/10.1139/x11-193.

Toffoli, Tommaso. 1984. "Cellular automata as an alternative to (rather than an approximation of) differential equations in modeling physics." *Physica D: Nonlinear Phenomena* 10, no. 1 (January): 117–127. ISSN: 0167-2789. https://doi.org/10.1016/0167-2789(84)90254-9.

Torres, Fillipe Tamiozzo Pereira, Joyce Machado Nunes Romeiro, Ana Carolina de Albuquerque Santos, Ricardo Rodrigues de Oliveira Neto, Gumercindo Souza Lima, and José Cola Zanuncio. 2018. "Fire danger index efficiency as a function of fuel moisture and fire behavior." *Science of The Total Environment* 631-632 (August): 1304–1310. ISSN: 0048-9697. https://doi.org/10.1016/j.scitotenv.2018.03.121.

Touzé, Cyril, and Antoine Chaigne. 2000. "Lyapunov Exponents from Experimental Time Series: Application to Cymbal Vibrations." *Acta Acustica united with Acustica* 86, no. 3 (May): 557–567.

Trap, Jean, Marthe Akpa-Vinceslas, Pierre Margerie, Simon Boudsocq, Franck Richard, Thibaud Decaëns, and Michaël Aubert. 2017. "Slow decomposition of leaf litter from mature Fagus sylvatica trees promotes offspring nitrogen acquisition by interacting with ectomycorrhizal fungi." *Journal of Ecology* 105 (2): 528–539. ISSN: 1365-2745. https://doi.org/10.1111/1365-2745.12665.

Trunfio, Giuseppe A., Donato D'Ambrosio, Rocco Rongo, William Spataro, and Salvatore Di Gregorio. 2011. "A New Algorithm for Simulating Wildfire Spread through Cellular Automata." *ACM Transactions on Modeling and Computer Simulation* 22, no. 1 (December): 6:1–6:26. ISSN: 1049-3301. https://doi.org/10.1145/2043635.2043641.

Turcotte, Donald L., Sergey G. Abaimov, Robert Shcherbakov, and John B. Rundle. 2007. "Nonlinear Dynamics of Natural Hazards." Edited by Anastasios A. Tsonis and James B. Elsner. *Nonlinear Dynamics in Geosciences* (New York, NY), 557–580. https://doi.org/10.1007/978-0-387-34918-3_30.

Understory. 2022. In *American Heritage Dictionary,* 5th ed. HarperCollins. Accessed June 19, 2024.

"USDA Forest Service Fire Terminology Web Page." 2024. Accessed June 19, 2024. https://www.fs.usda.gov/nwacfire/home/terminology.html.

Van Lear, David H., W. D. Carroll, P. R. Kapeluck, and Rhett Johnson. 2005. "History and restoration of the longleaf pine-grassland ecosystem: Implications for species at risk." *Forest Ecology and Management,* Relative Risk Assessments for Decision –Making Related To Uncharacteristic Wildfire, 211, no. 1 (June 6, 2005): 150–165. ISSN: 0378-1127. https://doi.org/10.1016/j.foreco.2005.02.014.

Vichniac, Gérard Y. 1984. "Simulating physics with cellular automata." *Physica D: Nonlinear Phenomena* 10, no. 1 (January): 96–116. ISSN: 0167-2789. https://doi.org/10.1016/0167-2789(84)90253-7.

Wade, Dale D., and James D. Lunsford. 1989. *A Guide for Prescribed Fire in Southern Forests.* Technical Publication R8-TP-11. U.S. Department of Agriculture, Forest Service, Southern Region.

Weber, R. O. 1991. "Modelling fire spread through fuel beds." *Progress in Energy and Combustion Science* 17, no. 1 (January 1, 1991): 67–82. ISSN: 0360-1285. https://doi.org/10.1016/0360-1285(91)90003-6.

Wilson Jr., Ralph A. 1985. "Observations of Extinction and Marginal Burning States in Free Burning Porous Fuel Beds." *Combustion Science and Technology* 44, nos. 3-4 (December): 179–193. ISSN: 0010-2202. https://doi.org/10.1080/00102208508960302.

Wolf, Alan, Jack B. Swift, Harry L. Swinney, and John A. Vastano. 1985. "Determining Lyapunov exponents from a time series." *Physica D: Nonlinear Phenomena* 16, no. 3 (July): 285–317. ISSN: 0167-2789. https://doi.org/10.1016/0167-2789(85)90011-9.

Wolfram, Stephen. 1983. "Statistical mechanics of cellular automata." *Reviews of Modern Physics* 55, no. 3 (July): 601–644. https://doi.org/10.1103/RevModPhys.55.601.

Xeric. 2022. In *American Heritage Dictionary,* 5th ed. HarperCollins. Accessed June 19, 2024.

Yassemi, S., S. Dragićević, and M. Schmidt. 2008. "Design and implementation of an integrated GIS-based cellular automata model to characterize forest fire behaviour." *Ecological Modelling* 210, no. 1 (January): 71–84. ISSN: 0304-3800. https://doi.org/10.1016/j.ecolmodel.2007.07.020.

Yongzhong, Zhang, Z.-D. Feng, Han Tao, Wu Liyu, Li Kegong, and Duan Xin. 2004. "Simulating wildfire spreading processes in a spatially heterogeneous landscapes using an improved cellular automaton model." In *IGARSS 2004. 2004 IEEE International Geoscience and Remote Sensing Symposium,* vol. 5, 3371–3374 vol.5. IGARSS 2004. 2004 IEEE International Geoscience and Remote Sensing Symposium. September. https://doi.org/10.1109/IGARSS.2004.1370427.

Zhang, Shiyu, Jiuqing Liu, Hewei Gao, Xiandong Chen, Xingdong Li, and Jun Hua. 2022. "Study on Forest Fire spread Model of Multi-dimensional Cellular Automata based on Rothermel Speed Formula." *CERNE* 27 (March 7, 2022). ISSN: 0104-7760, 2317-6342. https://doi.org/10.1590/01047760202127012932.

Zheng, Zhong, Wei Huang, Songnian Li, and Yongnian Zeng. 2017. "Forest fire spread simulating model using cellular automaton with extreme learning machine." *Ecological Modelling* 348 (March): 33–43. ISSN: 0304-3800. https://doi.org/10.1016/j.ecolmodel.2016.12.022.

APPENDIX A. HIGRAD-FIRETEC

Here we describe the governing equations for calculating the variables we used within FIRETEC and it's coupled hydrodynamic solver HIGRAD. HIGRAD-FIRETEC is, in its essence, a modified Navier-Stokes system that takes an ignition sequence and a fuel bed or canopy arrangement as inputs. FIRETEC works with HIGRAD to track the fire movement throughout the domain space. HIGRAD is an atmospheric simulator that uses a Method of Averages scheme to decrease computational expense (Reisner et al. 2000).

A.0.1 Definitions

- **Solid**: The combination of the fuel and the water within a given material.
- **Fuel**: The dry portion of the solid.
- **Cell**: The three-dimensional cube at a given coordinate in the FIRETEC domain space.
- **Cylinder**: The basic building blocks of the fuel within a particular FIRETEC cell; all fuel is modeled to be made up of several cylinders such that environmental factors may move through the area in between each cylinder.

A.0.2 Q

Q stands for Convective Heat Transfer and is used in FIRETEC to describe the transfer of heat from the gas to the solid within a given cell. It is positive when the gas in the cell is hotter than the solid in the cell as it is measured from the perspective of the solid. The equation is related to the basic convective heat transfer formula from Çengel and Ghajar (Çengel and Ghajar 2019):

$$Q = h\gamma(T_g - T) \tag{A.1}$$

where

- h is the convective heat transfer coefficient (units = $W/m^{-2} \cdot K^{-1}$),
- γ is a scaling coefficient based off of the relationship of the bulk density to the true density,
- T_g is the temperature of the gas in the cell, and
- T is the temperature of the solid.

Note that since we are subtracting T from T_g, this value can be negative when the gas in the cell is hotter than the solid. We define each of these parameters below.

The parameter h can be derived from using the Nusselt number, which in thermodynamics can be defined as the ratio of the convective heat transfer to the conductive heat transfer:

$$Nu = \frac{h}{C_p/L} = \frac{hL}{C_p} \tag{A.2}$$

where C_p is the thermal conductivity or specific heat of the air (units = $W/m^{-1} \cdot K^{-1}$), and L is a characteristic length which we define as the radius of the cylinder (units = m). When we solve for h in this equation, we find:

$$h = \frac{NuC_p}{L} \tag{A.3}$$

In practice, we define the Nusselt number as a function of the Reynold's number to represent forced convection within the fire. In FIRETEC, the vegetation is modeled as a collection of cylinders of ranging sizes (i.e. 0.005 m for grass) so that the wind may travel through the cylinders and spread the fire. Thus, we use a Nusselt number associated with crossflow wind across a cylinder (Edge and LLC,):

$$Nu = 0.683Re^{0.466} \tag{A.4}$$

and altogether we get:

$$h = 0.683Re^{0.466}\frac{C_p}{L} \tag{A.5}$$

with units of $W/m^{-2} \cdot K^{-1}$.

For the parameter γ, we use an area per volume and define it as the ratio of the bulk density of the fuel in the cylinder to the true density of the fuel, multiplied by the radius of the cylinder, L. The bulk density of the fuel ρ_f is defined as the mass of the fuel to the volume of the cell, and the true density of the fuel ρ_0 is defined as the mass of the fuel to the volume of the fuel.

$$\gamma = 2a\frac{\rho_f}{\rho_0}\frac{1}{L} \tag{A.6}$$

where a is a dimensionless correction factor for a change in orientation of the cylinder. This equation can be expressed as being the surface area of the cylinder to the volume of the cell and has units $1/m$.

A.0.3 *T*

T stands for the temperature of the solid. Using conservation of energy laws, this quantity is calculated using the specific internal energy of the solid (E_s) divided by the heat capacity for the solid material at a constant pressure ($C_{p,s}$):

$$T = \frac{E_s}{C_{p,s}} \tag{A.7}$$

We use the Kopp-Neumann Law (Kauwe et al. 2018) to define $C_{p,s}$:

$$C_{p,s} = \frac{\rho_w C_{p,w} + \rho_F C_{p,f}}{\rho_w + \rho_f} \tag{A.8}$$

where we take the density of the water within the solid, ρ_w, and multiply it by the specific heat of the water at constant pressure, $C_{p,w}$. We add that to ρ_F, the density of the fuel within the solid, multiplied by the specific heat of the fuel at constant pressure, $C_{p,f}$; and divide that sum by $\rho_w + \rho_f = \rho_s$, the total density of the solid. We define the change in the energy of the solid (E_S) as:

$$\frac{dE_s}{dt} = Q_{conv} + \theta_s \Delta H_{RXN} - E_{f,m} + \Delta H_{EVAP} - E_{w,m} + R_s \tag{A.9}$$

where we have:

- Q = the convective heat transfer (see Appendix A.0.2)
- $\theta_S \Delta H_{RXN}$ = the amount of energy from combustion returning to the solid with:
  - θ_S = the proportion of the combustion energy that returns to the solid and
  - ΔH_{RXN} = the total energy generated through the combustion reaction
- $E_{f,m} = m_f C_{p,f} T_{RXN}$ is the loss of energy attributed to mass loss during combustion with
  - m_f = mass of fuel lost

  - $C_{p,f}$ = heat capacity of the fuel
  - T_{RXN} = temperature of the combustion reaction
- ΔH_{EVAP} = amount of energy lost due to evaporation of the water in the solid
- $E_{w,m}$ = the loss of energy attributed to water loss through evaporation
- $R_s = -0.8\sigma\gamma(T^4 - T_A^4)$ is the energy added to the solid through radiation with
  - -0.8 is an emissivity constant for the fuel
  - $\sigma = 5.678e-8$ is the Stefan-Boltzmann constant,
  - γ is defined as in Eqn. A.6
  - T = the temperature of the solid and
  - T_A = the ambient temperature

A.0.4 WIND VARIABLES

The horizontal wind magnitude we are using, $UV = \sqrt{u^2 + v^2}$ and the vertical wind velocity W are calculated using HIGRAD, the hydrodynamics solver coupled with FIRETEC. A complete description and all equations associated with these variables can be found in Reisner et al. (2000).

APPENDIX B. Limited Glossary

B.1 Fire and Thermodynamics Terminology

Convective Heat Transfer High-to-low temperature transport of energy between a moving fluid (gas or liquid) and a solid surface (Quintiere 1998).

Fire Behavior The manner in which a fire reacts to the influences of fuel, weather and topography ("USDA Forest Service Fire Terminology Web Page" 2024); The way a fire burns, such as how quickly it spreads, how much energy it gives off, and how much vegetation it consumes.

Fireline AKA *Fire Front* The part of a fire within which continuous flaming combustion is taking place. Unless otherwise specified the fire front is assumed to be the leading edge of the fire perimeter ("USDA Forest Service Fire Terminology Web Page" 2024); in FIRETEC, the fireline is the cells farthest from the ignition source that has a temperature of the solid of 500K or greater.

Heat Coefficient AKA *Thermal Conductivity* The property of matter that represents the ability to transfer heat from high-to-low within a substance (Bergman et al. 2011).

Heat Flux The transfer rate per unit area perpendicular to the direction of transfer and it is proportional to the temperature gradient; in a direction defined as x:

$$Q_x'' = -k\frac{dT}{dx}$$

- $k =$ thermal conductivity
- $\frac{dT}{dx} =$ temperature gradient

(Bergman et al. 2011)

Low-Intensity Fire Flames with an upper bound on the output power range such that the heat consumes the fuel and produces char, but does not burn hot enough to become a crown fire (when the flames encroach on the canopy). These types of fires generally move slower than high-intensity fires and rely on surface fuels as their main driver. Many prescribed burns are designed to be low-intensity fires as they are easier to control and char increases soil fertility for ecosystem management (Linn et al. 2021).

Newton's Law of Cooling The equation for convective heat flux (W/m^2):

$$Q'' = h(T_s - T_\infty)$$

- h = convective heat transfer coefficient
- T_s = temperature of the surface
- T_∞ = temperature of the fluid

Prescribed Fire is defined by the USDA Forest Service as:

> ... fire applied in a knowledgeable manner to forest fuels on a specific land area under selected weather conditions to accomplish predetermined, well-defined management objectives (Wade and Lunsford 1989).

Some examples of these objectives include removing invading species, reducing fuel loads to minimize wildfire risk, perpetuating fire-dependent species, controlling disease, restoring ecosystem balance, and nutrient cycling, among other things.

Radiant Heat Transfer Transfer of heat due to electromagnetic energy transfer such as light (i.e. infrared light) (Quintiere 1998).

B.2 Ecological Terminology

Broadleaf Trees or plants having leaves that are not needles (*Broadleaf* 2024)

Conifer Any of an order of mostly evergreen trees and shrubs having usually needle-shaped or scalelike leaves and including forms (such as pines) with true cones and others (such as yews) with an arillate fruit (*Conifer* 2024).

Decay Factor The total mass loss of a plant per unit of time due to decay; decay factors are affected by moisture levels (Etheridge 1958).

Drag Coefficient A dimensionless quantity used to quantify the resistance of an object moving through a fluid (gas or liquid); ratio of the drag force on an object to the dynamic pressure of the free-stream flow times frontal area of the object (Çengel and Ghajar 2019)

$$C_d = \frac{F_d}{\frac{1}{2}\rho u^2 A}$$

- F_d = drag force on the object in the direction of the flow velocity
- ρ = mass density of the fluid
- u = flow speed of the object relative to the fluid
- A = the reference area

(Bergman et al. 2011)

Duff The partly decayed organic matter on the forest floor (*Duff* 2024)

Litter Fallen leaves and other decaying organic matter that make up the top layer of a forest floor (*Litter* 2022).

Overstory The highest layer of vegetation in a forest, usually forming the canopy; the trees in a forest whose crowns constitute this layer (*Overstory* 2022)

Understory An underlying layer of [live and dead] vegetation; the plants that grow beneath a forest's canopy (*Understory* 2022).

Xeric : Of, characterized by, or adapted to an extremely dry habitat (*Xeric* 2022).

B.3 Mathematical Terminology

Artificial Neural Network A massively parallel combination of simple processing units which can acquire knowledge from environment through a learning process and store the knowledge in its connections loosely based on the structure of the brain (Haykin 1998).

Cellular Automata A discrete mathematical model or dynamical system of an infinite, regular lattice in a finite number of dimensions, which consists of cells, each in a finite number of states. The cells evolve in discrete time steps according to a set of rules based on the state of both the cell and its neighboring cells (*Cellular Automata* 2022).

Chaos Aperiodic long-term behavior in a deterministic system that exhibits sensitive dependence on initial conditions (Strogatz 2019).

Coupled Map Lattice A discrete mathematical model or dynamical system of an infinite, regular lattice in a finite number of dimensions, which consists of cells, each of which is assigned a real number from a continuous set of state variables. The cells evolve in discrete time steps according to a set of rules based on the state of both the cell and its neighboring cells.

Deterministic Causally determined and not subject to random chance; the system has no random or noisy inputs or parameters (Strogatz 2019).

Embedding Dimension / Time Delay AKA *Phase Space Reconstruction Parameters* The minimum dimension needed to reconstruct a topologically equivalent attractor to the attractor in the underlying data by the technique of time-delay embedding; Time delay assists in removing the temporal correlations that exist in time series due to the sampling rate that one would like to remove (Malik 2024).

Eulerian An analysis of fluid flow developed from a frame of reference through which the fluid particles move (Çengel and Ghajar 2019).

Fractal Dimension An index for characterizing fractal patterns or sets by quantifying their complexity as a ratio of the change in detail to the change in scale (Mandelbrot 1982).

Lagrangian : An analysis of fluid flow developed from a frame of reference attached to moving material particles (Çengel and Ghajar 2019).

Permutation Entropy A measure of complexity for a system that finds ordinal relations between the values of time series and calculates the probability of these patterns (Henry and Judge 2019). The Permutation Entropy is defined as:

$$\sum_{i=1}^{r!} -p_i \log_2(p_i)$$

- r = length of possible permutations
- $r!$ = total number of possible permutations
- p_i = probability of the ith permutation

(Bandt and Pompe 2002)

Phase-Space Reconstruction AKA *Attractor Reconstruction* A data analysis technique in which the full phase space dynamics of a system governed by an attractor are reconstructed from a single time series (Strogatz 2019). The reconstruction requires an embedding dimension and a time delay which are defined above.

Self-Organization The appearance of structure or pattern in the evolution of a nonlinear dynamical system without an external agent imposing it (Heylighen 2001).

Spatially Extended : A dynamical system that evolves in space as well as time (Malik 2024).

Stochastic Involving or containing a random variable or process (*Stochastic* 2022).

Transition Matrix AKA *Markov Matrix, Probability Matrix, Stochastic Matrix* For a system that could be in n discrete states, a $n \times n$ matrix in which the abth element, p_{ab} is the probability for a cell in state a to transition to state b (Asmussen 2003).